Politechnika Śląska

Comparative analysis and implementation of selected new alternating current electric arc models

Doctoral Dissertation
by

Maciej Klimas

Supervisor: dr hab. inż. Dariusz Grabowski, prof PŚ

Co-Supervisor: dr inż. Dawid Buła

Faculty of Electrical Engineering
Silesian University of Technology
Gliwice, Poland
2023

Contents

1 Introduction **11**
1.1 Literature overview 13
1.2 Power balance-based electric arc furnace (EAF) model 16

2 Electric arc furnace **19**
2.1 Installation description 19
2.1.1 Mechanical structure 19
2.1.2 Electrical circuit 20
2.1.3 Operation principle 21
2.2 Measurement data 22
2.2.1 Large industrial EAF 23
2.2.2 Small industrial EAF 23
2.2.3 Laboratory EAF 24

3 Stochastic EAF model **29**
3.1 EAF random differential equation 29
3.2 Simulation results and analysis 34
3.2.1 Analysis of K_1, K_2 and K_3 for the large industrial EAF 34
3.2.2 Analysis of K_1, K_2 and K_3 for the small industrial EAF . . . 37
3.2.3 Analysis of K_1, K_2 and K_3 for the laboratory EAF 41
3.2.4 Analysis of $\hat{K}_1$ and $\hat{K}_2$ for the large industrial EAF 44

4 Chaotic EAF model **50**
4.1 Selected chaotic systems 50
4.1.1 Chua circuit 52
4.1.2 Lorenz system 52
4.1.3 Rössler system 53
4.1.4 Four-wing chaotic attractor system 54
4.2 Simulation results and analysis 55
4.2.1 Large industrial EAF 55
4.2.2 Small industrial EAF 58
4.2.3 Laboratory EAF 58

5 Artificial neural network EAF models **62**
5.1 Selected ANNs 62
5.1.1 Shallow ANN 62
5.1.2 Deep ANN 66
5.2 Simulation results and analysis 68
5.2.1 Large industrial EAF 68

5.2.2 Small industrial EAF . . . 73
5.2.3 Laboratory EAF . . . 76

6 Fractional order EAF model **81**
6.1 Fractional order power balance equation . . . 81
6.2 Simulation results and analysis . . . 84
6.2.1 Large industrial EAF . . . 85
6.2.2 Small industrial EAF . . . 89
6.2.3 Laboratory EAF . . . 91

7 Comparative analysis **94**

8 ETMP-ATP EAF model **102**
8.1 Implementation of the RDE model . . . 102
8.1.1 Representation of $\hat{K}_1$ . . . 103
8.1.2 Representation of $\hat{K}_2$ . . . 104
8.1.3 Representation of the high frequency component . . . 104
8.2 Simulation results and analysis . . . 107
8.2.1 Single-phase model . . . 107
8.2.2 Three-phase model . . . 107
8.2.3 Model validation . . . 109

9 Conclusions **111**

10 Appendix - EMTP-ATP code **115**

Bibliography **119**

List of figures **126**

Abstract

Electric arc furnaces (EAFs) are one of the largest and most disturbing loads found in electrical power systems. Their random and nonlinear nature can result in many power quality problems. Mitigating these problems involves the use of power quality improvement systems and the appropriate design of the power system itself. This, in turn, requires detailed knowledge of the furnace behavior and its influence on the electrical circuit. An accurate model can provide that kind of data.

The doctoral dissertation is focused on the development of new, more accurate models of the electric arc phenomena occurring in electric arc furnaces. The modeling process has especially been oriented to the melting stage of the EAF work cycle because of its worst impact on power quality, compared to other stages. The proposed models have been based on measurement data originating from three differently sized real furnaces: a large industrial furnace, a small industrial furnace, and a laboratory-sized self-designed furnace. The analysis carried out based on those datasets has confirmed that the proposed approaches can be successfully applied to installations with various rated powers.

The main part of the thesis is devoted to the actual development of the EAF models using different theoretical approaches. One of the primary goals was to create models capable of reflecting not only the deterministic component of the furnace behavior, but also its stochastic part. To do so, four concepts have been proposed: a model based on a random differential equation, a chaotic model, models using shallow and deep learning artificial neural networks, and a novel fractional order model. Both qualitative and quantitative evaluations presented in the text have shown that all proposed approaches can be effectively applied for EAF model development, significantly reducing errors between modeled and measured waveforms.

Another goal of the dissertation has been related to comparative analysis leading to the selection of a model suitable for implementation in the widely known EMTP-ATP simulation software. The comparison has highlighted the differences between the proposed approaches and evaluated their performance. In conclusion, the models varied in the precision of the stochastic component reflection, the computational power required, and the calculation time. Based on those criteria, a random differential equation model has been chosen and implemented in the EMTP-ATP software using built-in components and the programming language. The results of simulations conducted with the EMTP-ATP software indicate that the proposed model can be applied not only to reflect the single-phase arc but also to model a three-phase device.

An analysis contained in the doctoral dissertation yielded an overview of modern methods for simulation of the stochastic electric arc phenomena. Furthermore, it revealed potential paths for further studies related to the indicated limitations and the simplified assumptions used.

Streszczenie

Elektryczny piec łukowy stanowi jeden z największych odbiorników energii elektrycznej spotykanych w systemach elektroenergetycznych. Jego losowa i nieliniowa charakterystyka może powodować wiele problemów w zakresie jakości energii elektrycznej. Łagodzenie skutków tych problemów wiąże się z koniecznością stosowania systemów poprawy jakości energii oraz odpowiedniego zaprojektowania samego układu zasilania. To z kolei wymaga znajomości zachowania pieca łukowego oraz jego wpływu na sieć. Dokładny model pieca jest w stanie zapewnić te informacje.

Rozprawa doktorska skupia się na stworzeniu nowych, dokładniejszych modeli łuku elektrycznego występującego w elektrycznych piecach łukowych. Praca obejmuje modelowanie etapu roztapiania wsadu, który cechuje się najgorszym wpływem na sieć elektryczną pod kątem jakości energii. Zaproponowane modele zostały opracowane na podstawie danych pochodzących z trzech pieców łukowych różnej wielkości: dużego i małego przemysłowego pieca oraz laboratoryjnego pieca zaprojektowanego specjalnie do tego celu. Analizy przeprowadzone na bazie zgromadzonych danych potwierdziły, że zaproponowane podejścia mogą być skutecznie wykorzystane do modelowania instalacji o różnej mocy znamionowej.

Zasadnicza część pracy jest poświęcona opracowaniu modeli przy wykorzystaniu czterech różnych podejść teoretycznych. Jednym z głównych celów pracy było stworzenie modeli zdolnych do odzwierciedlenia deterministycznego i stochastycznego zachowania pieca. W tym celu zaproponowano zastosowanie następujących metod: modelu opartego o losowe równania różniczkowe, modelu chaotycznego, modeli korzystających z płytkich oraz głębokich sztucznych sieci neuronowych oraz nowego modelu ułamkowego rzędu. Zarówno jakościowa, jak i ilościowa ocena modeli przedstawiona w pracy wykazała, że wszystkie zaproponowane koncepcje mogą być skutecznie stosowane do modelowania elektrycznych pieców łukowych, istotnie zmniejszając błąd między przebiegami symulowanymi a pomiarowymi.

Kolejnym celem pracy była analiza porównawcza opracowanych modeli służąca wybraniu najodpowiedniejszego do implementacji w szeroko stosowanym środowisku symulacyjnym EMTP-ATP. Wyciągnięte wnioski świadczą, iż modele różniły się dokładnością odwzorowania stochastycznych cech obiektu, wymaganą mocą obliczeniową oraz czasem obliczeń. Na podstawie tych kryteriów wybrano model oparty na losowym równaniu różniczkowym. Zaimplementowano go z wykorzystaniem dostępnych w programie komponentów i dedykowanego języka programowania. Wyniki symulacji świadczą, iż zaproponowane rozwiązanie jest zdolne do odzwierciedlenia zarówno pojedynczego łuku elektrycznego, jak i trójfazowego pieca łukowego.

Analiza zawarta w pracy doktorskiej przedstawia współczesne metody modelowania stochastycznych zjawisk towarzyszących łukowi elektrycznemu. Ponadto, wskazuje potencjalne ścieżki do dalszych badań, których przyczynkiem są ograniczenia obecnych rozwiązań oraz zastosowane założenia upraszczające.

Acknowledgements

I would like to sincerely thank dr hab. inż. Dariusz Grabowski, prof. PŚ for his support and guidance throughout my entire doctoral studies and during preparation of this dissertation. I also would like to express many thanks to dr inż. Dawid Buła for his advice and expertise.

I would like to thank mgr inż. Sławomir Tenerowicz and the ZDWO steel and cast iron foundry in Gliwice for allowing me to conduct the measurements in their facility. I also thank prof. Haidar Samet for allowing the use of measurement data from the Mobarakeh Steel Company in Isfahan.

This research is co-financed from government funds for science for years 2019-2023 as part of the "Diamond Grant" program (grant 0139/DIA/2019/48).

Co-financed by the European Union through the European Social Fund (grant POWR.03.05.00-00-Z305).

I thank Poland's PLGrid high-performance computing infrastructure (HPC Centers: ACK Cyfronet AGH) for providing computer facilities and support within computational grant no. PLG/2022/015966.

Chapter 1

Introduction

As stated by the famous writer and scientist Johann Wolfgang von Goethe: "He who moves not forward, goes backward." This philosophy accompanied us throughout the ages, even before being put into words by Goethe. As a consequence, the main goal was always connected with constant growth and development in societal or technical areas. This approach eventually leads to further industrial revolutions and the incorporation of countless solutions for improving our everyday life. However, further development requires increasing energy consumption. It is very important to note that an economy based on endless growth is unsustainable. To maintain sustainability, technological development has started to focus more on the optimization of existing solutions to reduce energy and financial costs. Because the most widely used form of energy is electrical energy, it is especially important to reduce unnecessary losses related to its transmission and final utilization. Not paying attention to excessive power losses is related not only to unnecessary energy production but also to reduced power system capabilities by nonoptimal exploitation of transmission and distribution lines, as well as excessive equipment wear. Consequently, unacted power losses can lead to further financial and environmental losses. This fact imposes an obligation to identify and solve power quality problems.

In worldwide electrical energy consumption, the industrial sector has always been one of the most significant contributors. Due to its scale, the optimization of industrial processes also has the most significant positive influence on the sustainability aspects. An understanding of this sector itself allows for the identification of the loads that can be the most problematic. Among them there is one of the largest electrical loads - an electric arc furnace (EAF). The EAF is a device used for melting processes, mainly for steel production, using the heat generated by the arc burning between the electrodes and the load. The electric arc itself is an unpredictable and strongly nonlinear phenomenon. Due to the high power of EAFs, the negative impact of arc behavior on the power system can be significant. Strong and random variations in power consumption in EAFs, as well as voltage or current deformations, reduce power quality in the supplying power system, therefore increasing unwanted losses. Of course, mitigation methods for such problems exist and are most often directly applied, however, the appropriate selection and design of such devices require detailed knowledge about the load's behavior. Furthermore, designers of the power system designated for facilities equipped with EAFs would benefit from this knowledge. Being aware of this fact, electrical engineers around the world have been investigating the working conditions of EAFs since their early introduction to in-

dustry. The key element to understanding the furnace is the arc phenomenon itself, which is the root of the nonlinearities and randomness of this load. Measurements and observations of the arc lead to the development of various theoretical models, some of which directly describe the relationships between the electrical properties of EAFs. The models vary in their theoretical background, complexity, or range of reflected arc features, and therefore in their accuracy. The simplest approaches lack stochastic properties of the arc but are easy to implement, while the most complex are better in reflection of randomness, but simultaneously they require larger computation power and are not as easy to be applied by the end user. Even the most accurate models available today have a limited background related to the stochastic features of the arc. This indicates room for improvement. Development of more accurate models would lead to a better understanding of such complex phenomena as the electric arc. Incorporation of a wide range of arc stochastic features into the model would make the analyses more reliable and trustworthy. Moreover, its implementation in suitable software would contribute to the promotion of such solutions to a larger audience. All of these actions could result in improvements in the design and analysis of power quality conditioning systems or components of power systems.

The main goal of the research presented in this thesis is to develop new and more accurate models of EAFs for the purpose of time-domain circuit simulations, based on different theoretical approaches and real measurement data. In terms of accuracy, the models should not only properly reflect the deterministic component of the behavior of EAFs, but also include representation of stochastic properties in a wide frequency range. The specific goals of the thesis include:

- extension of the existing deterministic model of the EAF based on the power balance differential equation to the random differential equation reflecting stochastic properties of the arc phenomenon,
- representation of the stochastic behavior of the arc using chaotic signals and artificial neural networks with different topologies,
- novel generalization of the power balance equation model to include fractional order operator,
- a multi-aspect comparative analysis of the developed models,
- implementation of selected models directly in the software dedicated to electrical circuit time domain simulations.

Moreover, all of the proposed models are intended to be developed based on real measurement data. The aim of this thesis is to analyze the versatility of the proposed approaches by investigating their application to the data obtained from three independent furnaces of different sizes.

The main hypothesis of this work is that it is possible to develop new stochastic models of the EAF based on different theoretical approaches using real measurement data, so that their accuracy is higher than existing deterministic-only models. Taking into account the main and specific goals, supplementary hypotheses have been formulated:

- it is possible to include physically interpretable stochastic processes in the power balance equation in order to improve the model accuracy,

- it is possible to fit selected chaotic systems so that the signals they generate represent stochastic processes in the power balance equation without reduction of accuracy,
- it is possible to train artificial neural network so that it can represent stochastic processes in the model based on power balance without reduction of accuracy,
- it is possible to generalize the power balance differential equation to fractional order differential equation to improve the model accuracy,
- it is possible to directly implement the best performing stochastic EAF model in the EMTP-ATP circuit simulation software.

The research presented in this thesis is subject to specific assumptions and limitations. The most significant is that the models considered are developed only for alternating current (AC), not for direct current (DC) EAFs and only with openly burning arcs, not submerged arc furnaces. Moreover, as described in detail in the following chapters, the thesis considers only the worst stage of the EAF work cycle, in terms of power quality. Although the proposed models can be modified for other stages, they are developed only for the melting stage. The analysis was carried out on the basis of measurement data obtained from three different-sized furnaces. Consequently, the proposed approaches can be applied for furnaces with different rated power, however, individual differences between installations with the same size are not considered. As for the electric arc phenomenon itself, the general approach is focused on the phase voltage and current waveforms. From this follows the assumption that random, automatic control, or human operator interferences with the furnace load, arc environment, or electrodes are already indirectly contained in the measurement data. Therefore, to conduct an effective analysis, various statistical methods are applied. Additionally, because the models are focused on a single arc and can later be extended to the three-phase version, the thesis applies a simplifying assumption that the influence of the three arcs in the three-phase EAF on each other can be omitted.

The thesis is divided into 10 chapters. This Chapter includes an introduction to the work, its conceptualization, as well as its main goals and scientific hypothesis. It is also devoted to a discussion of the current state of knowledge and a literature overview including the differential equation of power balance, which is a basis for the development of new EAF models. Chapter 2 consists of a description of the construction and operation of EAFs. It also includes details of the measurement data used for the development of the stochastic models described in the following chapters. Chapters 3-6 present a detailed description of both methods and results of development of the random differential equation (RDE), chaotic, ANN and fractional models, respectively. These chapters are followed by a comparative analysis of the models in Chapter 7. Chapter 8 is devoted to the implementation of a selected model in the EMTP-ATP simulation software. The thesis ends with a 9th Chapter with conclusions and an appendix containing a code of the model implemented in the EMTP-ATP software.

1.1 Literature overview

The first attempts at applying arc melting in industrial processes were conducted in the XIXth century. The first successful tests were carried out by Ernesto Stassano

and Paul Hérnoult, in Italy and France, respectively [1]. In the next decades, the technology was improved and gained popularity - more furnaces around the world emerged, and their rated power and capacity increased. Since the introduction of EAFs into the industry, this device has been an object of interest to researchers. After reaching levels of capacity surpassing 100 t in so-called Ultra-High-Power EAFs, their development focused on improving the steelmaking process itself. Such improvements included a reduction in heating time, enhancement of electrode control systems, and reinforcement of the refractory lining. Despite a long history, research related to issues that focus on energy efficiency is still of interest and is addressed with modern methodologies, for example, with machine learning methods, as in [2].

One of the aspects related to the improvement of EAF operation concerns its electrical properties. These are especially important considering not only the steel production process itself, but also the quality of the power in the power system to which the furnace is connected. Due to the strongly nonlinear and stochastic nature, the EAFs are especially problematic in terms of power quality. Among the problems they can cause are voltage harmonics, current harmonics, voltage sags or swells, and voltage flicker [3]. Similar problems can also occur in the case of DC furnaces [4]. Mitigating such issues requires the application of appropriate power quality improvement systems. Among common methods, there are installations with Static Var Compensators [5], [6], STATCOMs [7], Active Power Filters [8], and passive or hybrid filters [9]. To correctly choose and design an appropriate power quality improvement system, it is essential to have an accurate EAF model at disposal. Even the design stage of the entire facility that is intended to be equipped with EAF would benefit from accurate models because they can help with estimation of the electrical parameters needed for correct operation.

The problems of EAF modeling are extensively studied by researchers using various methods. In the past, some researchers developed frequency domain models, as in [10]. Nowadays, however, because of the importance of transients, time domain models predominate. Among time domain models, one can specify several of the most popular basic arc models, which are then improved or generalized. Very popular and simple models consist of an approximation of the EAF's V-I characteristic. It can be achieved using different functions fitted to the experimentally obtained data. In some cases the models are limited to approximation with a linear piecewise, hyperbolic, exponential, hybrid hyperbolic-exponential functions [11], [9], [6], [8], [7], [12] and other, e.g. cubic spline interpolation model [13]. The next commonly used group of arc models includes Cassie, Mayr, and hybrid Cassie-Mayr models [14], [9], [15], [16]. These take the form of dynamic models based on a differential equation with arc resistance as a state variable. The other group of arc models can be found with the radius of the arc column as a state variable. The most significant is the one based on the instantaneous power balance equation. Some approaches are based on analytical solutions of this equation [17], while others rely on numerical solutions [18], [19], [20]. Sometimes the integral form of the equation is used [21].

The basic models listed in the previous paragraph are most often enhanced by the application of various components, which are designed to reflect the random behavior of the electric arc phenomenon. One way is to use statistical methods, most often by the introduction of stochastic processes into the deterministic model. For example, certain regions of the EAF characteristic or waveforms can be represented

with the hidden Markov model as presented in [22] or [23]. A different way is based on superimposing a stochastic process onto the previously obtained deterministic data. The considered process can be, for example, a white noise as in [16], [24] or [25], autoregressive model [26] or combined autoregressive and moving average models [27].

Other methods of representing the random arc behavior are based on the application of deterministic chaos. Chaotic signals are then also superimposed on the previously obtained model output. In terms of applied chaotic systems, the Chua circuit is often used [28], [24], [18]. Other chaotic systems such as Lorenz, Rössler systems, or logistic map have also been applied [29], [30].

In addition to introducing purely stochastic or chaotic components, another popular method is to apply various ANNs for the purpose of EAF modeling. For example, in [31] or [27] authors used ANNs with the hyperbolic tangent sigmoid transfer function to represent the arc length in the arc model, while in [32] the authors applied the radial basis function network combined with the lookup table. In [33] in turn, the hybrid wavelet transform has been applied to model the EAF characteristic. In addition to shallow neural networks, deep learning methods are also applied in the field of EAF modeling, although, most often not for direct representation of the characteristic EAF. For example, deep learning can be applied to predictive compensation in power quality studies as shown in [34].

In terms of the application of fractional order system analysis in EAF modeling, the literature overview indicated a gap. To the author's current knowledge, the literature lacks publications considering the EAF model focused on the time domain simulations including fractional order methods. Instead, the only available research topics on EAF and fractional systems are devoted to control systems, as shown in [35].

The most common EAF modeling approaches have been presented in Fig. 1.1. Existing models often consist of the deterministic and stochastic parts. The first can be described with ordinary differential equations (e.g. Cassie, Mayr, or power balance models), directly by ANNs or various approximations. The stochastic part may be divided into low and high frequency components. Low frequency variations can be reflected using a stochastic, modulated, chaotic or ANN-based component added to the deterministic solution. The high frequency component, if included, can be directly represented with an additional stochastic signal.

The methods of EAF modeling presented in this Chapter strongly rely on numerical simulations conducted in various environments. Among the most popular software used for this purpose are: Matlab/Simulink ([7], [20], [16], [8], [6], [9], [13], [17], [33]), PSCAD ([27], [25], [36], [24]) and EMTP-ATP ([37], [30]). These programs are widely used by engineers around the world, making the considered EAF models available for replication or development by a larger audience. Additionally, they are often used by commercial and industrial users, increasing the usefulness of the proposed solutions.

The following chapters include results that are an extension and summary of research partially published in previous papers by the author [38], [39], [40], [41], [42], [43], [44], [45], [46].

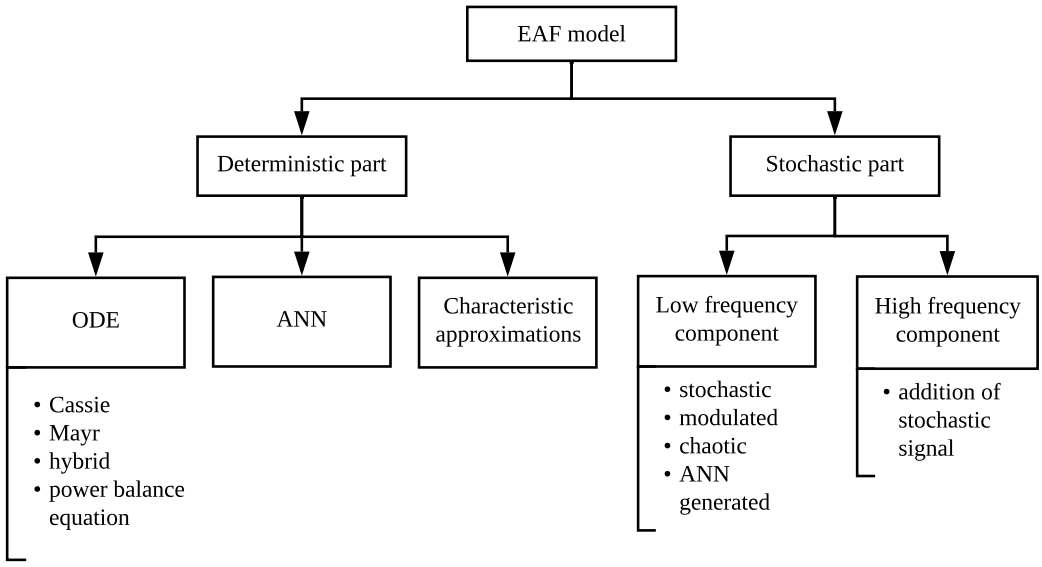

Fig. 1.1: Diagram presenting the most common strategies of EAF modeling.

1.2 Power balance-based EAF model

As stated in the previous section, the basic component of the EAF models is its deterministic part. It describes the fundamental behavior of the electric arc phenomena. Then it can be extended or enhanced with additional components, improving the accuracy of the model by including more realistic characterization of the disturbing load, such as EAF. Various deterministic models of the EAF exist, they can be based on a mathematical description of the voltage-current characteristic's shape, or the relationship between arc voltage and current as closed-form equations. In this thesis, the new proposed EAF models are based on the deterministic differential equation that describes the phenomenon of the electric arc using the principle of energy conservation. This model was first introduced in [47]. Its definition states that the electrical power delivered to the burning arc is balanced between two main components: the power transmitted to the environment as heat and the power increasing the energy accumulated internally by the arc column. It is worth noting that the applied model describes a single arc phenomenon. It binds quantities related to a single phase of the EAF and this model can later be extended for the description of each of the furnace phases by tripling its structure. Such a simplified model omits the influence of arcs on each other. Formally, the equation takes the following form:

$$k_1 r^n(t) + k_2 r(t) \frac{\mathrm{d}r(t)}{\mathrm{d}t} = \frac{k_3}{r^{m+2}(t)} i^2(t), \tag{1.1}$$

where:

$r(t)$ – arc radius,
$i(t)$ – arc current,
k_j – proportionality coefficients, $j = 1, 2, 3$,
n, m – parameters, $n = 0, 1, 2$, $m = 0, 1, 2$.

The arc voltage is then given by:

$$v(t) = \frac{k_3}{r^{m+2}(t)} i(t). \tag{1.2}$$

The model applies several assumptions regarding the electric arc phenomenon. The most fundamental one states that the arc column can be thought of as a cylindrical shape, which is approximately uniform throughout its length but may not be uniform throughout the cross-sectional area. In consequence, the energy balance depends on the volume of the column and therefore can be described mathematically using its length and radius. The first term of the sum in equation (1.1) is related to the cooling effect, and it uses the assumption that the heat transfer depends on the radius of the arc column. The arc's environment temperature influences the heat transfer, therefore when its hot, it can be simplified with $n = 0$. If the heat transfer is more efficient and the arc is long, it is assumed that $n = 1$ due to the proportionality of the cooling effect to the lateral surface. For a short arc, $n = 2$, since the cooling is proportional to the cross section of the arc. The second term assumes that the energy accumulated in the column is proportional to $r^2(t)$ and the rate at which it changes is described with derivative of that expression. The right side of the equation represents the total electrical power delivered to the arc, where the resistivity of the arc is assumed to be proportional to the term $r^{-m}(t)$. The parameter m equals 0, 1 or 2, which reflects the fact that the arc can be hotter near the center of its cross section.

When applying equations (1.1) and (1.2) to the EAF model, it is assumed that the parameters m and n are related to the phase of the furnace work cycle. For the melting stage, which is the main focus of this work, $m = 0$ and $n = 2$ are assumed. From now on, throughout the rest of the thesis, these values will be assumed constant and equal to those indicated above. However, the proportionality coefficients k_j should be estimated using empirical data. Most often, they are assumed constant. Exemplary values were estimated in [28] and equal to $k_1 = 3000$, $k_2 = 1$ and $k_3 = 12.5$, while in [23] they were estimated as: $k_1 = 2565$, $k_2 = 7.04$ and $k_3 = 26.7$. The exemplary voltage-current characteristic of the arc calculated using equations (1.1) and (1.2) and the coefficient values proposed by the authors cited have been presented in Fig. 1.2. The output voltage has been calculated with the assumption of a sinusoidal input current of 1000 A amplitude. As shown, their values strongly influence the characteristic's shape.

The model has been widely used in different electrical engineering applications. For example, it can be used to model the power system with PSCAD or EMTP-ATP software. Moreover, it has been pointed out as one of the most important arc models by the IEEE Task Force on Harmonics Modeling and Simulation [48].

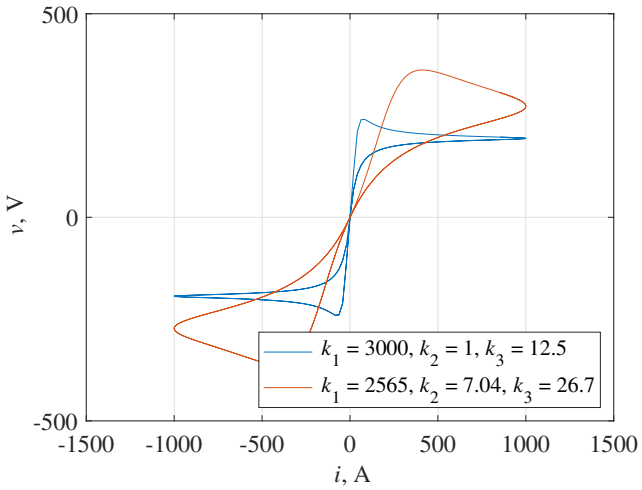

Fig. 1.2: Exemplary V-I characteristics of the arc calculated for sinusoidal current and two different sets of k_j coefficients [28], [23].

Chapter 2

Electric arc furnace

EAFs belong to the group of devices used for electrical heating in the industry. They use the heat generated by the electric arc phenomenon to melt the load and can operate with either a submerged or an open arc. Another classification can be made considering the type of power supply - DC or AC. Each type of device, although with many similarities, is characterized by different properties, construction, and power supply. This thesis focuses on the AC furnaces with an openly burning arc.

2.1 Installation description

2.1.1 Mechanical structure

As with any other device of this type, an EAF consists of mechanical and electrical parts. A general schematic of an early EAF construction has been presented in Fig. 2.1. Nowadays, the main structure does not change much. AC EAFs are mainly constructed as three-phase devices, which is important for structure construction. In terms of the mechanical part, an EAF consists of the hearth covered with refractory materials, resistant to very high temperatures. The metal load is placed inside the main chamber for the smelting process. The hearth usually has two or three main side openings, one for the slag tapping, sometimes a separate one for the molten charge tapping, and one for charging. The tapping is performed by tilting the whole furnace at an appropriate angle, allowing the liquid to flow freely due to the gravitational force. Depending on the size of the furnace, it can be charged through the charging door placed on the side (smaller EAFs) or from above (larger EAFs). Charging from above is available because in most cases the furnace's roof can be lifted and moved to the side, leaving the inside of the chamber exposed. Depending on the installation, the roof and chamber walls can be equipped with additional gear, such as oxygen lances or burners designed to improve the smelting process or water cooling systems designed to increase the service life of the construction. The size of industrial EAFs usually varies between 50 and 80 t (up to a maximum of 400 t [1]) of metal charge per one smelting cycle.

The EAF roof has three additional openings through which the graphite electrodes are lowered into the chamber. Electrodes wear out in the melting process. In time, they are not replaced, but extended by screwing a new segment at the top and appropriate positioning in the holder. The holder arms, separate for each electrode, are conductive and equipped with a water cooling system. Each horizontal arm is

mounted on a pillar on which it can move in a vertical direction using the positioning system driven by electric motors or other type of actuators. These are controlled either manually by the operator or, more commonly, by the dedicated automatic control system. The electrodes can be moved independently from each other.

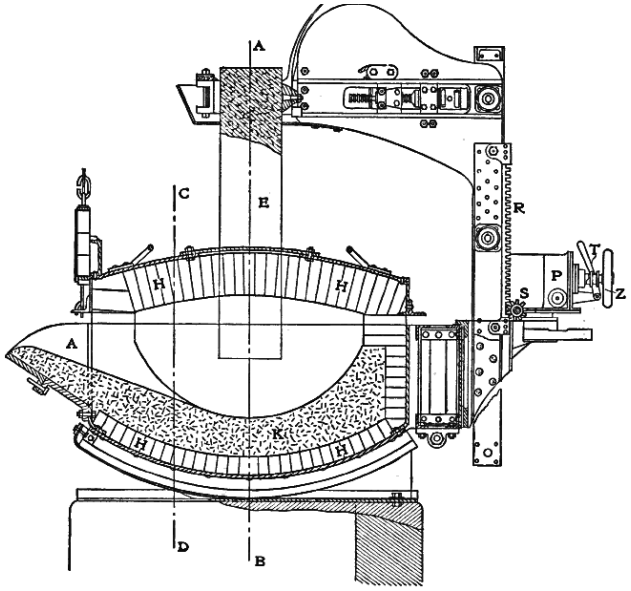

FIG. 306. — HÉROULT REFINING FURNACE.

Fig. 2.1: Schematic of the EAF construction [49].

2.1.2 Electrical circuit

The EAF's power supply consists of two main sections divided by the furnace transformer, which has a primary side with a medium voltage of the grid and a secondary side of low voltage and high current. The primary circuit is usually equipped with additional devices related to the operation of the grid, the improvement of power quality, and the regulation and control systems of the furnace. This equipment includes a disconnector, voltage and current transformers for auxiliary devices, circuit breaker, reactor with optional bypass, surge diverter, and installation of a local power quality improvement system.

The furnace transformer itself is a special transformer that reduces the medium voltage of the grid to a low voltage supplied to the electrodes. The transformer should be equipped with several taps for regulatory purposes. The secondary circuit must be designed to withstand tens of kA of current during normal operation, and surges related to the initial melting phase, where short circuit to the furnace load can occur repeatedly. The primary coils are most often connected in a star, whereas the secondary coils are connected in a delta connection.

Further, towards the furnace, the power is transferred through flexible cables to the electrode arms, allowing their unrestricted vertical movement. Cables can also be equipped with a water cooling system due to their severe working conditions. The working current of each phase then flows through the conductive arms and contact pads to the graphite electrodes. Each of the phase currents then passes through the burning arc column and reaches the common coupling point in the conductive metal

bath. The furnace hearth is usually grounded, that is why it is important to leave the transformer secondary circuit ungrounded.

Each element of the EAF installation contributes to the resistance and inductance of the circuit. This fact is especially important considering any measurements conducted in such a system. The presence of an electrode and cable impedance strongly influences the measurement of electric arc parameters, and the transformer impedance also has a considerable impact on the measurements if conducted on the primary side. In the case of steel furnaces, the resistance and reactance of the overall high-current circuit vary around $0.5 - 1.5\,\mathrm{m\Omega}$ and $2 - 5\,\mathrm{m\Omega}$, respectively. The part between the transformer bus bars to the electrodes can make up the most (around 60% [1]) of the circuit impedance. A simplified electrical circuit of the EAF power supply has been presented in Fig. 2.2. It consists of a HV/MV supply transformer (T_1) and an electric arc furnace MV/LV transformer (T_2). Next, X_{LSC} represents the short circuit reactance at Bus 1, L_f and R_f represent the inductance and resistance of the feeder connecting the supply transformer and the EAF transformer, L_c and R_c represent the equivalent impedance of flexible cables, bus conductors and graphite electrodes.

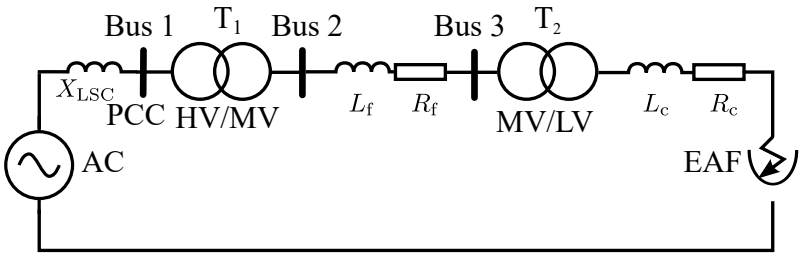

Fig. 2.2: Electrical circuit of EAF.

2.1.3 Operation principle

The EAF is designed for cyclic work. The cycle starts with a load charging when the scrap metal to be melted is placed inside the furnace. Next, the actual furnace operation starts - electrified electrodes are lowered into the furnace chamber, and when they reach a certain height in the proximity of the charge, the electric arc ignites. The heat generated by the arc starts the metal melting process. At the beginning of this phase, the metal is still in solid form with random and asymmetric placement. This causes the arc to ignite and extinguish repeatedly in a random and unstable manner. However, each time the arc burns, some part of the charge is melted, allowing the electrodes to go deeper into the hearth. Once the bottom layers of charge are reached, the volume of liquid metal at the bottom of the furnace allows the arc to burn more continuously. The phenomenon is then still very unpredictable and random, but the arc can be maintained as a continuous heat source. The melting stage lasts until the load is fully liquefied. The next stage is a refining one, where the molten metal bath is still being heated with more stable arcs. The metallurgical parameters of the load are measured and refined during this period. The last steps include deslagging and tapping of the molten metal with the desired properties, and the whole process is repeated for the next charge. If necessary, after cooling, EAF may be inspected and some maintenance of the refractory lining or other equipment can be performed.

2.2 Measurement data

From a power quality point of view, the worst conditions in the power system occur continuously during the melting phase, when the charge inside the furnace is still not completely molten. The physical conditions of the arc in such a relatively cold environment cause its instability and random behavior. This, in turn, leads to the occurrence of various power quality problems, such as harmonics, voltage flicker, or sags and swells. Because of this, it is important to focus on the modeling of this particular stage so that the simulation can consider the worst-case scenario. Only then could the equipment and design of the industrial facility with an EAF be accurate enough to withstand its continuous operation. This thesis is in particular oriented towards the development of such exact models of the EAF reflecting the melting stage.

The proposed models are based solely on actual measurement data collected during measurements of real and differently sized electric arc furnaces (EAFs). The difference in size, of course, translates into the difference in the range of measured quantities. As the EAF electrical circuit consists of several important elements, one can choose from multiple measurement points. Each point is characterized by its own advantages and disadvantages. Measurements on the high voltage side of the furnace transformer may be more feasible considering smaller currents, but it also requires appropriate medium voltage level probes. However, because of the influence of the transformer, the current and voltage waveforms at this point would be less distorted than those on the low voltage side. This means that the actual point of interest, which is the behavior of the arc and its influence, would not be directly visible. Next, the point at the low voltage side is characterized by easier voltage measurements because of low voltage; however, the current measurements are more complicated because of their very high amplitude, reaching several dozens of kA. Despite this, it is beneficial to place probes on this side of the transformer because the measured quantities would be far more accurate in terms of arc behavior reflection. In this case, the only factor that influences them would be the impedance of the electrodes and flexible cables. Another point of measurement that is theoretically available would be at the electrode mounting point. It allows the exclusion of the influence of the cable directly during the measurements, but unfortunately, due to very severe environmental conditions (temperature, dust, and harmful fumes) and movement of the electrodes, it is virtually impossible to install appropriate current and voltage probes at this location. However, it would be closest to the arc itself. Given the circumstances mentioned above, the best measurement location has been chosen as the low voltage side of the furnace transformer.

While taking measurements, the phase voltage and phase current of the electric arc have been recorded with a sampling frequency of 5 kHz for the small industrial EAF, 8 for the large industrial EAF and 10 kHz for the laboratory EAF. Any other quantity such as active, reactive power, or harmonics can be derived from such recordings at a later post-processing stage. In the case of such measurements, it is especially important to record all three voltages and all three currents of the three-phase device simultaneously, without delays at the single sample level. For this purpose, a suitable six-channel recorder has been applied. Three of the channels were equipped with differential voltage probes, and the other three with Rogowski coils with an embedded integrator, allowing for measurement of currents up to 30 kA.

The coils were placed on the bars on the low voltage transformer busbars, while the phase voltage was measured between each phase busbar and the EAF hearth. The outer hearth housing is usually grounded, therefore phase voltages are measured relative to the ground potential.

2.2.1 Large industrial EAF

The first installation from which the measurement data has been obtained is a large industrial EAF located in Iran [1]. Its rated power is equal to 70 MW. It is a high-power industrial installation with a 400/63/33 kV transformer that connects the 400 kV grid to a 63 kV EAF busbar and a 63/0.718 kV furnace transformer. Three-phase voltages and currents have been presented in Fig. 2.3 on both long and short time scales. For this dataset the powers related to the melting process were changing, as shown in Fig. 2.4. Due to its size and significant influence on power quality, it has been a primary dataset used for the development of EAF models. The second and third considered installations described in the following sections have been included to investigate the versatility of the proposed modeling methods.

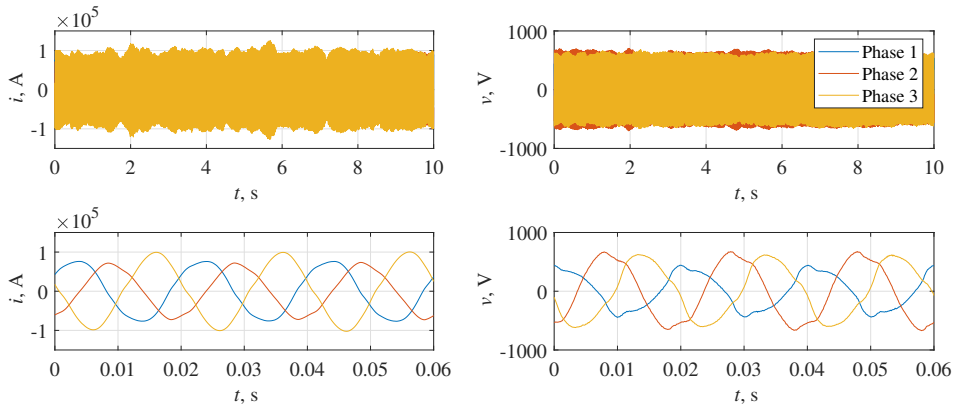

Fig. 2.3: Phase voltage and current waveforms measured in the large industrial EAF.

For arc modeling purposes, the data had to be cleared by subtracting the voltage drop that occurs across the cables and the electrode impedance. Resistance and reactance values per phase in this particular furnace were equal to R = 0.33 mΩ and X = 2.26 mΩ. The influence of those voltage drops is significant from the point of view of arc modeling. This influence has been visualized in Fig. 2.5 on the example of several consecutive measured single phase voltage periods.

2.2.2 Small industrial EAF

To broaden the analysis and provide better accuracy of the proposed models in addition to their generality, the next measurement has been carried out in another EAF. In this case, it was a smaller installation, which additionally provides information

[1] The measurement data have been obtained from EAF located at the Mobarakeh Steel Company in Isfahan. The data have been provided by Prof. Haidar Samet, who also used them in his own research, e.g. [14].

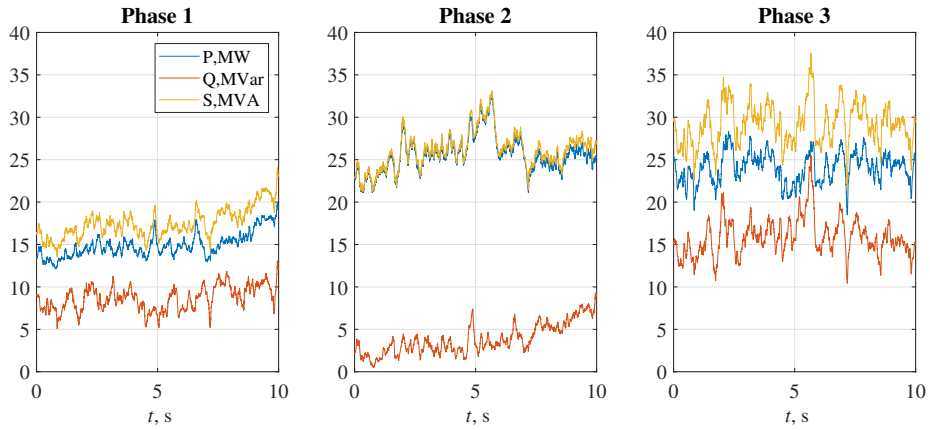

Fig. 2.4: Active, reactive and apparent power of each phase of the melting process of the large industrial EAF.

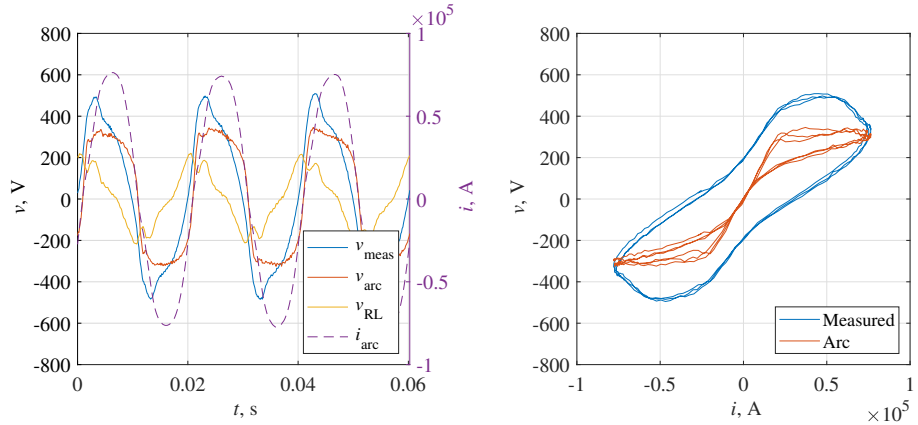

Fig. 2.5: Measured voltage waveform compared with cables and electrodes voltage drop and arc voltage itself for the large industrial EAF.

about the scalability of the phenomena and models considered. This furnace is located in a facility in Gliwice, Poland [2]. It has a capacity of 0.6 t of steel charge, which is significantly less than the device considered in Subsection 2.2.1. The furnace has been presented in Fig. 2.6.

The measured three-phase voltages and currents have been presented in Fig. 2.7 on both a long and short time scale. For this dataset the powers related to the melting process have been changing, as shown in Fig. 2.8.

Again, for this EAF, the data were cleared by subtracting the voltage drop occurring across the cables and the electrode impedance. For this particular furnace, the impedance components have been estimated as R = 2.5 mΩ and X = 0.15 mΩ. This influence has been visualized in Fig. 2.9 on the example of several consecutive measured single phase voltage periods.

2.2.3 Laboratory EAF

Access to real, especially large EAF installations, is often limited, due to the fact that it disrupts the normal operation of the facility. If the works are not part

[2]The data have been obtained at ZDWO steel and cast iron foundry in Gliwice.

Fig. 2.6: Photos of the small industrial electric arc furnace.

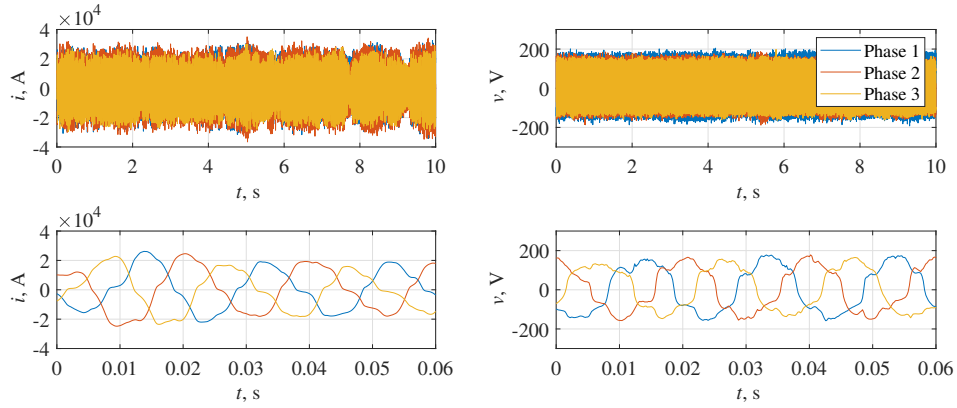

Fig. 2.7: Measurement phase voltage and current waveforms in the small industrial EAF.

of a commissioned action, it may be difficult to examine the furnace and be able to conduct repeated measurements. Additionally, performing any additional tests unusual for the classic work cycle can be either impossible or prohibited by facility staff. Because of that, to be independent from such conditions and for further scalability analysis, a special dedicated laboratory station has been constructed. The laboratory station is designed to represent a very small scale EAF. The maximum power of the laboratory station furnace is estimated to be 20 kVA with a crucible capacity of around 2 kg.

For this purpose, the three-phase transformer was replaced with three single-phase welding transformers equipped with a dedicated cooling system and an overheating indicator. Similarly to the real size EAF, the power from the transformer is transferred to the hearth through flexible cables and graphite electrodes placed in copper holders. The holders are attached to a vertically moving rack, driven manually by a handwheel. The system is equipped with input current measurement

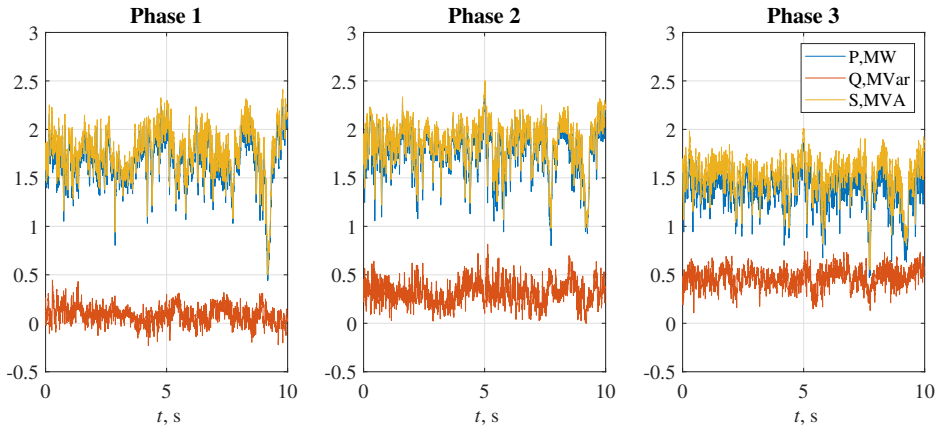

Fig. 2.8: Active, reactive and apparent power during the melting process of the small industrial EAF.

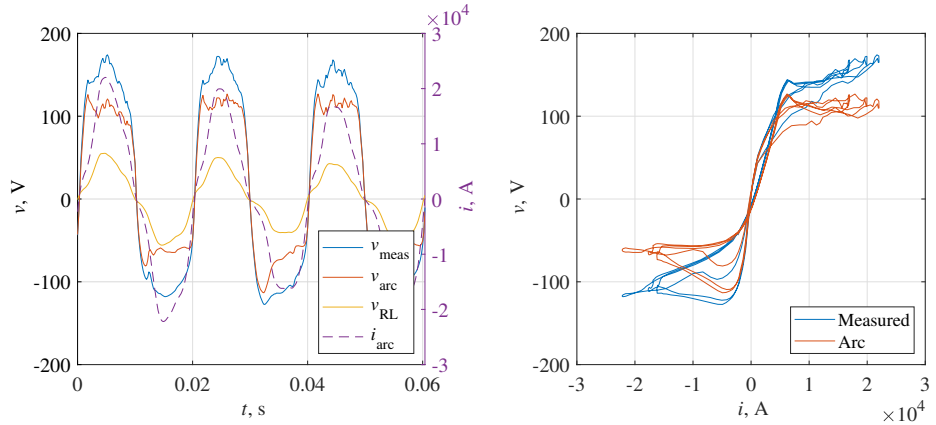

Fig. 2.9: Measured voltage waveform compared with cables and electrodes voltage drop and arc voltage itself for the small industrial EAF.

conducted with an analog ammeter, a switching gear allowing various operating modes including single- or two-phase operation, and a main chamber temperature control and fume extractor. The hearth consists of a graphite crucible protected with additional refractory bricks. The station has been presented in Fig. 2.10

A difference between the laboratory EAF and larger installations, apart from its flexibility and ability to easily change its structure, is that the measurement probes can be placed closer to the actual electric arc phenomena. In this case, the influence of flexible cables can be minimized but not completely eliminated. Additionally, for the purpose of a more detailed analysis of the arc behavior, the measurements were focused on the dataset captured during the melting stage, in which only two electrodes have been powered. One of them has been placed in the crucible to provide short-circuit connection to the load, while the second has been in proximity of the metal, allowing ignition of the arc.

The measured voltage and current have been presented in Fig. 2.11 in both long and short time scales. For this dataset the powers related to the melting process have been changing, as shown in Fig. 2.12.

Again, for this EAF, the data were cleared by subtracting the voltage drop that occurs on the cables and the impedance of the electrode. This particular furnace

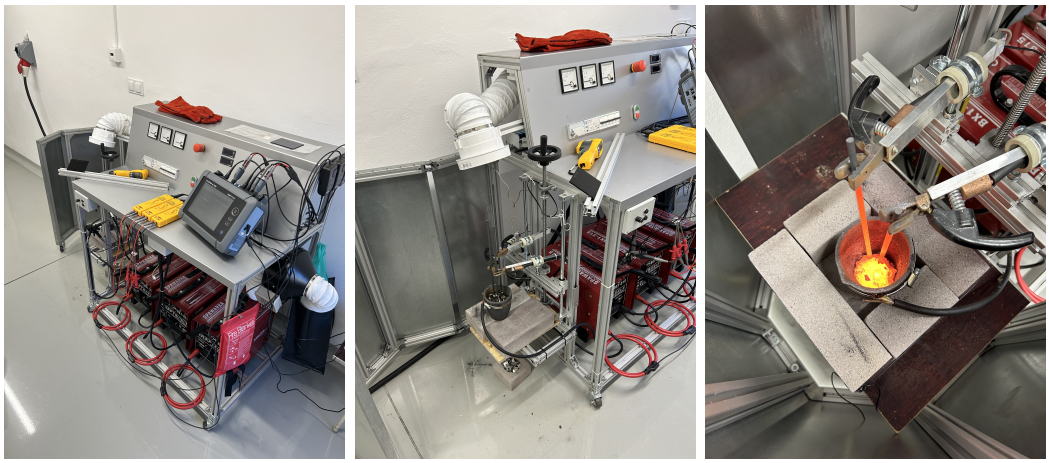

Fig. 2.10: Photos of the laboratory scale electric arc furnace.

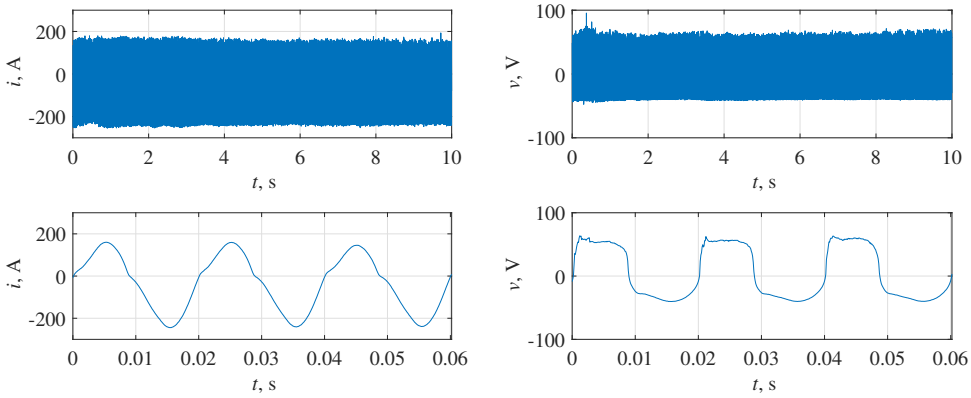

Fig. 2.11: Measurement phase voltage and current waveforms in the laboratory EAF.

had an estimated R = 55 mΩ and the negligibly low reactance. This influence has been visualized in Fig. 2.13 on the example of several consecutive measured single phase voltage periods.

As shown in this Chapter, the scale of the furnace considered significantly influences the measurement data. The influence of the flexible cable parameters is much more considerable in larger installations. For the smaller furnaces, the measured V-I characteristics are more similar to the actual arc characteristic. Moreover, the smaller the furnace, the more visible is the asymmetry between the positive and negative parts of waveforms. This effect is very significant in the laboratory EAF. It is related to the scale of the investigated phenomena. On a smaller scale, where the environment of the arc and load is characterized by different thermodynamical properties, it is more evident that the direction of current flow influences the voltage and current waveforms. As observed, the arc rectification effect occurs, which is related to difference in emission of the electrical charges from steel and graphite. Similar phenomena had been used in industrial rectifiers in the pre-semiconductor era, e.g. in mercury vapor arc rectifiers [50]. Namely, lower resistance is posed by the arc column, while current flows from the steel to the graphite electrode, and higher resistance in the opposite direction. Along with lower resistance, the more visible high frequency random variations of the signals are observed.

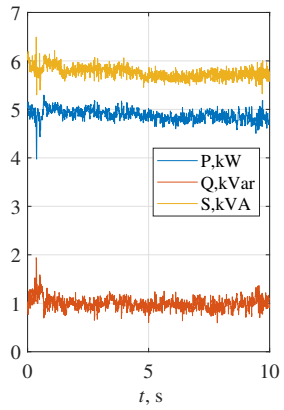

Fig. 2.12: Active, reactive and apparent power of each phase of the melting process of the laboratory EAF.

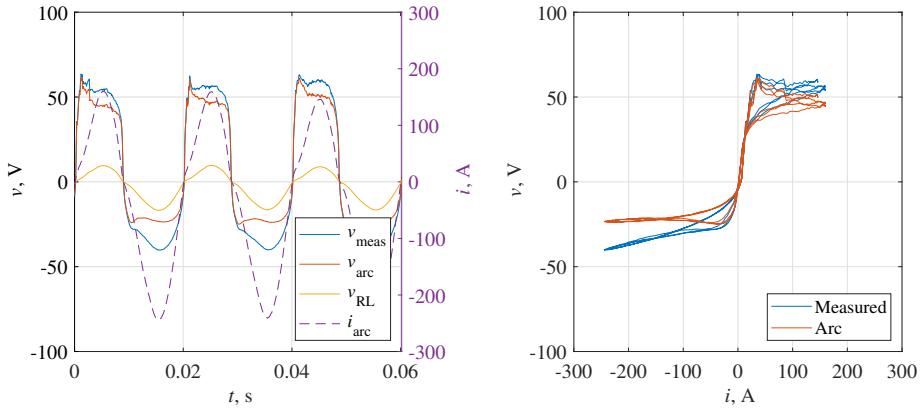

Fig. 2.13: Measured voltage waveform compared with cables and electrodes voltage drop and arc voltage itself for the laboratory EAF.

Chapter 3

Stochastic EAF model

The effects observable in the electric arc phenomenon are random in their nature, therefore any measured quantities can be thought of as realizations of some stochastic processes. Assuming that the fundamental behavior of the arc can be approximately described with deterministic relationships, the model can be improved by incorporating a stochastic component into its structure. Such a stochastic component is usually designed as an additive or multiplicative term, which appears in deterministic equations. However, that kind of solution requires the introduction of a new term that acts as a stochastic ingredient. This section describes a solution where the k_j coefficients of the equation (1.1) are considered to be stochastic processes. A physical interpretation of this assumption is related to dynamic and random environment conditions in the EAF hearth in close proximity to the arc column. The rate of arc cooling and energy accumulation, as well as the conductivity of the arc, can be subject to variations due to changes in position of the furnace charge, speed of its movement, and thermodynamical processes. Those variations can be reflected in the proportionality coefficient values, and as such they can change throughout the melting process.

3.1 EAF random differential equation

The general methodology described in this section is related to representation of random phenomena occurring in the electric arc, with stochastic processes. Measurement data indicate that such random variations can be observed in a wide frequency spectrum. Consequently, two main stochastic components can be specified: low and high frequency. The first is related to the general shape of the EAF V-I characteristic, while the second is mainly related to the high frequency ripples visible especially in the voltage waveforms, e.g. around its peak values. Both of them can be reflected separately with certain stochastic processes.

The low frequency component can be described based on a power balance equation (1.1) into which stochastic processes are incorporated. Because the equation consists of three terms with three coefficients, it is also possible to rely on its reduced form obtained by division of the equation by one of the coefficients. A diagram describing possible structures of the RDE model has been presented in Fig. 3.1. As shown, the model can consist of two components; low frequency and high frequency components. The first one can be reflected on the basis of a full power balance model with three stochastic processes representing its three coefficients. Optionally, it can

be reflected with a reduced form of the power balance model with only two stochastic processes representing its two coefficients. The high frequency component itself can be treated as a separate stochastic process. Each of the stochastic processes present in the chosen model should be identified based on the measurement data. The identification procedure can be done in two different ways. The first relies only on an identification of the distribution of the process values. Such an approach results in the generation of a white noise process with an empirically specified distribution. It does not include any possible dependencies between consecutive values. The second way is an extended version in which a whole stochastic process should be identified, including the correlation of consecutive values, where e.g. an ARIMA model can be applied [51].

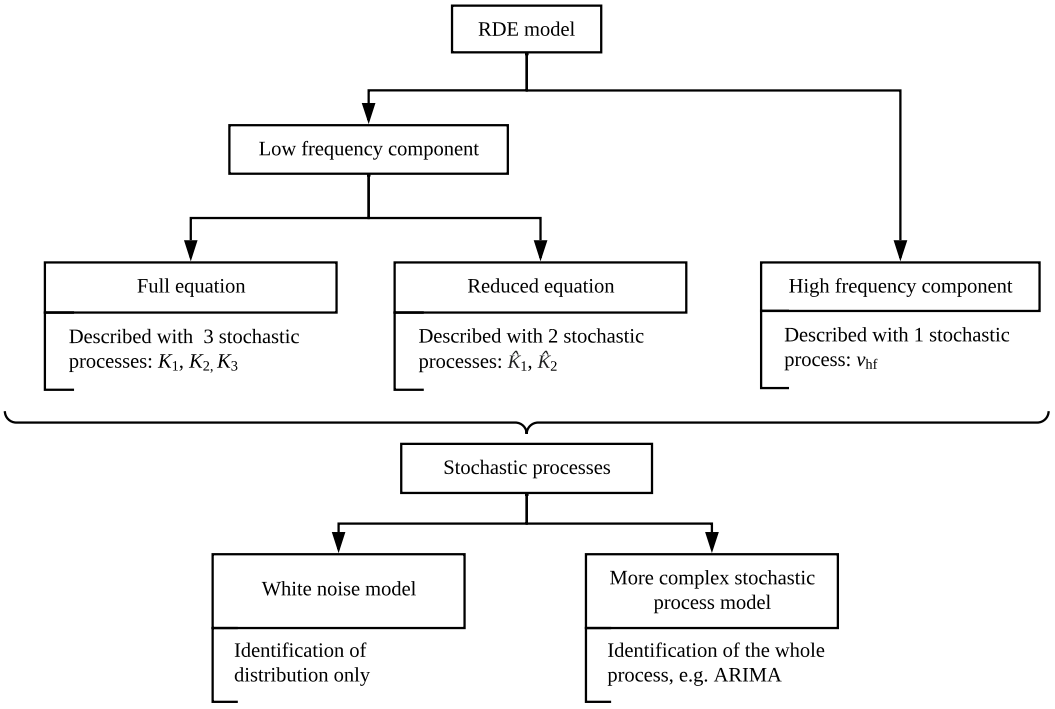

Fig. 3.1: Diagram of possible RDE model structures.

The assumption that the k_j coefficients are, in fact, the stochastic processes K_j[1] results in the transformation of the original power balance model into a random differential equation, where each quantity is also represented by a stochastic process:

$$K_1(l)R^2(t) + K_2(l)R(t)\frac{dR(t)}{dt} = \frac{K_3(l)}{R^2(t)}I^2(t), \tag{3.1}$$

where:

$K_j(l)$ – model coefficients represented by discrete-time stochastic processes for $j = \{1, 2, 3\}$,

l – current frame index, $l = \left\lceil \frac{t}{T_w} \right\rceil$,

[1]Notation of uppercase K_j refers to the stochastic processes representing variations of the power balance equation coefficients, while lowercase k_j is used to refer to constant values of coefficients in a single considered frame.

T_w – length of a frame,
$R(t)$ – arc radius stochastic process,
$I(t)$ – arc current stochastic process.

Thus, a modified equation for calculating the arc voltage can be expressed as:

$$V(t) = \frac{K_3(l)}{R^2(t)} I(t). \tag{3.2}$$

Stochastic processes K_j must be identified. A procedure has been proposed that leads to the estimation of the coefficient values based on the measurement data. The details of this procedure have been presented in [38]. The coefficient estimation process assumes that the coefficients remain constant for a certain time frame and then change their values for the next frame. A detailed investigation of the influence of frame length and starting point has been carried out. Fig. 3.2 presents the configurations that have been analyzed. The analysis indicated that for the dataset where the V-I characteristic is symmetrical in positive and negative planes, the optimal solution is that the frame starts with waveform's zero-crossing and has length equal to the signal's period (version B). In the case of asymmetry between the positive and negative parts of the characteristic, a half-period long frame is more appropriate (version C).

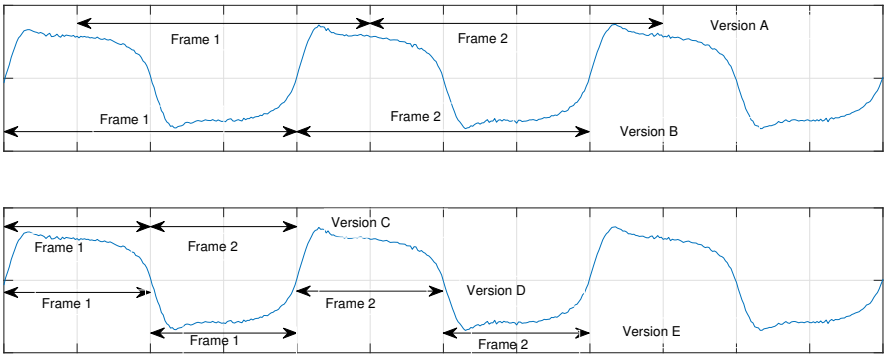

Fig. 3.2: Graphical presentation of investigated K_j coefficients frames and starting points.

This assumption leads to a further estimation process in which the data were divided into frames. Then, for each frame separately, the measured current waveform was considered as input for the power balance equation, allowing the calculation of the voltage as output. First, the calculation was performed using an arbitrarily chosen set of coefficient values k_j. The essence of the estimation procedure is to optimize the coefficient values k_j for each frame separately to minimize the discrepancy between the simulated output voltage and the measured voltage related to the appropriate frame. For this purpose, the goal function was proposed in the form of root mean square error (RMSE):

$$\min_{k_1,k_2,k_3} \sqrt{\frac{1}{N}\sum_{i=1}^{N}(v_i - \hat{v}_i)^2}, \tag{3.3}$$

where:

v_i – i-th sample of the measurement voltage,
$\hat{v}_i$ – i-th sample of the simulated voltage,
N – number of samples in the considered frame.

The optimization was carried out using genetic algorithm (GA), which is a universal tool suitable for various types of problems, especially multivariate optimization with complex goal function. In this procedure, a set of coefficient values k_j is encoded on a chromosome representing one of the possible solutions. Initially, a whole population is generated with respect to user-defined boundaries and constraints. Then each individual is evaluated on the basis of the goal function, which in this case is an RMSE value describing the error between the simulated and measured voltages. Based on the evaluation process, a new population is created following rules representing the biological processes of natural selection: selection of the best individuals, crossover of chosen individuals, and mutations in some of their chromosomes. This process leads to the acquisition of a new population. More specifically, the GA approach uses a selection method based on moving along a line, where parents are represented proportionally to their goal function value, with steps of equal size. Most of the new individuals in the next generation, namely 80%, are obtained through a crossover, which is done by creating a random binary vector that determines the origin of the genes. Genes corresponding to value 1 in the binary vector are taken from the first parent and those corresponding to 0 are taken from the second parent. Mutation is the second process that takes place when creating a new generation. It makes small random changes in individuals in the population to create mutation children. The mutation in GA is carried out using a function that randomly generates the direction and step by which the decision variable changes. These parameters are adapted to the scores of the previous generation. Furthermore, 5% of the best individuals are passed on unchanged to the next generation. The whole cycle is then repeated until stopping conditions are met, which can be defined using the maximum generation value or with respect to the change in the best individual goal function value. After reaching an optimal solution for the initially selected frame, the values of the k_j coefficients are saved, and optimization is performed again for the next frame. The whole process has been presented in a flowchart in Fig. 3.3.

Due to the fact that equation (3.1) has three terms and three coefficients, it is possible to reduce the number of the unknown variables by dividing the equation with one of them. Consequently, it leads to the reduction of the number of stochastic processes to be identified from three to two. Here, a division of the whole equation by K_1 is proposed because of its highest values. This operation results in the simplification of RDE in the following form:

$$R^2(t) + \hat{K}_1(l)R(t)\frac{dR(t)}{dt} = \frac{\hat{K}_2(l)}{R^2(t)}I^2(t), \tag{3.4}$$

where:

$$\hat{K}_1(l) = \frac{K_2(l)}{K_1(l)}, \quad \hat{K}_2(l) = \frac{K_3(l)}{K_1(l)}, \quad \text{for} \quad K_1(l) > 0. \tag{3.5}$$

The last step that leads to the acquisition of a standalone RDE model is to take the obtained realizations of the stochastic processes, either K_1, K_2 and K_3 or $\hat{K}_1$

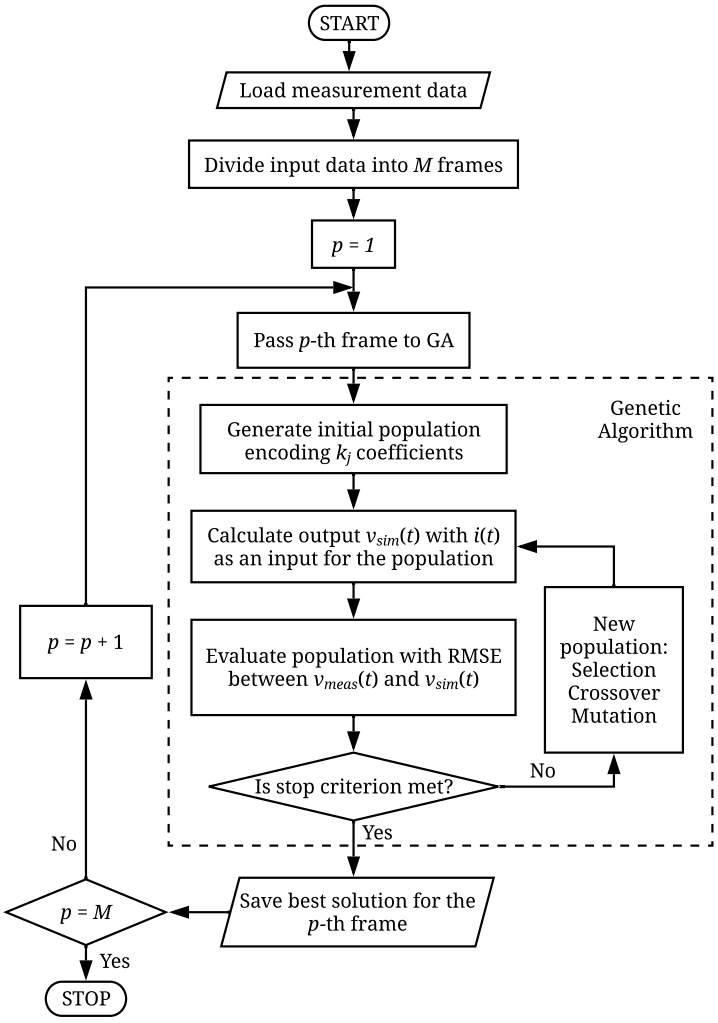

Fig. 3.3: Flowchart of the GA optimization process.

and $\hat{K}_2$ and analyze them to actually identify them. To do so, it is important to consider the distributions of the data itself, its autocorrelation function, and the partial autocorrelation. The information given by this statistical analysis is helpful in choosing the best-fitting stochastic process model. After choosing one, it is also important to test the distributions of residuals that would be left after applying the chosen stochastic process model. A set of data with the type of stochastic process and the distribution of its residuals can be considered as a complete RDE model. Any implementation knowing the definition of the stochastic process would be able to generate such realizations independently.

The procedure described in the previous subsection is limited to the components that can be reflected in the power balance-based model and changes in the general shape of the EAF V-I characteristic. However, apart from such variations, the measurement data also contain a high frequency component which is best visible in the voltage waveform, especially around peak values. To incorporate such phenomena into the RDE model, a separate stochastic component is applied. It consists of a voltage signal added directly to the output voltage obtained from a previous version of the model. However, in this way, a general operating point would not change,

assuming that linearization of the characteristic in strict proximity around the operating point allows for a simple summation of those two components. In order to actually identify the high frequency component first, the measured voltage waveform has been filtered using a high-pass FIR filter. It is worth mentioning that the cut-off frequency of the filter is chosen based on the capacity of the low frequency component model. The base model is capable of reflecting signals up to 600 Hz, and thus the frequencies higher than that are points of interest for high frequency component models. The obtained signal is then considered as a separate stochastic process. An analysis based on distribution of the values, autocorrelation function, and partial autocorrelation function is repeated in order to select the best fitting stochastic process model. Details and results have been presented in the following section.

3.2 Simulation results and analysis

The procedures described in the previous sections have been used for the development of three models, each reflecting the behavior of EAFs with different sizes. In the next subsections, the numerical results for the modeling of large industrial, small industrial, and laboratory EAFs have been presented. The primary models for each furnace are constructed with a low frequency component represented with a full equation with three stochastic processes reflected with a simplified white noise process of suitable distribution according to Fig. 3.1. Additionally, each contains a high frequency component identified as a stochastic process more complex than a simple white noise. The fourth subsection has been introduced to present the possibility of extended analysis of a low frequency component represented with a simplified equation with two stochastic components identified as more complex stochastic processes from the ARIMA group. This extended analysis has been performed based on the large industrial EAF dataset.

3.2.1 Analysis of K_1, K_2 and K_3 for the large industrial EAF

For the measurement data obtained from the large industrial EAF, the estimation of the coefficients k_j has been carried out separately for every period-long frame. The frame starting point was set to zero crossing at the rising edge of the waveforms. As described in the previous section, this led to the acquisition of three separate realizations of discrete-time stochastic processes K_j. These realizations have been shown in Fig. 3.4. The next graphs presented in Fig. 3.5 and Fig. 3.6 show results of further statistical analysis - autocorrelation functions, and distribution of values and their increments. As presented, the realizations themselves exhibit stochastic behavior. The autocorrelation and partial autocorrelation functions clearly suggest a significant correlation in some cases, but their character differs between different coefficients. A visualization of 3D histograms also highlights that the realizations oscillate in a stable way around some central location - larger values are accompanied by negative increments and vice versa. This suggests that the process being considered is stationary.

To provide a quantitative measure of the improvement of the EAF model caused by the introduction of variable coefficients k_j, their optimal values have been calculated considering that they are constant throughout the measurement data set.

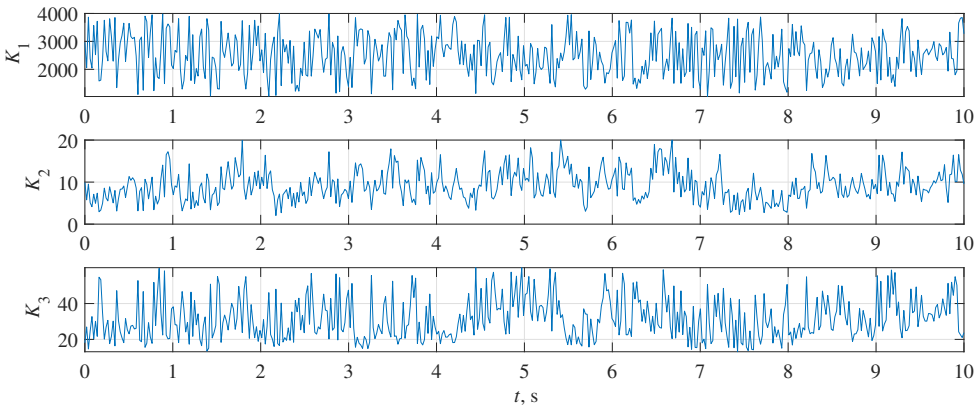

Fig. 3.4: Realizations of K_j stochastic processes estimated from large industrial EAF measurement data.

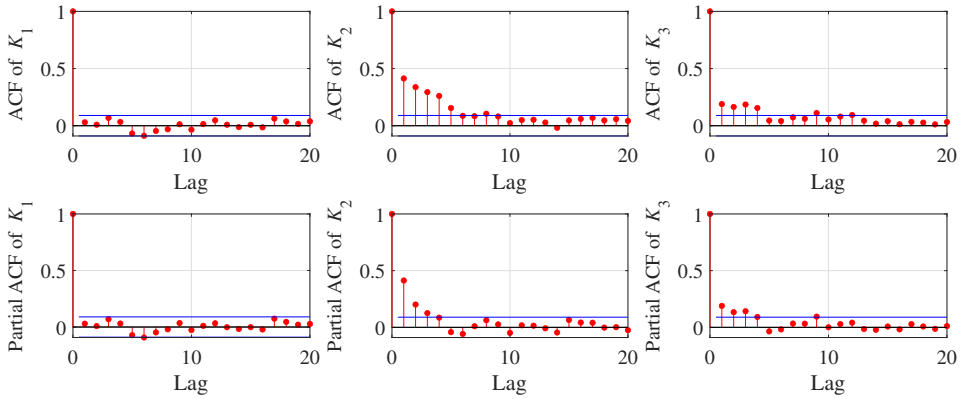

Fig. 3.5: Autocorrelation and partial autocorrelation function of realizations of K_j stochastic processes obtained from large industrial EAF measurement data.

That case was compared to the solution, where they vary from period to period. As a result, the reduction in the RMSE error reached 27%. The details of the results have been gathered in Table 3.1. These results clearly justify the introduction of the proposed approach.

The values of k_j in this simulation have been generated randomly for each frame from their actual distributions shown in Fig. 3.6. The applied method was an inverse cumulative distribution function (CDF) method, which allowed the drawing of random variables from the empirically obtained distribution [52]. The exemplary output voltage realization has been presented in Fig. 3.7. As depicted, the model exhibits behavior similar to that of the measurement data.

As indicated in Chapter 2, apart from low frequency changes in the EAF voltage, there are high frequency stochastic components visible. The application of the high pass filter to the voltage measurement allowed one to obtain a signal presented in Fig. 3.8. As shown, the waveform seems stochastic. Analysis of the autocorrelation function and partial autocorrelation function of the signal and its increment has been presented in Fig. 3.9. The analysis suggests that data can be represented with a model from the ARIMA group, but much simpler, reduced only to the moving average (MA) process. In this case, the MA process has four components. The

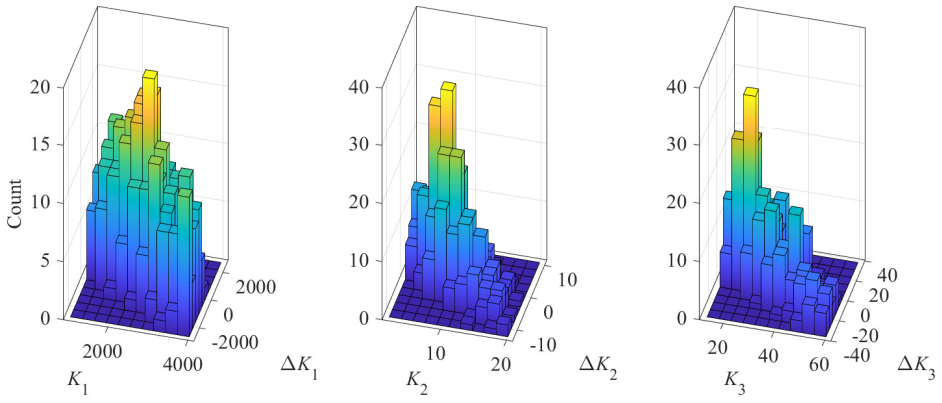

Fig. 3.6: Three dimensional histogram of raw values and their increments of realizations of K_j stochastic processes obtained from large industrial EAF measurement data.

Table 3.1: Comparison of approaches with constant and variable values k_j for the large industrial EAF.

	Constant coefficients	Stochastic processes	Relative change
Fitted values	$k_1 = 2213.3$ $k_2 = 7.46$ $k_3 = 31.82$	k_j variable	-
RMSE	3.2	2.4	-27%

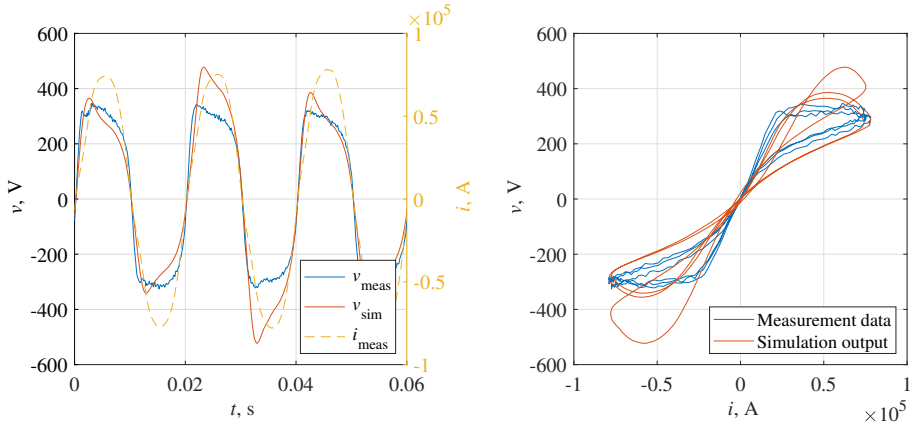

Fig. 3.7: Short-term current and voltage waveforms and characteristic of the EAF single phase arc measured during the melting stage compared to the simulation output for the large industrial EAF.

MA model has been fitted to the measurement data, resulting in the estimation of the following coefficients: $MA_1 = -0.417$, $MA_2 = -0.521$, $MA_3 = -0.140$ and $MA_4 = 0.086$. A signal generated with this MA model has been added to Fig. 3.8 with measurement data.

The overall RDE standalone model can be implemented by applying the power balance equation with k_j coefficients generated independently for the consecutive

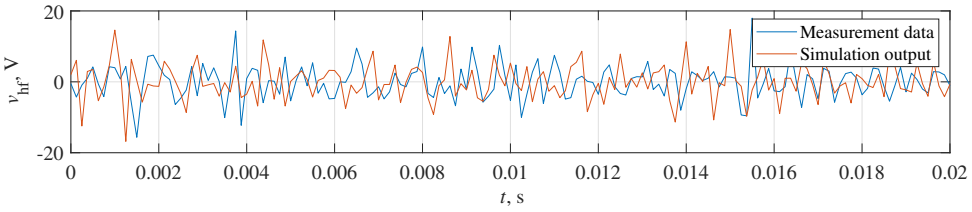

Fig. 3.8: High frequency component of large industrial EAF voltage waveform.

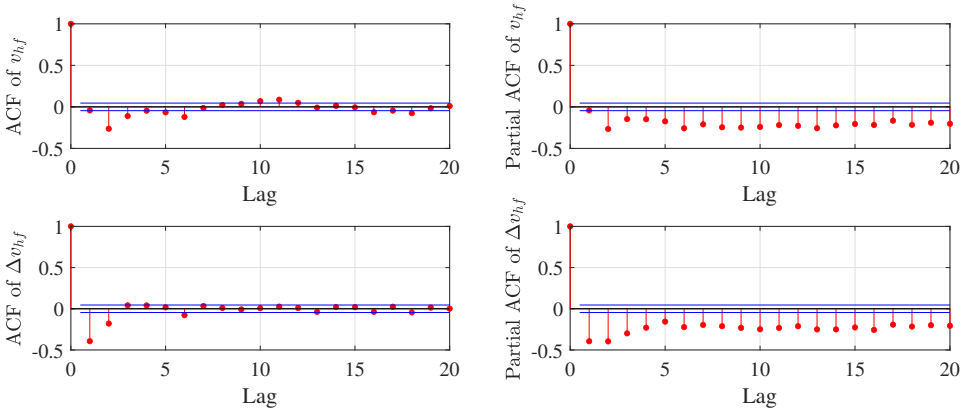

Fig. 3.9: Autocorrelation and partial autocorrelation function of the high frequency voltage component for the large industrial EAF.

frames by discrete time stochastic processes described in this section with an additional high frequency voltage signal simply added to the output voltage. An example of such a waveform and the V-I characteristic obtained with a complete RDE model have been presented in Fig. 3.10. As shown, the overall effect reflects stochastic variations in the EAF characteristic in a wide spectrum of frequencies.

3.2.2 Analysis of K_1, K_2 and K_3 for the small industrial EAF

For the purpose of investigating the versatility of the proposed approach, the procedures described in previous sections have been repeated for the small industrial EAF measurement dataset. Due to little but visible asymmetry between positive and negative parts of the waveforms, this dataset has been divided into half-period long frames based on the detected zero crossings. This type of division has been marked as Version C in Fig. 3.2.

The realizations of the processes K_j for this case have been presented in Fig. 3.11. Compared to the realizations obtained from a large industrial furnace, the distributions and range differ significantly. However, the stochastic behavior of the series is retained. Similarly to the previous section, the autocorrelation and 3D histograms of the realizations and its increments have been calculated and showed in Fig. 3.12 and Fig. 3.13. In this case, there is a significant negative autocorrelation in K_1 and especially K_3, which is related to the fact that consecutive samples are related to the half of the period with the opposite sign and shape. This effect is not present in the realization of K_2. Histograms suggest that these processes again vary around a certain level, without any long-term drift in either a positive or negative direction.

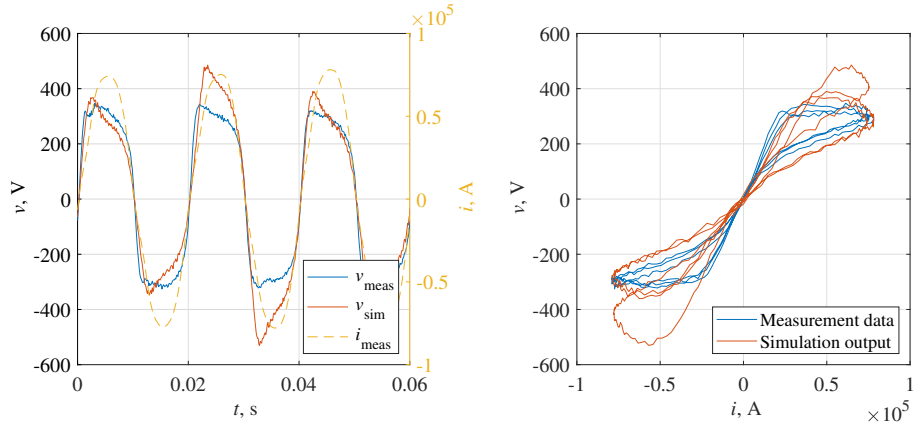

Fig. 3.10: Short-term current and voltage waveforms and characteristic of EAF single phase arc measured during the melting stage compared to the overall simulation output (with both low and high frequency components) for the large industrial EAF.

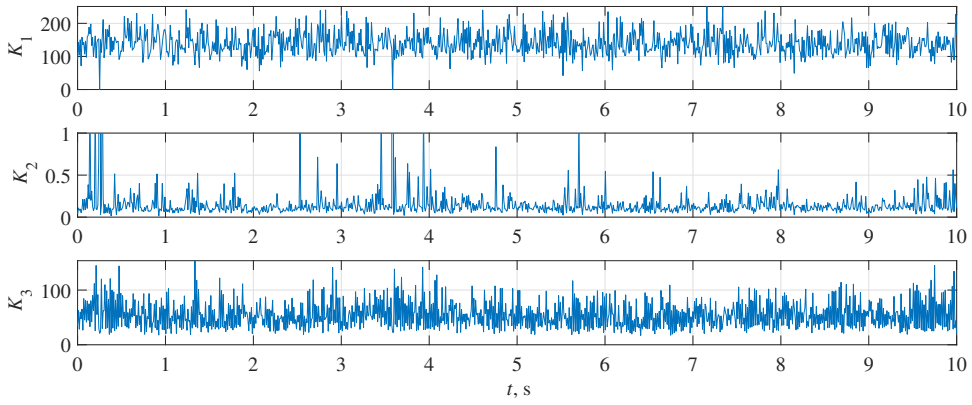

Fig. 3.11: Realizations of K_j stochastic processes estimated from the small industrial EAF measurement data.

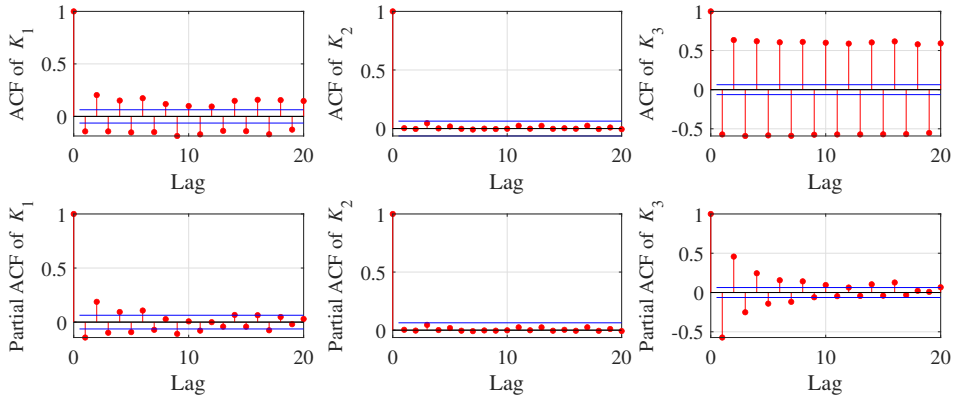

Fig. 3.12: Autocorrelation and partial autocorrelation function of realizations of K_j stochastic processes obtained from the small industrial EAF measurement data.

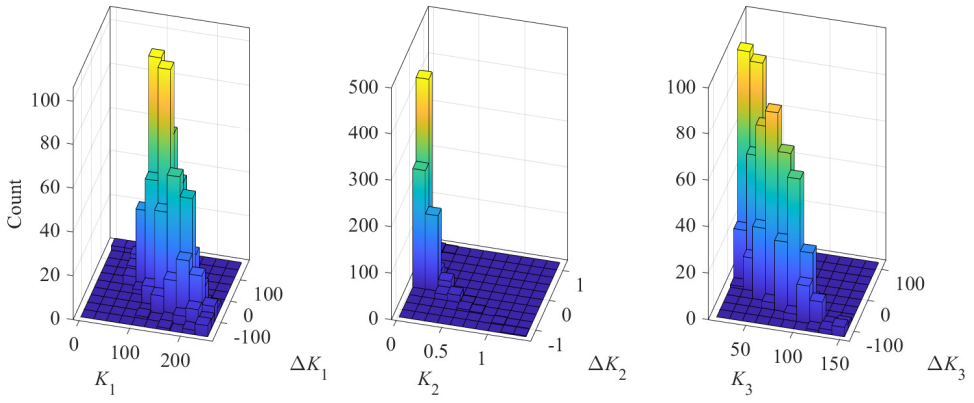

Fig. 3.13: Three dimensional histogram of raw values and their increments of realizations of K_j stochastic processes obtained from the small industrial EAF measurement data.

Table 3.2: Comparison of approaches with constant and variable k_j values for small industrial EAF.

	Constant coefficients	Stochastic processes	Relative change
Fitted values	$k_1 = 62.15$ $k_2 = 0.05$ $k_3 = 114.46$	k_j variable	-
RMSE	23.9	14.0	-41%

In addition to the graphical representation of the realizations and some of their statistical properties, an investigation has been conducted to determine whether this approach improves the accuracy of the small industrial model EAF. Similarly to the large industrial EAF, Table 3.2 presents the rate of improvement in terms of RMSE error between the constant k_j (optimal for the entire dataset) and stochastic K_j. As shown, the improvement reaches approximately 40%, which is an even better result than for the large industrial furnace.

Additionally, a complete model has been developed to compare the overall RDE approach. The values of k_j in this simulation have been generated randomly for each frame from their actual distributions shown in Fig. 3.13. The applied method was an inverse CDF method, which allowed the draw of random variables from the empirically obtained distribution. The exemplary output voltage realization has been presented in Fig. 3.14. As depicted, the model exhibits behavior similar to that of the measurement data.

In the case of the small industrial EAF the high frequency component has also been analyzed. The application of the high-pass filter to the voltage measurement allow the obtaining of a signal presented in Fig. 3.15. As shown, the waveform exhibits stochastic behavior. The analysis of the autocorrelation and partial autocorrelation function of the signal and its increment has been presented in Fig. 3.16. The investigation based on the information criterion indicated that the optimal results are obtained by simulating the series with the MA process with four components. The MA model has been fitted to the measurement data, resulting

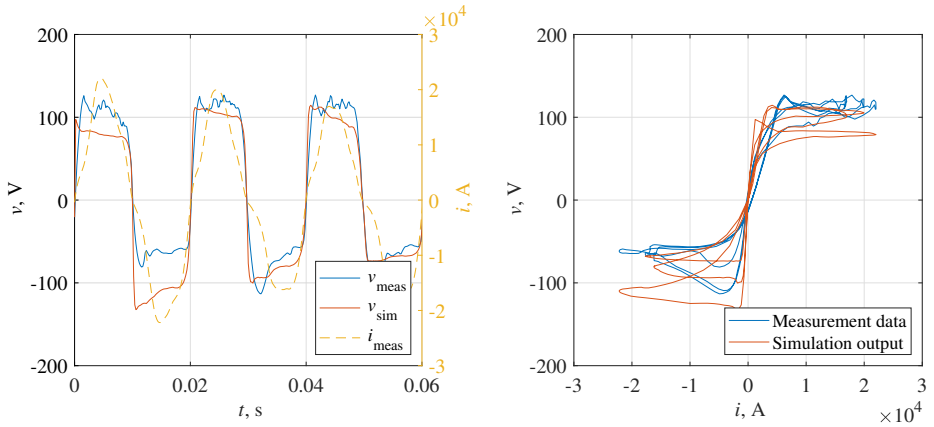

Fig. 3.14: Short-term current and voltage waveforms and characteristic of EAF single phase arc measured during the melting stage compared to the simulation output for the small industrial EAF.

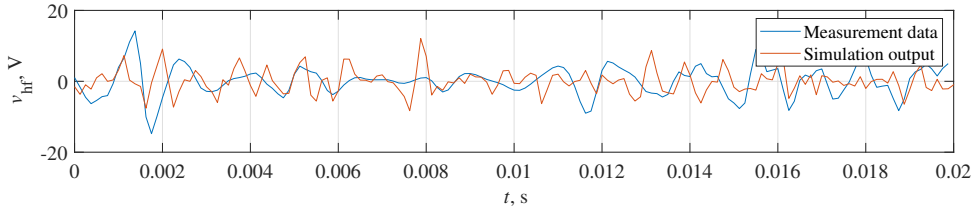

Fig. 3.15: High frequency component of small industrial EAF voltage waveform.

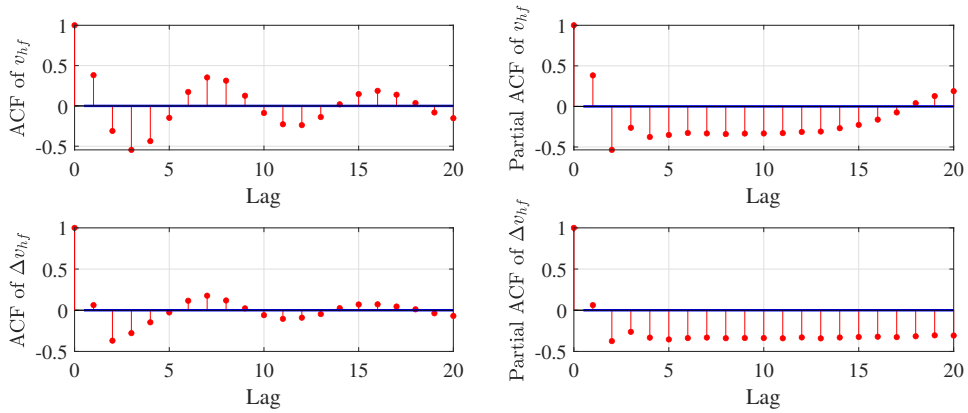

Fig. 3.16: Autocorrelation and partial autocorrelation function of the high frequency voltage component for small industrial EAF.

in the estimation of the following coefficients: $MA_1 = -0.395$, $MA_2 = -0.335$, $MA_3 = -0.507$ and $MA_4 = 0.248$. A signal generated with this MA model has been added to Fig. 3.15 with measurement data.

An example of the overall output waveform of the model and the characteristic V-I has been presented in Fig. 3.17. As shown, it reflects stochastic variations in the EAF characteristic in a wide spectrum of frequencies.

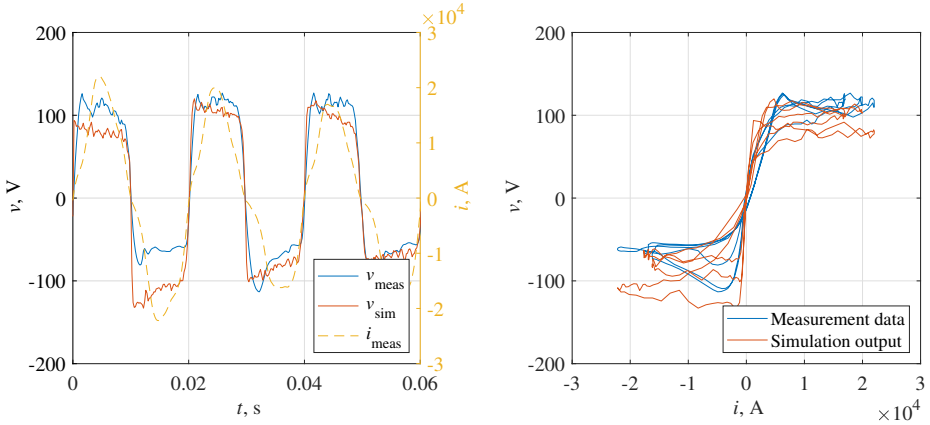

Fig. 3.17: Short-term current and voltage waveforms and characteristic of EAF single phase arc measured during the melting stage compared to the overall simulation output (with both low and high frequency components) for the small industrial EAF.

3.2.3 Analysis of K_1, K_2 and K_3 for the laboratory EAF

Another dataset which has been used to verify the RDE model has been obtained from the laboratory station. Due to strong asymmetry between the positive and negative parts of the waveforms, this dataset has been divided into half-period long frames based on the detected zero crossings. This type of division has been marked as Version C in Fig. 3.2.

The realizations of the processes K_j for this case have been presented in Fig. 3.18. In comparison with the realizations obtained from the large industrial furnace, the distributions and range significantly differ, although they are more similar to those from the small industrial one. The stochastic behavior of the series is again retained. Similarly to the previous section, the autocorrelation and 3D histograms of the realizations and its increments have been calculated and showed in Fig, 3.19 and Fig. 3.20. In this case a significant negative autocorrelation occurred in K_1. Histograms suggest that these processes again vary around a certain level, without any long-term drift in either a positive or negative direction. A histogram of K_3 has been zoomed into a range where the most significant differences between the bars are the most visible. Individual instances of values reaching above the histogram axis in Fig. 3.18 have been omitted.

In addition to the graphical representation of the realizations and some of their statistical properties, an investigation has been conducted to determine whether this approach improves the accuracy of the model for the laboratory EAF. Similarly to the large industrial and the small industrial EAFs, Table 3.3 presents the improvement rate in terms of RMSE error between the constant k_j (optimal for the dataset) and stochastic K_j. As shown, the improvement reaches approximately 70%. This is the best result among all the tested datasets and is strongly related to the asymmetry observed in the measurement data. Constant values of k_j are not only not capable of an accurate representation of the general shape of the furnace characteristic but cannot also include this asymmetry in the simulation.

Additionally, a model similar to the one concerning the large industrial furnace has been developed to compare the overall modeling approach. The values of k_j

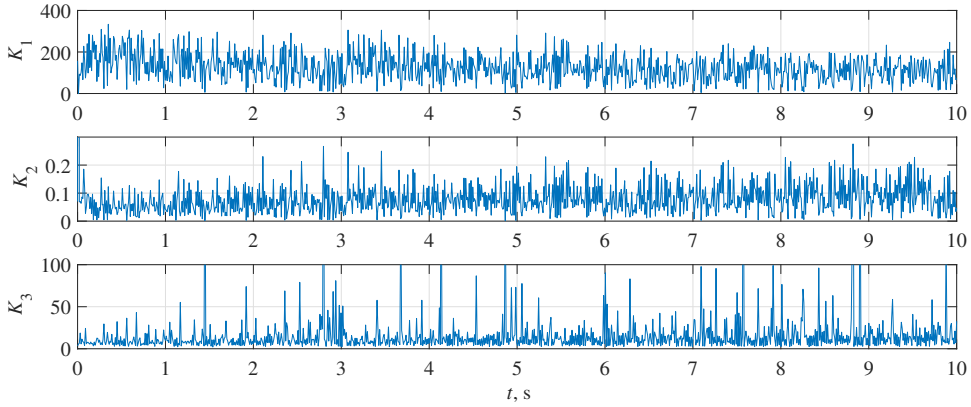

Fig. 3.18: Realizations of K_j stochastic processes estimated from laboratory EAF measurement data.

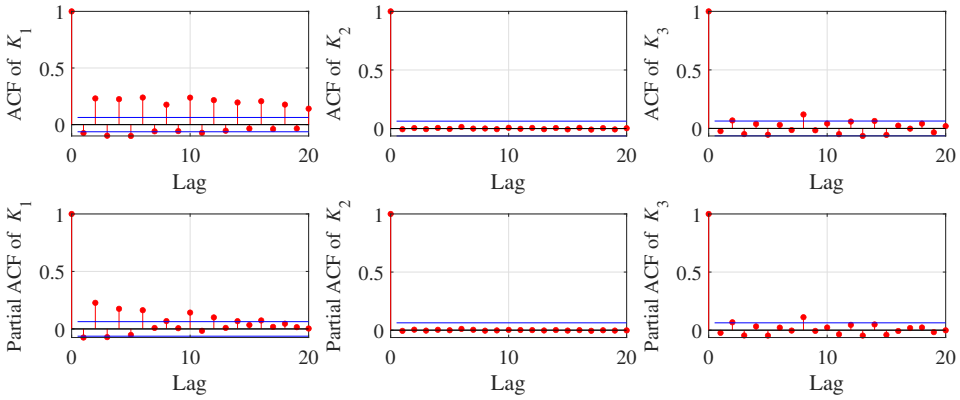

Fig. 3.19: Autocorrelation and partial autocorrelation function of realizations of K_j stochastic processes obtained from laboratory EAF measurement data.

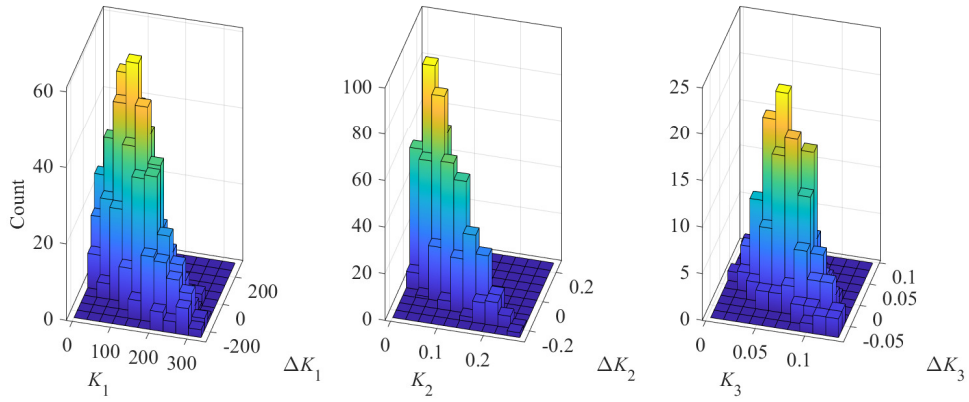

Fig. 3.20: Three dimensional histogram of raw values and their increments of realizations of K_j stochastic processes obtained from laboratory EAF measurement data.

in this simulation have been generated randomly for each frame from their actual distributions shown in Fig. 3.20. The applied method was an inverse CDF method, which allowed the draw of random variables from the empirically obtained distribu-

Table 3.3: Comparison of approaches with constant and variable k_j values for laboratory EAF.

	Constant coefficients	Stochastic processes	Relative change
Fitted values	$k_1 = 88.49$ $k_2 = 0.06$ $k_3 = 12.30$	k_j variable	-
RMSE	12.3	3.9	-68%

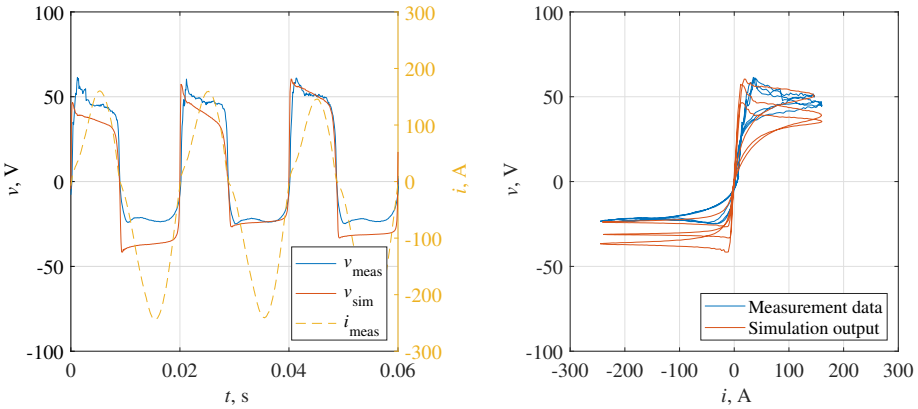

Fig. 3.21: Short-term current and voltage waveforms and characteristic of EAF single phase arc measured during the melting stage compared to the simulation output for the laboratory EAF.

tion. The exemplary output voltage realization has been presented in Fig. 3.21. As depicted, the model exhibits behavior similar to that of the measurement data.

For the laboratory EAF, the high frequency component has been analyzed separately. The application of the high-pass filter to the voltage measurement allow the obtaining of a signal presented in Fig. 3.22. As shown, the waveform seems stochastic. The autocorrelation and partial autocorrelation function analysis of the signal and its increment have been presented in Fig. 3.23. The investigation based on the information criterion indicated that the optimal results are obtained by simulating the series with the MA process with three components. The MA model has been fitted to the measurement data, resulting in the estimation of the following coefficients: $MA_1 = 0.907$, $MA_2 = 0.526$ and $MA_3 = 0.216$. A signal generated with this MA model has been added to Fig. 3.22 for comparison with measurement data.

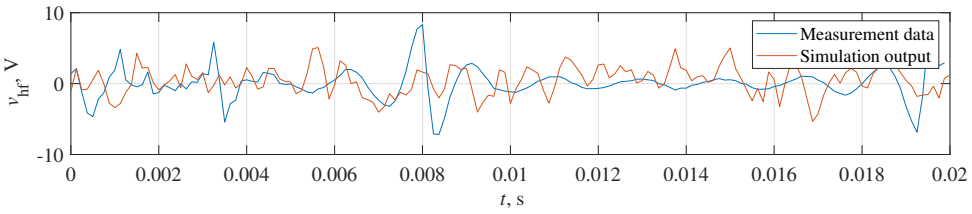

Fig. 3.22: High frequency component of the laboratory EAF voltage waveform.

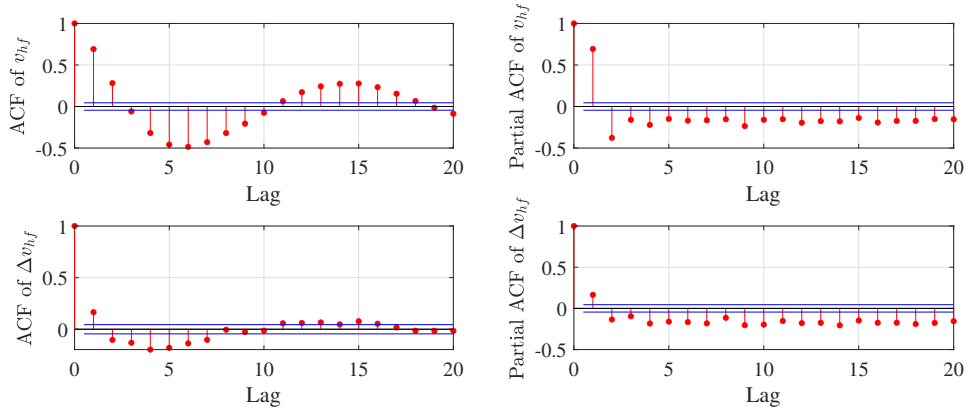

Fig. 3.23: Autocorrelation and partial autocorrelation function of the high frequency voltage component for the laboratory EAF.

An example of the overall model output waveform and the V-I characteristic obtained with a complete RDE model has been presented in Fig. 3.24. The asymmetry visible in those data limits the accuracy of representation of the high frequency component in the smoother, negative half of the signal period. However, the reflection of this component in the positive half is much better.

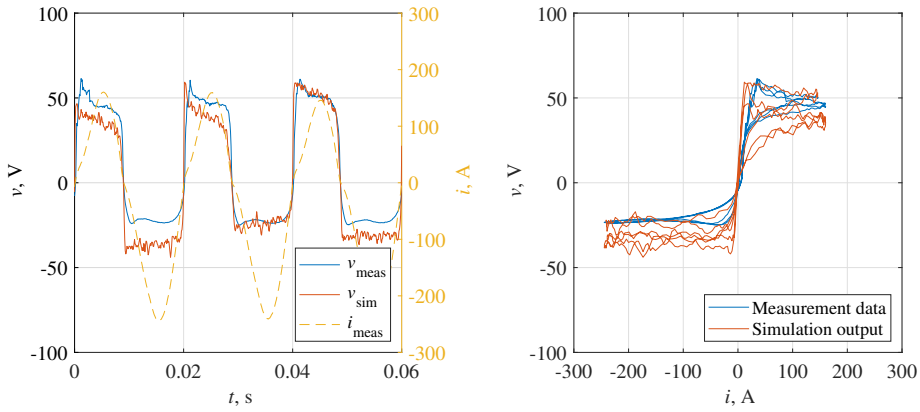

Fig. 3.24: Short-term current and voltage waveforms and characteristic of the EAF single phase arc measured during the melting stage compared to the overall simulation output (with both low and high frequency component) for the laboratory EAF.

3.2.4 Analysis of $\hat{K}_1$ and $\hat{K}_2$ for the large industrial EAF

The results presented in the previous section are related to the RDE model with three stochastic coefficients. This subsection is devoted to an extended analysis of the large industrial EAF with a model containing two stochastic processes that are identified in detail using more complex statistical analysis. After appropriate division of the realizations of the stochastic processes K_1, K_2, and K_3 by K_1, according to equation (3.5), the $\hat{K}_1$ and $\hat{K}_2$ time sequences have been obtained and presented in Fig. 3.25.

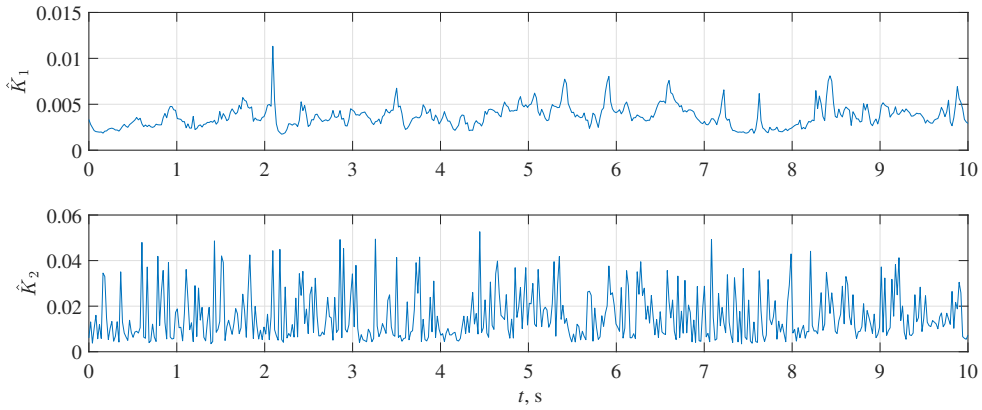

Fig. 3.25: Realizations of $\hat{K}_1$ and $\hat{K}_2$ stochastic processes estimated from large industrial EAF measurement data.

Table 3.4: Parameters of the ARIMA process representing $\hat{K}_1(l)$ for large industrial EAF.

ARIMA(1,1,2) coefficients	AR_1	MA_1	MA_2
	0.7627	0.8135	0.1556
standard error	0.0642	0.0738	0.0546

Analysis of $\hat{K}_1$ process

Firstly, a detailed investigation of the realization of $\hat{K}_1$ has been carried out. The graphic presentation of the distribution of values in Fig. 3.26 indicated that the distribution is not Gaussian. To perform further analysis, a Box-Cox transformation has been applied [53]. Then the autocorrelation and partial autocorrelation functions of both transformed data and its increments $\Delta\hat{K}_1[l] = \hat{K}_1[l] - \hat{K}_1[l-1]$ have been calculated [51]. The results have been presented in Fig. 3.27.

These results suggest that $\hat{K}_1(l)$ can be an autoregressive integrated moving average (ARIMA) process [51]. This process consists of terms related to regression based on previous samples (AR), a derivative of time series (I), and a linear combination of previous values (MA). ARIMA models are a class of models widely used in statistical analysis of time series for better understanding and prediction of some phenomena developing over time. To develop a standalone large industrial EAF model, the ARIMA process coefficients have been fitted to the measurement data. This was obtained by minimizing the information criterion. The optimization process resulted in the fitting of the ARIMA(1,1,2) model, which is characterized by a single autoregressive term, a differentiation degree of one, and two moving average terms. The values of the fitted parameters along with their standard errors have been combined in Table 3.4.

The residuals obtained under the assumption that $\hat{K}_1$ can be represented with the ARIMA (1,1,2) process have then been analyzed. Their distribution was non-normal, which was proven by a Shapiro-Wilk test (statistical significance: $p-$value$= 1.404 \cdot 10^{-10}$). Furthermore, analysis of the autocorrelation of the residuals indicated that they are not correlated. This hypothesis was also supported by the Ljung-Box test ($Q = 3.0403$, $df = 7$, statistical significance: $p-$value $= 0.8812$). The histogram

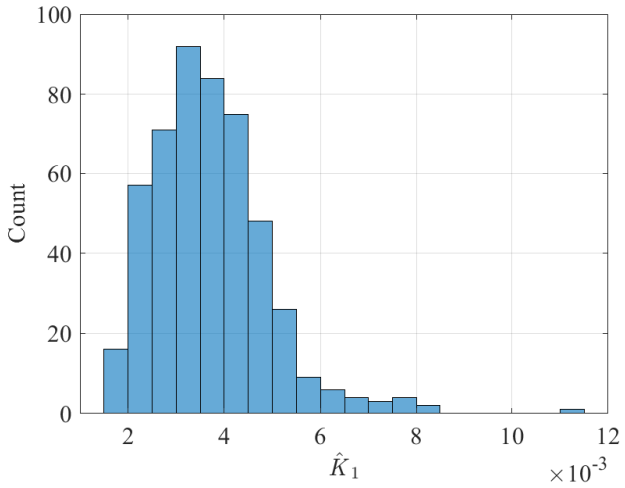

Fig. 3.26: Distribution of the values of $\hat{K}_1(l)$ for the large industrial EAF.

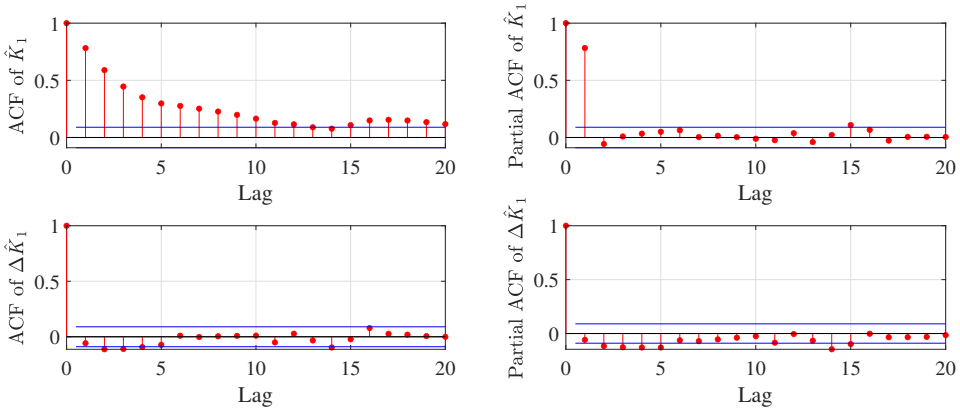

Fig. 3.27: Autocorrelation and partial autocorrelation function of $\hat{K}_1(l)$ and $\Delta\hat{K}_1(l)$ for the large industrial EAF.

itself suggests a symmetric distribution with positive excess kurtosis. A fitting of three potential distribution functions that could represent the residuals has been proposed, i.e. Laplace, hyperbolic secant, and logistic distribution. Each distribution has been fitted to the residual data and tested with the Kolmogorov-Smirnov test with a parametric bootstrap method to reduce the bias of the test results. Numerical results have been collected in Table 3.5.

The results suggest that the hypothesis that the $\hat{K}_1$ residuals can be represented with a logistic distribution should be rejected. Of the two remaining options, the hyperbolic secant distribution was the best fit. In conclusion, $\hat{K}_1$ can be represented with the ARIMA(1,1,2) model, the residuals of which follow the hyperbolic secant distribution.

Analysis of $\hat{K}_2$ process

Next, $\hat{K}_2$ has been analyzed similarly. The autocorrelation and partial autocorrelation of $\hat{K}_2$ have been calculated and shown in Fig. 3.28. The results obtained suggest that the process is white noise, which was supported by the results of the

Ljung-Box test (statistical significance: $p-$value$= 0.7489$) and Turning point test of independence (statistical significance: $p-$value$= 0.6193$).

After concluding that the process can be white noise, the exact distribution of the values was investigated. The histogram has been presented in Fig. 3.29. As shown, it is a bimodal distribution. Data were shifted to ensure that all values were positive. Then, it has been analyzed whether the distribution can be described by a shifted mixed Weibull distribution or a shifted mixed Gamma distribution. Each proposed model has been fitted to the data, and its compatibility was checked again with the Kolmogorov-Smirnov test with parametric bootstrap method correction. The combined results have been presented in Table 3.6. The numerical results obtained indicate that the best-fit distribution of a white noise $\hat{K}_2(l)$ process is a mixed shifted Weibull distribution with two components.

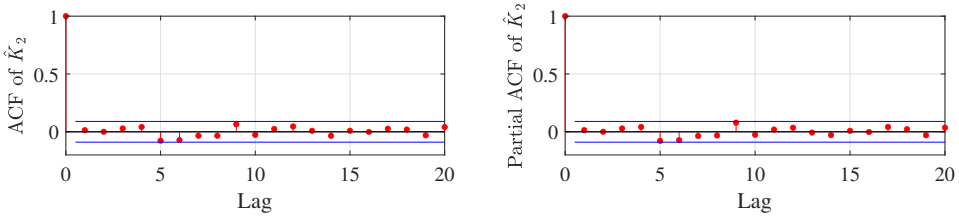

Fig. 3.28: Autocorrelation and partial autocorrelation function of $\hat{K}_2(l)$ for the large industrial EAF.

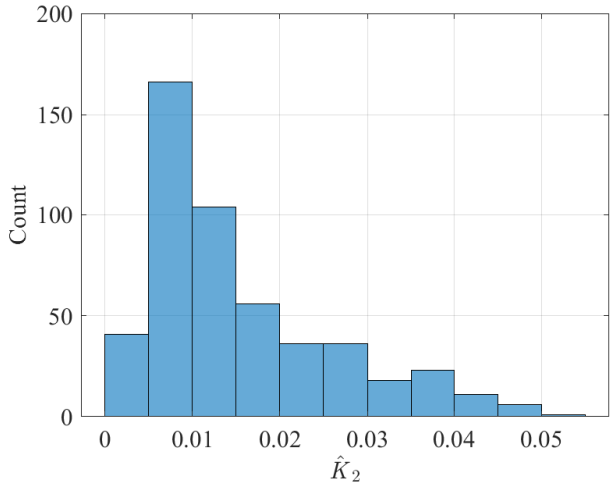

Fig. 3.29: Histogram of $\hat{K}_2(l)$ for the large industrial EAF.

Table 3.5: Parameters of residuals of the ARIMA process representing $\hat{K}_1(l)$ for the large industrial EAF.

Distribution	Density function	Fitted parameters	K-S p-value	Corrected p-value
Laplace	$f(x) = \frac{1}{2\sigma} e^{-\frac{\lvert x-\mu \rvert}{\sigma}}$	$\hat{\mu} = 0.011$ $\hat{\sigma} = 0.217$	0.795	0.445
Hyperbolic secant	$f(x) = \frac{1}{2\sigma} \operatorname{sech}\left(\frac{\pi(x-\mu)}{2\sigma}\right)$	$\hat{\mu} = 0.007$ $\hat{\sigma} = 0.292$	0.895	0.824
Logistic	$f(x) = \frac{1}{\beta} e^{\frac{x-\alpha}{\beta}} \left(1 + e^{\frac{x-\alpha}{\beta}}\right)^{-2}$	$\hat{\alpha} = 71.753$ $\hat{\beta} = 1578.395$	0.496	0.035

Table 3.6: Distribution parameters of $\hat{K}_2(l)$ for the large industrial EAF.

Distribution	Density function	Fitted parameters	K-S p-value	Corrected p-value
Mixed Weibull	$f(x) = \pi_1 \cdot f_{\text{Weib}}(x; k_1, \lambda_1) + \pi_2 \cdot f_{\text{Weib}}(x; k_2, \lambda_2)$ $f_{\text{Weib}}(x; k, \lambda) = \begin{cases} \frac{k}{\lambda}\left(\frac{x}{\lambda}\right)^{k-1} e^{-\left(\frac{x}{\lambda}\right)^k} & : x > 0 \\ 0 & : x \leq 0 \end{cases}$	$\hat{\pi}_1 = 0.765$ $\hat{\pi}_2 = 0.235$ $\hat{k}_1 = 1.278$ $\hat{k}_2 = 3.209$ $\hat{\lambda}_1 = 0.008$ $\hat{\lambda}_2 = 0.030$	0.982	0.631
Mixed Gamma	$f(x) = \pi_1 \cdot f_{\text{Gam}}(x; \alpha_1, \beta_1) + \pi_2 \cdot f_{\text{Gam}}(x; \alpha_2, \beta_2)$ $f_{\text{Gam}}(x; \alpha, \beta) = \begin{cases} \frac{x^{\alpha-1} e^{-\frac{x}{\beta}}}{\beta^\alpha \Gamma(\alpha)} & : x > 0 \\ 0 & : x \leq 0 \end{cases}$	$\hat{\pi}_1 = 0.936$ $\hat{\pi}_2 = 0.064$ $\hat{\alpha}_1 = 1.231$ $\hat{\alpha}_2 = 60.002$ $\hat{\beta}_1 = 118.296$ $\hat{\beta}_2 = 1744.354$	0.658	0.236

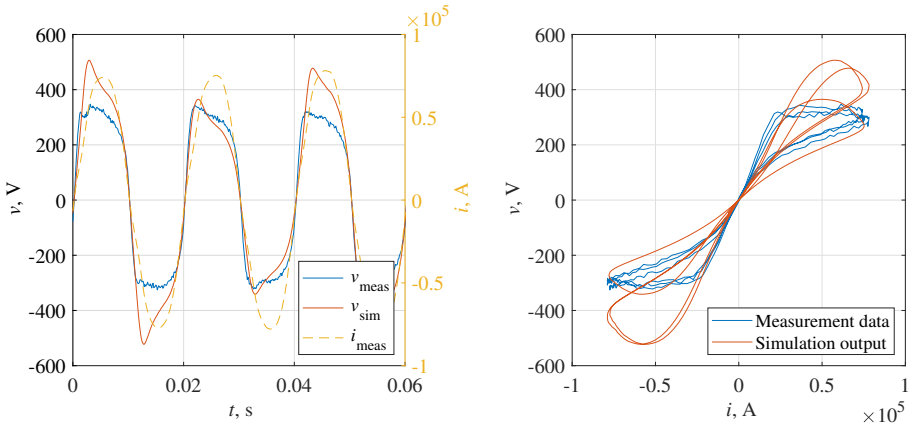

Fig. 3.30: Short-term current and voltage waveforms and characteristic of the EAF single-phase arc measured during the melting stage compared to the extended model output for large industrial EAF.

The results described above can be considered as details of a standalone model of an EAF capable of reflecting low frequency stochastic phenomena related to variations of a general shape of the V-I characteristic. For demonstration of the model operation, the output of an exemplary clipping of the input current waveform has been calculated. The output voltage waveform has been computed using the model with stochastic processes K_j obtained through independent processes of $\hat{K}_1$ and $\hat{K}_2$. The discrete-time processes have changed the values of the k_j coefficients in the power balance model for each period. The output voltage and characteristic have been presented in Fig. 3.30. As shown, the low frequency random variations observable in the real EAF measurement data are reflected by the model accurately. Individual periods vary and tend to have a larger difference to the measurement data. However, it needs to be stressed that this is only an exemplary realization, among which such an effect can occur.

Chapter 4

Chaotic EAF model

In certain conditions, random properties of a given phenomenon can be mistakenly interpreted as purely stochastic in nature, while they can be the result of deterministic chaos. In the case of EAFs, it is generally considered stochastic, although some researchers have proven that it can exhibit chaotic behavior, as shown in [54]. In fact, an EAF is a complex dynamical system in which the arc is influenced by multiple factors, which may lead to temporary chaotic behavior. This in turn is similar to the complex dynamical system such as weather, which was a subject to initial chaos research conducted by E. Lorenz in the 1960s [55]. The chaotic behavior can be included in the EAF model to mimic the stochastic variations, as has been done in e.g., [24], [18] or [29]. This idea is based on the model introduced in the previous Chapter. Its details have been introduced in the author's previous publication - [40] and are presented in the next Section. One of the advantages of this approach is that although the chaotic system approximates the stochastic behavior, it is still deterministic. Consequently, one could study many different paths of developments in a dynamical system describing the arc, while maintaining the exact same nature and order of random-like events. Those paths could be related, e.g., to the application of different control algorithms or topology of power quality improvement systems. A deterministic background would allow for an objective comparison of the effects that those components or strategies have on a power system with an EAF.

4.1 Selected chaotic systems

The chaotic EAF model approach is strongly based on the RDE model presented in the previous Chapter. The main assumption regarding the changes in the EAF V-I characteristic remains the same - the variability of the k_j coefficients is responsible for their reflection. However, in the case of a chaotic model, the coefficients are not reflected with stochastic processes, but time sequences derived from chaotic systems. It is essential that the applied system remains in a chaotic state so that a single chosen variable time sequence can approximate random changes of a single coefficient k_j. In this way, a set of three chaotic systems could represent changes of the three coefficients k_j. There are many different chaotic systems described in the literature, which vary in terms of the severity of the chaotic behavior, the complexity of the chaotic attractors, and the timescale at which those behaviors can be observed. To ensure that the final results are accurate, the most universal and widely used have been chosen: a system based on the Chua circuit, the Lorenz

system, the Rössler system and another chaotic system introduced in [56]. The latter does not have a name, so it will be referred to as a four-wing chaotic attractor system based on the shape of its attractor.

As suggested in the previous paragraph, each system is characterized by its own range of values and the speed of changes. The first step leading to a proper application of a chaotic system is to modify the raw chaotic system time sequences using the median and standard deviation of each k_j coefficient calculated from the EAF measurement data. The sequence obtained from the chaotic system is modified so that the median and kurtosis of its distribution fits the chosen k_j coefficient distribution. To fit a chaotic system to modeling EAF, its parameters must be further optimized. The optimization has to be conducted in a way ensuring chaotic behavior, because otherwise the obtained time sequences would not be suitable for approximation of stochastic changes. To fit the system into its assumed role, a two-objective optimization has been performed for the combination of each system juxtaposed with each of the coefficients k_j. After the optimization process, the best-fit pairs have been selected.

The optimization process takes into account two decision variables. The first is one of the system's parameters which value is bounded to ensure a chaotic state, but which changes could result in better fitting of an attractor shape. This variable is denoted as ξ. The second is a sampling frequency f_s, which cannot be too high to obtain stochastic-like time sequences. Those two variables are subject to optimization applying two goal functions. One is related to the distribution of the values obtained from a chaotic system, while the second is related to their autocorrelation. The goal is to minimize the Cramér-von Mises distance between histograms and autocorrelation samples calculated based on the sequences k_j obtained from the measurement data and those obtained from a chaotic system [57]. Formally, the goal functions can be written as

$$\begin{aligned} f_1(\cdot) &= \sum_{p=1}^{N} (h_p^{meas} - h_p^{chaotic})^2, \\ f_2(\cdot) &= \sum_{p=1}^{M} (ACF_p^{meas} - ACF_p^{chaotic})^2, \end{aligned} \tag{4.1}$$

where:

h_p – p-th histogram bar of measurement or modified chaotic system data distribution,
N – number of histogram bars,
ACF_p – autocorrelation value for p-th lag,
M – number of lags for autocorrelation calculation.

Considering the decision variables, the optimization problem takes the following form:

$$\begin{aligned} &\min_{\xi, f_s} f_1(\xi, f_s), \\ &\min_{\xi, f_s} f_2(\xi, f_s), \end{aligned} \tag{4.2}$$

where $\xi \in \{C_2, L_2, R_3, F_3\}$ represents a single optimized parameter chosen individually from the coefficients in the equation of the chaotic system. The systems related

to the above variables are the Chua system, the Lorenz system, the Rössler system, and the four-wing attractor system, respectively. The exact equations have been presented in the following subsections.

Once the two-objective optimization is complete, a final solution is selected from a Pareto front as the closest to the ideal solution, which would be given by $f_1(\cdot) = 0$ and $f_2(\cdot) = 0$ [58]. More precisely, for each solution that belongs to the front, both values of the target function are normalized, and then an Euclidean distance is calculated with respect to the ideal point $(0, 0)$. The best solution is characterized by the smallest distance calculated.

4.1.1 Chua circuit

A Chua circuit was first introduced in [59]. It is a physical, autonomous electrical circuit that exhibits chaotic behavior. It has been studied through the years by many researchers because of its potential for many engineering applications. The system is described with a set of differential equations:

$$\begin{cases} \dot{x} = C_1(y - x - g(x)), \\ \dot{y} = x - y + z, \\ \dot{z} = -C_2 y, \\ g(x) = C_{d2}x + \dfrac{C_{d1} - C_{d2}}{2}(|x + 1| - |x - 1|), \end{cases} \tag{4.3}$$

where:

C_1, C_2 – coefficients related to resistance and capacitance of circuit elements,
C_{d1}, C_{d2} – parameters related to the slopes of the characteristic of the Chua diode.

Typical chaotic orbits examined in the case of the Chua system are obtained for $C_1 = 15.6$, $C_{d1} = -\frac{8}{7}$, $C_{d2} = -\frac{5}{7}$ and with variable C_2. In this case, the value C_2 was fitted to the data related to EAFs. To keep the signals chaotic, this coefficient can change in the following range $22.8 \leq C_2 \leq 33.6$. The variable y was chosen to represent the stochastic processes K_j. An exemplary chaotic attractor related to the Chua circuit has been presented in Fig. 4.1.

4.1.2 Lorenz system

The Lorenz chaotic system was introduced in [55] as a model related to the unpredictability of the weather. The set of equations can be formulated as follows:

$$\begin{cases} \dot{x} = L_1(y - x), \\ \dot{y} = x(L_2 - z) - y, \\ \dot{z} = xy - L_3 z, \end{cases} \tag{4.4}$$

where:

L_1 – coefficient related to the Prandtl number,
L_2 – coefficient related to the Rayleigh number,
L_3 – a geometric factor.

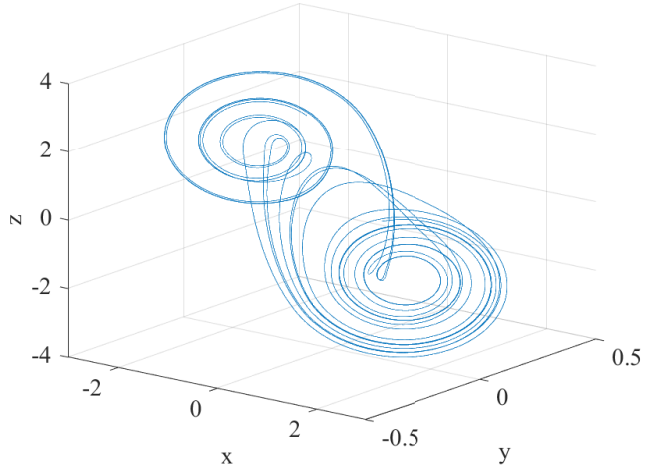

Fig. 4.1: Example of a Chua circuit chaotic attractor for the following parameters: $C_1 = 15.6$, $C_2 = 27$ $C_{d1} = -\frac{8}{7}$, $C_{d2} = -\frac{5}{7}$.

The dynamics of the Lorenz system is most often investigated for parameters $L_1 = 10$, $L_3 = \frac{8}{3}$, and for variable L_2. The latter was fitted to the data, but in order to ensure chaotic behavior, it had to be greater than:

$$L_2' = \frac{L_1(L_1 + L_3 + 3)}{L_1 - L_3 - 1} = 24.74. \tag{4.5}$$

The variable x was chosen to represent the stochastic processes K_j. An example of a Lorenz attractor has been presented in Fig. 4.2.

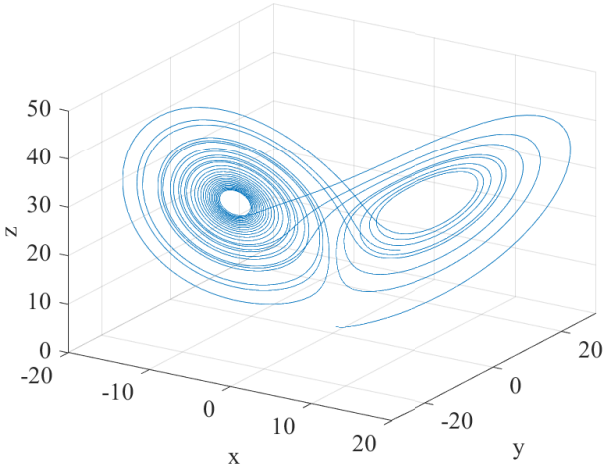

Fig. 4.2: Example of a Lorenz chaotic attractor for the following parameters: $L_1 = 10$, $L_2 = 28$, $L_3 = \frac{8}{3}$.

4.1.3 Rössler system

The Rössler system, intended to behave similarly to the Lorenz system, was introduced in [60]. It is described with the following equations:

$$\begin{cases} \dot{x} = -(y+z), \\ \dot{y} = x + R_1 y, \\ \dot{z} = R_2 + z(x - R_3), \end{cases} \tag{4.6}$$

where:

R_1, R_2, R_3 – real-valued system coefficients.

The Rössler system was investigated, among others, for parameters $R_1 = R_2 = 0.2$ and variable R_3. We have assumed that R_3 was fitted to the limits $4.2 \leq R_3 \leq 8$. The variable y was chosen to represent the stochastic processes K_j. An example of a Rössler chaotic attractor has been presented in Fig. 4.3.

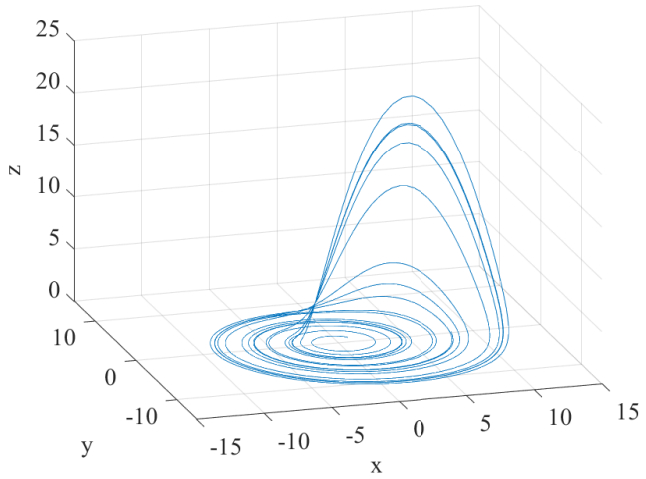

Fig. 4.3: Example of a Rössler chaotic attractor for the following parameters: $R_1 = R_2 = 0.2$ and $R_3 = 5.7$.

4.1.4 Four-wing chaotic attractor system

Based on theoretical and practical experiences related to the Chua, Lorenz, and Rössler systems the authors of [56] introduced a new chaotic system. It exhibits a four-wing chaotic attractor with a complicated topological structure over a wide range of parameters. The system is given by:

$$\begin{cases} \dot{x} = F_1(y - x) + F_5 yz, \\ \dot{y} = F_3 x + F_4 y - xz, \\ \dot{z} = -F_2 z + xy, \end{cases} \tag{4.7}$$

where:

F_1, F_2, F_4, F_5 – positive real-valued system coefficients,
F_3 – real-valued coefficient.

The system was thoroughly investigated and described in the cited work [56]. The authors deal primarily with the simulation results obtained with $F_1 = 14$, $F_2 = 43$, $F_4 = 16$, $F_5 = 4$, and the variable F_3. A wide range of chaotic behavior was observed

for $-2.3 \leq F_3 \leq 3$. Similarly, in the case of EAF modeling, the coefficients F_1, F_2, F_4, and F_5 were fixed as mentioned and F_3 was fitted to the data while maintaining the proposed range. The variable x was chosen to represent the stochastic processes K_j. An example of a four-wing chaotic attractor has been presented in Fig. 4.4.

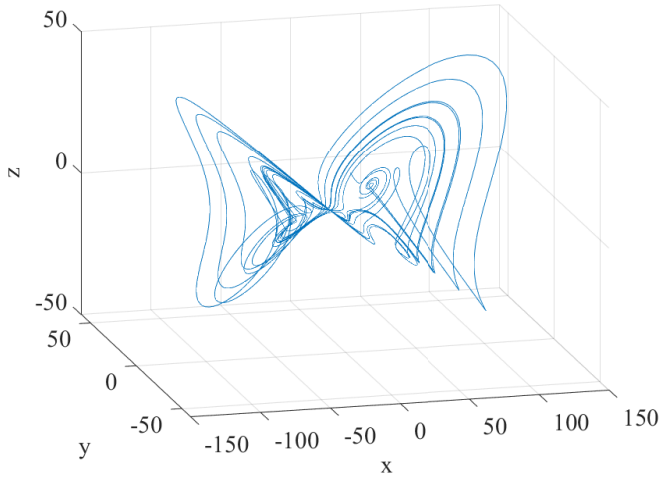

Fig. 4.4: Example of a four-wing chaotic attractor for the following parameters: $F_1 = 14$, $F_2 = 43$, $F_3 = -1$, $F_4 = 16$, $F_5 = 4$.

4.2 Simulation results and analysis

This section consists of three subsections devoted to the numerical results of the development of the chaotic model based on the EAF measurement data. Each subsection includes results obtained for EAFs of different sizes: large industrial, small industrial and laboratory furnace, respectively.

4.2.1 Large industrial EAF

Each of the systems proposed in the previous Section, i.e., the Chua, Lorenz, Rössler, and four-wing attractor systems, has been fitted using the optimization procedure described with equation (4.2) to each of the realizations of stochastic processes K_j. For each combination of the chaotic system and the coefficient K_j, the error, which is an Euclidean distance of the normalized coordinates represented with the goal function values to the ideal point $(0, 0)$ has been calculated. Its value has been denoted with symbol d. For every solution considered, the fitted value of the chaotic system coefficient $\xi \in \{C_2, L_2, R_3, F_3\}$ and the appropriate sampling frequency f_s have been provided. The exact results have been presented in Table 4.1. As shown, for the processes K_1 and K_3, it was the Lorenz system that after optimization was characterized by the lowest error. For K_2, the best fitted system was the four-wing attractor system. The best solutions for each process K_j are indicated in bold font.

To provide more detailed information on the results obtained, an additional graphical representation of the quantities related to the goal functions has been presented. The output sequences obtained from the chaotic systems have been presented in Fig. 4.5. For each of the best solutions, that is, the Lorenz system for

Table 4.1: Results of multi-objective optimization of chaotic systems for the large industrial EAF.

		Chua	**Lorenz**	**Rössler**	**Four-wing**
	ξ	24.73	**41.00**	7.34	-0.28
K_1	f_s, Hz	0.18	**2.05**	0.43	3.00
	d	0.13	**0.08**	1.35	1.00
	ξ	24.15	27.13	7.86	**1.13**
K_2	f_s, Hz	0.30	3.40	0.45	**8.47**
	d	0.56	0.54	1.41	**0.47**
	ξ	24.21	**32.03**	7.85	-1.00
K_3	f_s, Hz	0.20	**2.48**	0.51	3.57
	d	0.62	**0.43**	1.41	0.59

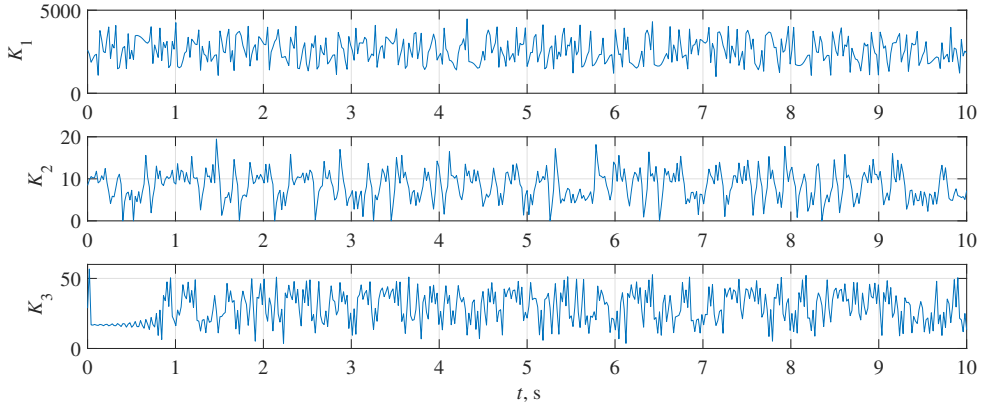

Fig. 4.5: Time sequences of the realizations of K_j obtained with an optimized chaotic systems for the large industrial EAF.

K_1 and K_3, and the four-wing attractor system for K_2, Fig. 4.6 shows the histograms and autocorrelation plots calculated based on the original realizations K_j and those simulated with the appropriate chaotic system. As shown, the optimized chaotic system for all cases is characterized by features very similar to those of the original measurement-based data in terms of distributions and autocorrelation.

Based on the above results, a model similar to the one presented in Chapter 3 has been proposed, but with a fundamental difference: in the chaotic model, the discrete-time values of K_j are generated with autonomous, optimized chaotic system differential equations. Each of the K_j is described with a separate chaotic system, the best fitting according to the data presented in Table 4.1. This means that in the case of a large industrial furnace, K_1 and K_3 have been represented with two separate Lorenz systems, and K_2 with a four-wing attractor system. Fig. 4.7 presents an example realization of the output voltage waveform and the V-I characteristic obtained from such a combined model, compared to the measurement data. As depicted, the model exhibits very similar features related to changes in the general shape of the EAF V-I characteristic.

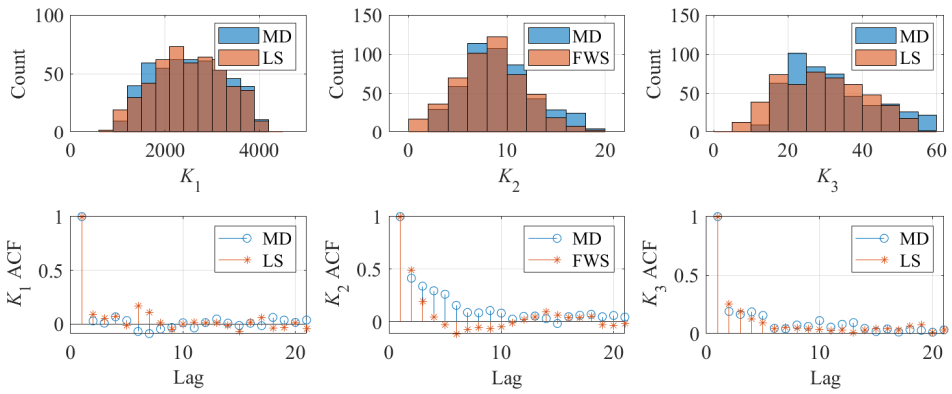

Fig. 4.6: Histograms and autocorrelation functions of the realizations of K_j calculated based on measurement data (MD) and fitted using the Lorenz system (LS) or the four-wing attractor system (FWS) for the large industrial EAF.

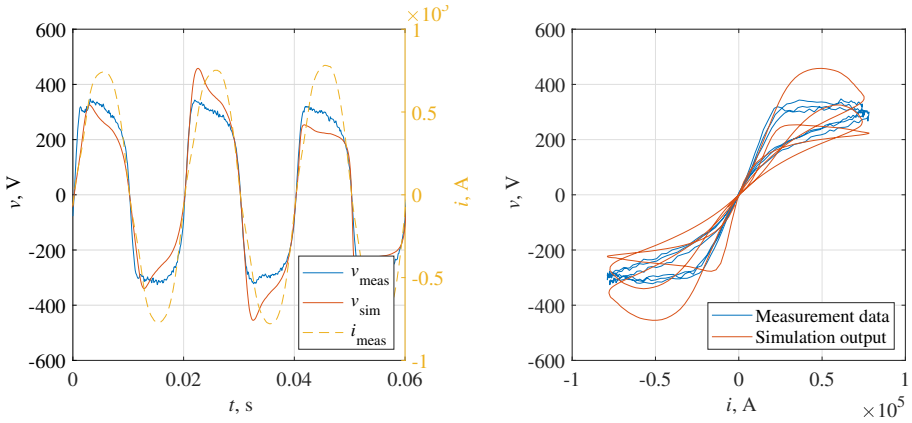

Fig. 4.7: Comparison of the measurement voltage waveform and the V-I characteristic with a realization generated by a chaotic EAF model for the large industrial EAF.

4.2.2 Small industrial EAF

A similar optimization procedure has been carried out based on the measurement data obtained from the small industrial EAF. The numerical results have been presented in Table 4.2. As highlighted, in this case the best chaotic systems were the four-wing attractor system for representation of K_1 and K_2, and the Rössler system for K_3. The realizations of the time series K_j have been presented in Fig. 4.8. Reflection of K_2 with a chaotic system has been more complicated due to the range of data, which causes the chaotic system to generate values close to zero, which can hinder the simulation process. An additional step of outliers cleaning is enough to ensure that numerical results remain good and the stochastic-like properties of the time series are retained. A graphic representation of both optimization criteria has been placed in Fig. 4.9. As shown for this dataset, the optimization process leads to obtaining distributions and autocorrelation values close to those originating from the measurement data.

For the purpose of comparison of the overall output of the model, Fig. 4.10 presents the measurement voltage, current and exemplary realization of the output voltage taken from the combined chaotic model using best fitted systems for the small industrial EAF. In addition, the figure contains a comparison of the V-I characteristics. Certain periods tend to take a shape which is more square, although, as mentioned earlier, these are only the exemplary realizations. Thus, some periods may differ. However, the tendency of the model to produce such a shape is related to the range of values generated by the chaotic model, which in the case of K_2 is slightly lower than in the measurement data.

Table 4.2: Results of multi-objective optimization of chaotic systems for the small industrial EAF.

		Chua	**Lorenz**	**Rössler**	**Four-wing**
	ξ	24.08	31.02	7.85	**-1.76**
K_1	f_s, Hz	0.86	0.42	2.94	**0.44**
	d	0.76	1.09	1.36	**0.50**
	ξ	24.38	41.48	7.86	**-0.61**
K_2	f_s, Hz	1.47	0.54	2.15	**0.42**
	d	0.44	1.00	1.02	**0.12**
	ξ	27.64	37.20	**6.10**	0.08
K_3	f_s, Hz	0.73	0.31	**2.94**	0.44
	d	1.00	1.14	**0.61**	1.17

4.2.3 Laboratory EAF

The optimization procedure has been repeated for the measurement data obtained from the laboratory EAF. The numerical results are summarized in Table 4.3. As highlighted, in this case the best chaotic system for the representation of all coefficients was the four-wing attractor system. The realizations of the time series K_j have been presented in Fig. 4.11. In case of these data, an additional step

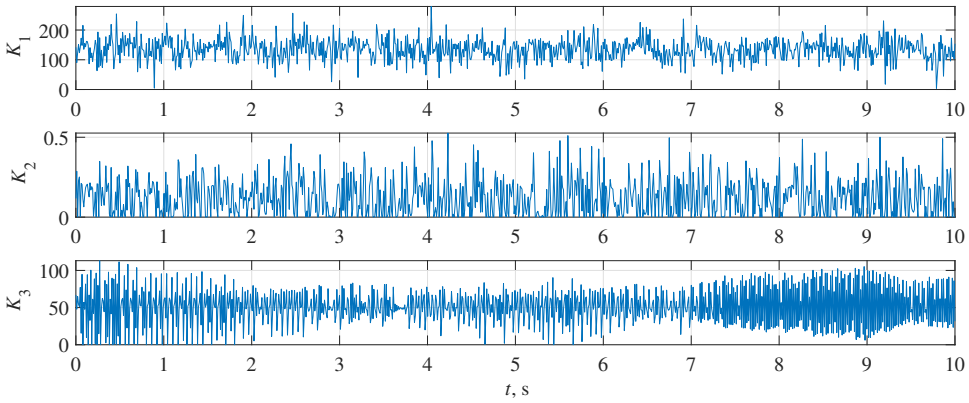

Fig. 4.8: Time sequences of the realizations of K_j obtained with the optimized chaotic systems for the small industrial EAF.

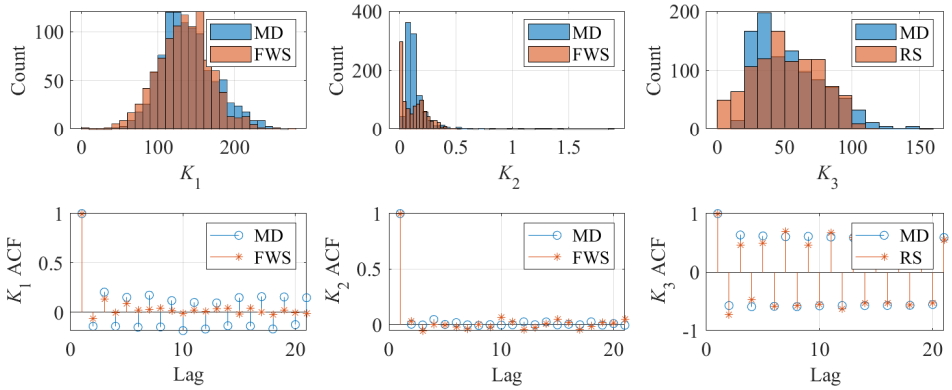

Fig. 4.9: Histograms and autocorrelation functions of realizations K_j calculated on the basis of measurement data (MD) and fitted using the Rossler system (RS) or the four-wing attractor system (FWS) for the small industrial EAF.

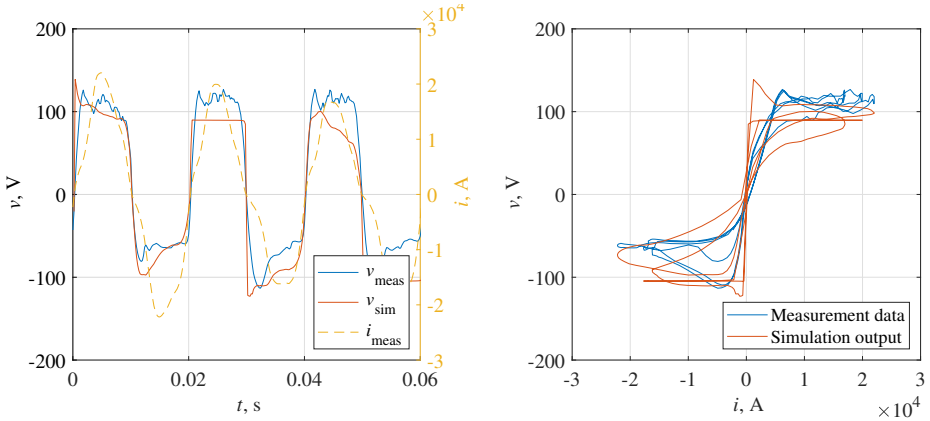

Fig. 4.10: Comparison of the measurement voltage waveform and V-I characteristic with a realization generated by a chaotic EAF model for the small industrial EAF.

of outliers cleaning has also been applied. The graphic representation of both optimization criteria has been placed in Fig. 4.12. As shown, for this dataset, the optimization process leads to the obtaining of distributions and autocorrelation values close to those originating from the measurement data. The results also suggest that the reflection of autocorrelation has been relatively harder than in the case of the other datasets, mainly because of the asymmetry between the period halves. The distribution of values was well represented, especially in the case of K_1 and K_2.

For the purpose of comparison of the overall output of the model, Fig. 4.13 presents the measurement voltage, current, and exemplary realization of the output voltage taken from the combined chaotic model using the best fitting chaotic systems for the laboratory EAF. In addition, the figure contains a comparison of the V-I characteristics. The overall effects of stochastic-like features resemble real observable phenomena.

Table 4.3: Results of multi-objective optimization of chaotic systems for the laboratory EAF.

		Chua	**Lorenz**	**Rössler**	**Four-wing**
	ξ	24.21	30.73	6.67	**-1.50**
K_1	f_s, Hz	1.94	0.40	2.75	**0.41**
	d	0.42	0.38	1.41	**0.23**
	ξ	24.41	37.56	7.86	**-0.39**
K_2	f_s, Hz	1.97	0.55	2.43	**0.33**
	d	0.52	0.53	1.41	**0.09**
	ξ	24.60	26.30	7.86	**-0.96**
K_3	f_s, Hz	0.58	0.23	2.13	**0.37**
	d	1.06	1.01	1.04	**0.22**

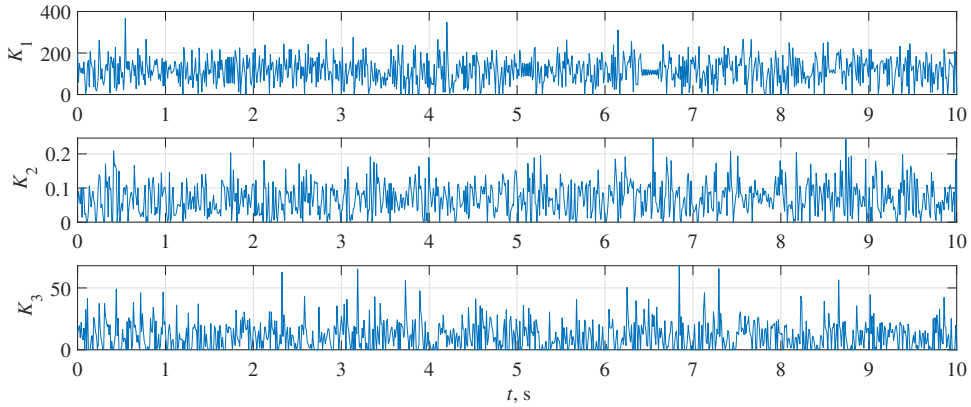

Fig. 4.11: Time sequences of the realizations of K_j obtained with the optimized chaotic systems for the laboratory EAF.

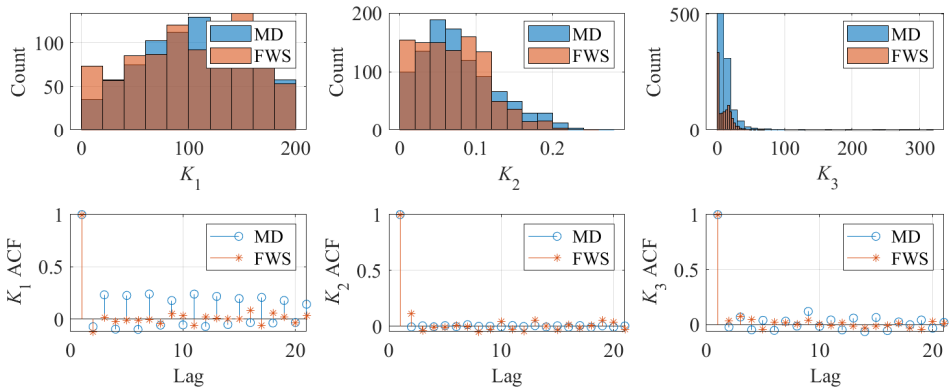

Fig. 4.12: Histograms and autocorrelation functions of the realizations of K_j calculated on the basis of the measurement data (MD) and fitted using the four-wing attractor system (FWS) for the laboratory EAF.

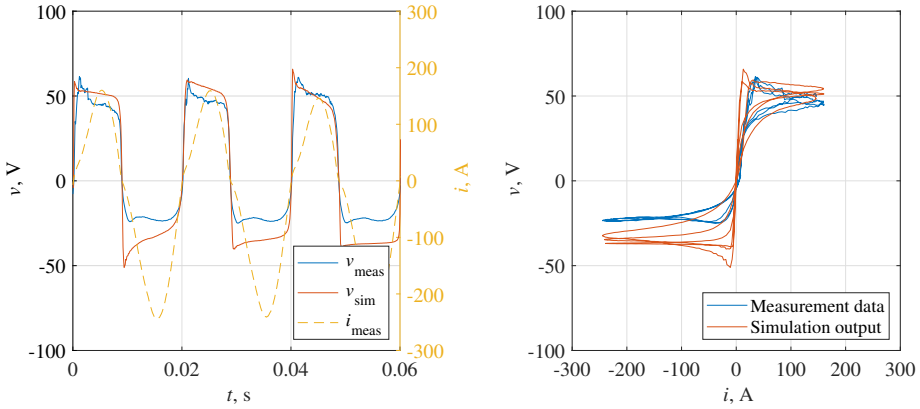

Fig. 4.13: Comparison of the measurement voltage waveform and V-I characteristic with a realization generated by a chaotic EAF model for the laboratory EAF.

Chapter 5

Artificial neural network EAF models

Some complex objects are very hard to model using any directly described mathematical expressions. In such cases, sometimes the only information regarding their behavior is limited to input and output data. To model such phenomena, it is very useful to apply methods belonging to the category of artificial intelligence. The development of a black-box model can be significantly simpler than trying to find a closed-form mathematical solution. Moreover, such models are characterized a high level of accuracy. In some other cases, developing a gray-box model is even more suitable. Especially when one has limited knowledge about a theoretical structure of a modeled phenomenon. Such a model combines a black-box concept with additional information regarding the structure to achieve good accuracy. The electric arc belongs to the group of phenomena which are relatively complex to model accurately. Therefore, it is justified to analyze the possibility of modeling EAFs with universal methods such as those based on artificial intelligence. Moreover, this approach has been applied for this purpose by other researchers, e.g., in [31], [27] or [32].

5.1 Selected ANNs

This Chapter introduces several models based on ANNs with different complexity. Three of the developed models have a fairly simple structure and belong to shallow ANNs, while two others are more complex, and they apply deep learning methods. The latter models are based on long short-term memory (LSTM) networks. A diagram presenting the approaches introduced in this Chapter has been presented in Fig. 5.1. Shallow ANNs include multilayer perceptron (MLP) and dual MLP models for the approximation of the V-I characteristic, as well as the modified nonlinear autoregressive exogenous (NARX) model, which replaces a dynamic block in the power balance equation model. The deep learning approach includes the representation of stochastic processes identified in Chapter 3 with LSTM neural networks. The proposed solutions have been the subject of previous publications [41], [39] and [42].

5.1.1 Shallow ANN

Multilayer perceptron model

The first shallow model developed is a very simple MLP model, which is considered a universal approximator. Its universality also comes with relatively low accuracy

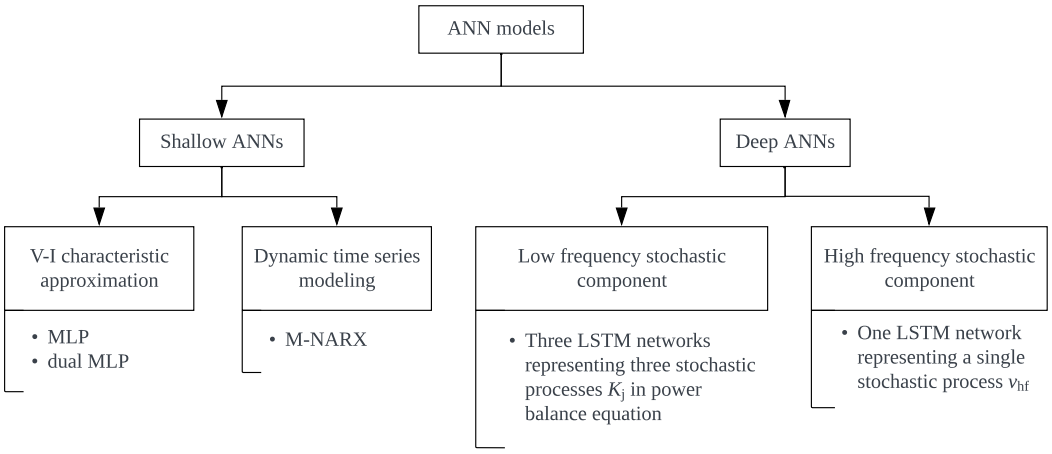

Fig. 5.1: Diagram presenting ANN based solutions for EAF modeling proposed in the dissertation.

in reflecting more complex objects. The MLP model has been developed to provide a basic reference to other models based on ANNs. The MLP consists of an input layer, a hidden layer containing a user-chosen number of units, and an output layer. The structure of a single neuron has been shown in Fig. 5.2. The transfer function f can be defined by the user, but among the most common are linear, logistic, or hyperbolic tangent functions. Such units are contained in hidden and output layers of the MLP model. A whole model structure including all important layers has been presented in Fig. 5.3.

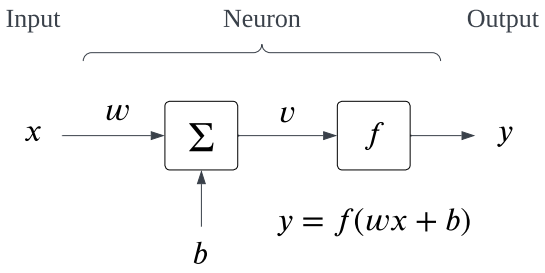

Fig. 5.2: Structure of a single neuron in an ANN model.

As shown in Fig. 5.3, the MLP applied in the EAF model is reduced to a simple structure of the single input single output (SISO) system. It has the role of a simple black-box object that is intended to directly reflect the EAF V-I characteristic. In this application, a current waveform is considered as the input while a voltage is considered as the output. The weight coefficients located inside the individual neural units are fitted during the learning procedure based on the measurement data. The data are first divided into training, validation, and testing sets, which are necessary to obtain the good effects of the learning procedure. The network adjusts its coefficients to reduce the overall error between its output and target data. Due to the simple structure of the MLP model, it is characterized by a tendency to average

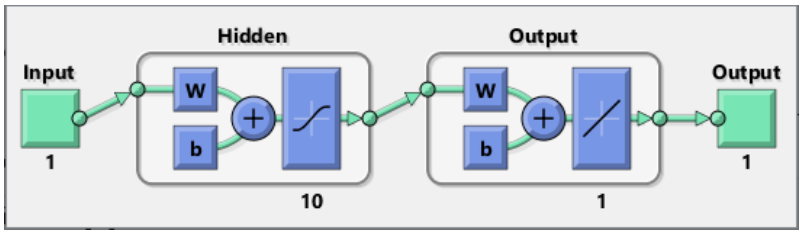

Fig. 5.3: Structure of the MLP model.

more complex input-output relationships but is perfectly capable of reflecting a certain class of nonlinear characteristics.

Dual multilayer perceptron (MLP) model

Due to limitations related to the application of a single MLP model, an extension has been proposed that allows for a better reflection of the EAF characteristic. As shown in Chapter 2, the V-I characteristic of the arc contains a hysteresis. An improvement in MLP response to such training data can be achieved by doubling its structure and dividing the characteristic into two categories, one for each network. Taking into account the MLP operation, the best division would run through the middle of the V-I characteristic so that its entire rising edge would be reflected with one network, while its entire falling edge would be reflected with the second. As the current waveforms in EAFs have relatively low deformations, the current would serve as a division criterion. Both the voltage and current data for which the current is rising would belong to one category, while the data for falling current would belong to the second. Formally, the division criterion is as follows:

$$\begin{aligned} v_1 &= v\big|_{\frac{di}{dt}\geq 0},\ i_1 = i\big|_{\frac{di}{dt}\geq 0}, \\ v_2 &= v\big|_{\frac{di}{dt}<0},\ i_2 = i\big|_{\frac{di}{dt}<0}. \end{aligned} \tag{5.1}$$

The example of data division obtained with the above criterion has been visualized in Fig. 5.4.

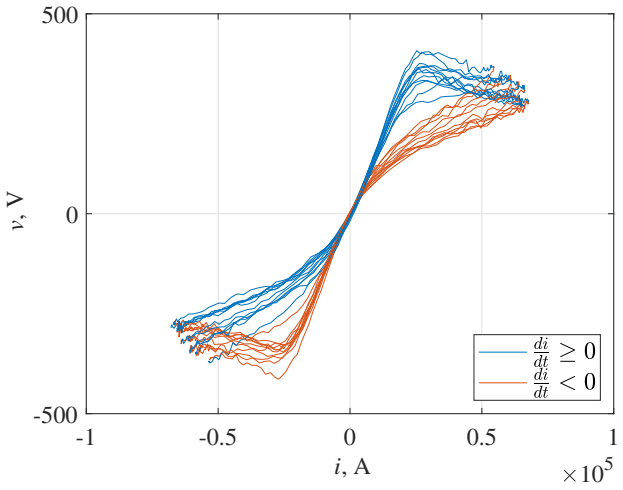

Fig. 5.4: An example of training data division for the Dual-MLP model.

The training, validation, and testing procedure for the dual MLP model remains virtually the same as for a single MLP network. The only difference is related to the division of the measurement data.

Modified nonlinear autoregressive exogenous model

Both models described above are limited to the reflection of a single characteristic obtained by averaging the measurement data. Neither of them is capable of including the changes of the characteristic. To complete a set of shallow models with another, which includes dynamic properties, an application of the NARX model has been proposed. However, the NARX structure cannot be applied directly to the measurement data. In this case, the developed model becomes a grey-box model due to the inclusion of some theoretical structure to this approach.

Again, similarly to the previous Chapter, this model refers to the power balance model of the electric arc. As stated in [23], a slight modification of equation (1.1) can result in its transformation, so the current can be considered as an input and the arc conductance as an output. Such a rearranging of the equation allows the separation of the two static nonlinear components from a single linear dynamic one in the middle. This structure is visible in Fig. 5.5 that presents a graphical block representation of the equation. This form is known as the Hammerstein-Wiener (HW) model, characterized by two nonlinear static blocks on both sides of the linear dynamic block.

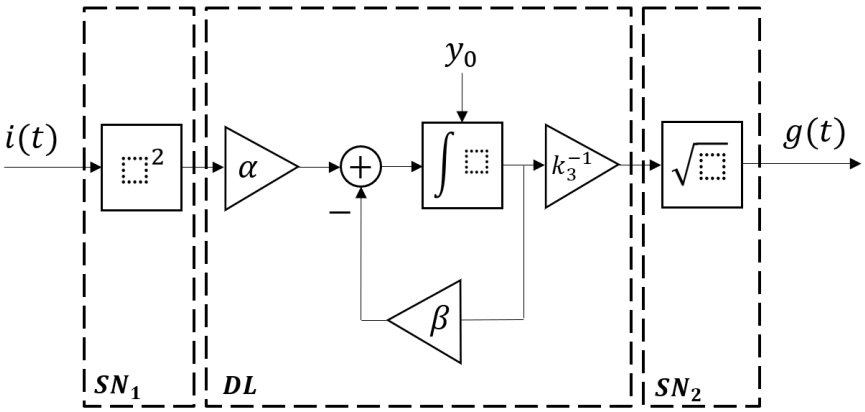

$$\alpha = \frac{k_3}{k_2}(m+4)$$

$$\beta = \frac{k_1}{k_2}(m+4)$$

SN_1 - first static nonlinear block

SN_2 - second static nonlinear block

DL – dynamic linear block

Fig. 5.5: Structure of the Hammerstein-Wiener model of the EAF [23].

Due to the transformation of the power balance model into the HW model form, one can directly implement both nonlinear static blocks using mathematical expressions, while the linear dynamic block can be represented with ANNs. In this case, the NARX model has been applied. Its basic structure has been shown in Fig. 5.6. Its general structure is similar to the MLP network, but NARX additionally includes feedback loop and optional delays of input signals. A delay of size 1 is equivalent to z^{-1} discrete-time operator, which delays input by one sample. However, this exact

structure is not best fitted to represent the dynamic linear block of the HW model. It has been modified to directly reflect the dynamic block (DL), so the delays have remained equal to 1, but the sigmoid activation function had to be changed to a linear one to ensure that the hidden layer output would only be a linear combination of input signal and delays. Additionally, because the output is the arc conductance, it has to be positive. To ensure that there are no negative values outputted, a single neuron in the output layer has been exchanged for a rectified linear unit, which is characterized by a linear function for positive input and 0 for negative ones. This modified NARX network has been presented in Fig. 5.7.

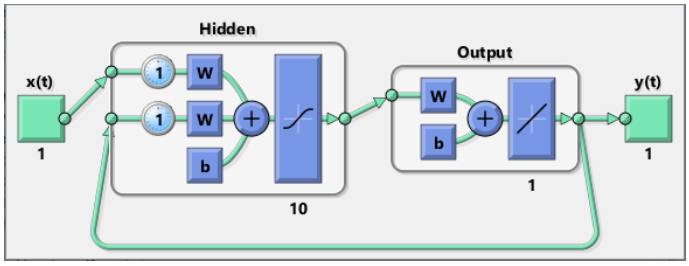

Fig. 5.6: Structure of NARX ANN.

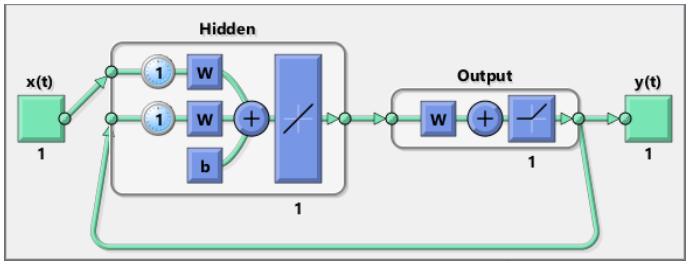

Fig. 5.7: Structure of M-NARX ANN.

Before referring to a numerical example, it is also worth noting that modification of the power balance model to obtain the arc conductance as the output requires recalculation of the measurement data. Calculation of the arc conductance was obtained by applying Ohm's law, but for some samples, the numerical accuracy resulted in outliers, which are very undesirable from the ANN training point of view. As a result, an additional data pre-processing stage is required to remove outliers. The entire data set has been cleared from outliers using the Hampel filter [61]. An example of an outlier in the conductance waveform has been shown in Fig. 5.8.

5.1.2 Deep ANN

Low frequency component

The main idea behind the application of deep learning methods in EAF modeling is to simplify a specific stage of model development. Here, it is again used in the context of a grey-box model. An application of LSTM networks capable of learning and reproducing relatively long data sequences has been proposed. Such networks, due to their versatility and ability to store information from earlier input samples and include them in the current stage, are most often used to predict time-varying phenomena or speech and text processing [62]. Such a LSTM network consists of

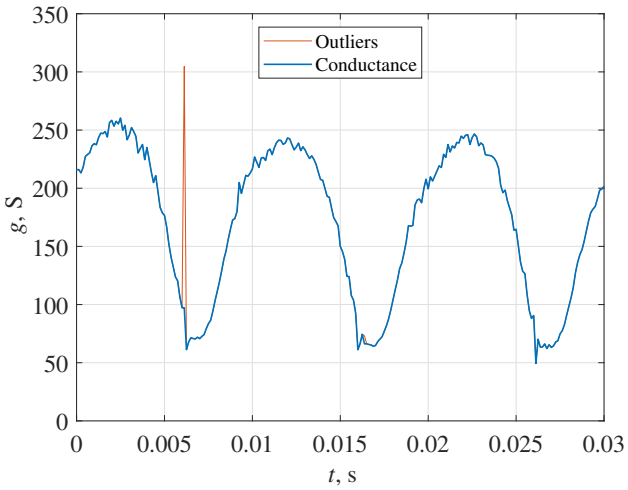

Fig. 5.8: Example of an outlier in EAF's arc conductance waveform.

multiple cells that process the input. A single cell structure has been presented in Fig. 5.9. It consists of separate functions, which, based on an input (x_t) and previous state (c_{t-1}, h_{t-1}), perform the operation of removing unnecessary pieces of information and updating the current state with the relevant data. That is, the "forget" gate removes certain data on the basis of the previous cell state, output, and new input. "Update" gate introduces new information to the cell state, and eventually the "output" gate provides information about the cell state (c_t) and newly calculated output (h_t) to the next cell. This procedure is repeated according to the number of LSTM units. The LSTM networks, similarly to the shallow ones, must be subject to a training, validation, and testing procedure. Training allows fitting of the coefficients governing each LSTM cell so that the entire structure would accurately replicate the output, even over the long term.

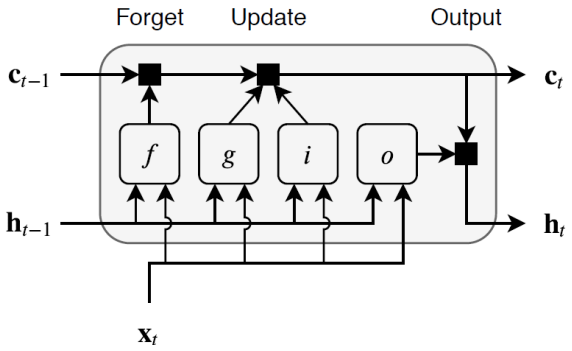

Fig. 5.9: Structure of a single LSTM cell [63].

Those exact features of LSTM networks make them suitable for replication of various signals, including stochastic-like time sequences. Here, three separate LSTM networks have been applied to replicate the K_j stochastic processes, instead of their actual identification. What is important is that a properly conducted training ensures that such deep networks are capable of independent generation of signals with statistical properties similar to the actual realizations of processes K_j from measurement data. Such signals, generated with an appropriate sampling frequency, can feed the model based on power balance, similar to the model from Chapter 3.

In addition to the set of LSTM cells, a network structure must be completed with additional layers to ensure the appropriate flow of data. In the case of time sequence analysis, a standalone solution should consist of a sequence input layer, then the LSTM layer, a fully connected layer, and finally a regression output layer. Each of the separate LSTM networks reflecting each of the K_j processes has the same structure. However, they are trained with different datasets. The structure of a complete LSTM network has been presented in Fig. 5.10.

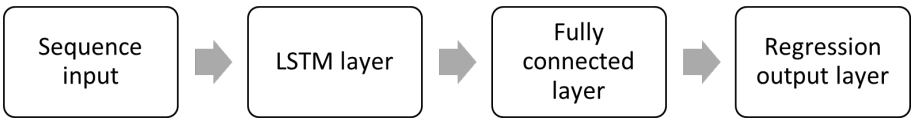

Fig. 5.10: Block diagram of a complete LSTM network.

High frequency component

Because the LSTM models shares the same base as the RDE model, the LSTM model form previous Subsection is limited to accurate reflection of low frequency components of the EAF characteristic. Therefore, a complete model should have an additional component reflecting the high frequency ripples observable in the measurement voltage waveforms. Here again, this component is an addition to the voltage output obtained from the previous subsection, based on linearization of the characteristic in proximity to the operating point. The only difference is due to the fact that the high frequency component is generated by a separate fourth LSTM network. This network is trained with the high frequency signal obtained from filtering the measurement voltage waveform, exactly in the same way as in the case of a RDE model.

5.2 Simulation results and analysis

For the purpose of developing the ANN models of the electric arc, a series of simulations have been carried out. The data obtained from the training of individual networks have been grouped into parts related to shallow models - MLP, dual MLP and M-NARX, and deep learning models - LSTM. The following subsections describe the results obtained for large industrial, small industrial and laboratory EAF separately.

5.2.1 Large industrial EAF

Shallow ANNs

The first developed ANN model was a basic MLP network. Data provided for model development have been divided into three groups: training, validation, and testing, with proportions of 70%, 15% and 15%, respectively. The network has been tested for different hidden layer sizes and activation function types. Eventually, the structure was deployed with 10 hidden units because more neurons only extended the computation time without improving the results. For the transfer function, the commonly used hyperbolic tangent sigmoid function has been selected. This network

has been used for training based on the measurement waveforms obtained for the large industrial EAF - with current as input and voltage as output.

Next, an exemplary clipping of the current waveform has been selected as input for the trained network. In this way, the simulated output voltage was calculated. The results have been presented in the form of a V-I characteristic compared to that in Fig. 5.11. As shown, the MLP model only averages the characteristic of the arc. It does include its nonlinearity but does not reflect any dynamic changes or the hysteresis.

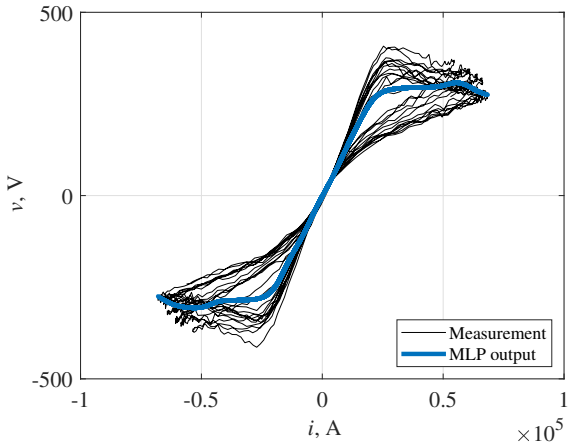

Fig. 5.11: V-I characteristic of the EAF – comparison between the MLP output and measurement data from the large industrial EAF.

An improvement in performance can be achieved by doubling the MLP structure and dividing the measurement data for half-period long frames stretching between consecutive peaks of a relatively low distorted current waveform. The data divided in this way have been used for the development of two MLP networks of identical structure and transfer function as for the single MLP version. In this case, again, the simulated output voltage waveform has been computed using trained networks for an exemplary current frame. The output V-I characteristic was compared with the measurement one in Fig. 5.12. As shown, this model is capable of reflecting the nonlinear characteristic with a hysteresis, but still does not include any changes in the characteristic's shape.

To incorporate the dynamic component into the ANN model, the M-NARX model has been developed. As previously introduced, it is constructed as a replacement for the linear dynamic block of the HW model shown in Fig. 5.5. This application required special data pre-processing consisting of outliers cleaning using appropriate filter. Additionally, the output of the M-NARX model is the arc conductance and not the voltage waveform directly. The exact structure of the M-NARX model remained as proposed in Fig. 5.7. It has single delays, one unit in the hidden layer with linear function, and the rectifying unit in the output transfer function. The intermediate exemplary results, that is, the arc conductance waveform, were compared with the conductance calculated based on the measurement data in Fig. 5.13. These data were then used for the calculation of the output voltage, which was again compared with the measurement data in Fig. 5.14. The model correctly reflects the arc conductance and includes both hysteresis and dynamic changes of the characteristic.

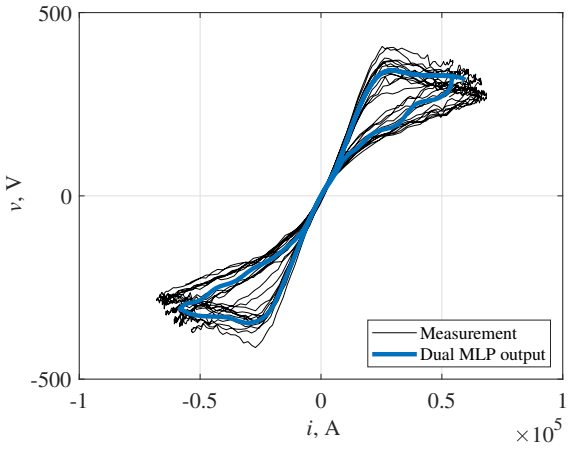

Fig. 5.12: V-I characteristic of the EAF – comparison between the dual MLP output and measurement data from the large industrial EAF.

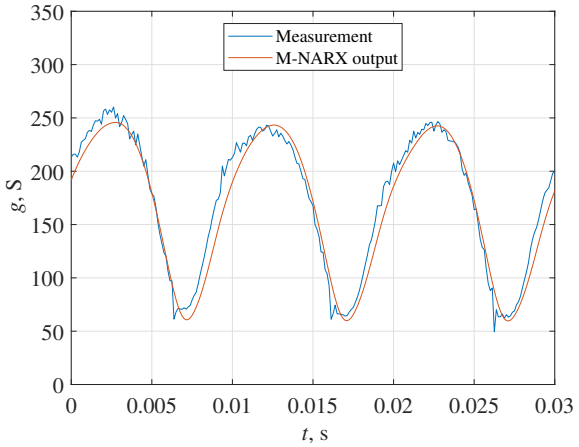

Fig. 5.13: Comparison between conductance waveforms based on data measured and simulated by the M-NARX for the large industrial EAF.

Among the shallow ANNs it was possible to calculate the objective error measure because all models were designed for the most precise reflection of the measurement waveforms, yet without stochastic components. Exemplary output voltage waveforms have been compared graphically in Fig. 5.15. As presented, each model reflects the voltage waveform differently, but all are relatively accurate. In addition, a quantitative assessment has been introduced. For this purpose, the following error measure has been proposed:

$$\epsilon_v = \sqrt{\frac{\int_0^{T_o}[\hat{v}(t) - v(t)]^2 dt}{\int_0^{T_o}[v(t)]^2 dt}} \cdot 100\% = \frac{|\Delta V|}{|V|} \cdot 100\%, \tag{5.2}$$

where:

ϵ_v – percent RMS error,
$v(t)$ – measured voltage data (model target),
$\hat{v}(t)$ – simulated voltage data (model output),
T_o – observation window.

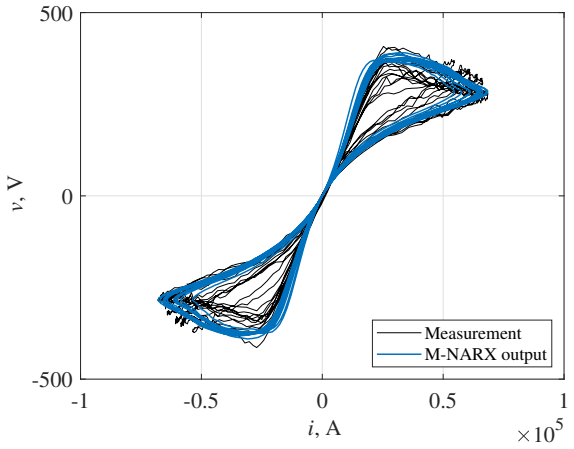

Fig. 5.14: V-I characteristic of the large industrial EAF – comparison between the M-NARX output and measurement data.

This formula describes the RMS value of the error relative to the RMS value of the voltage, expressed as a percentage. For the datasets applied to the development of the ANN models, the results have been presented in Table 5.1. They indicate that despite the lack of a dynamic component in the network structure, it was the dual MLP model characterized by the smallest error and a single MLP with the greatest.

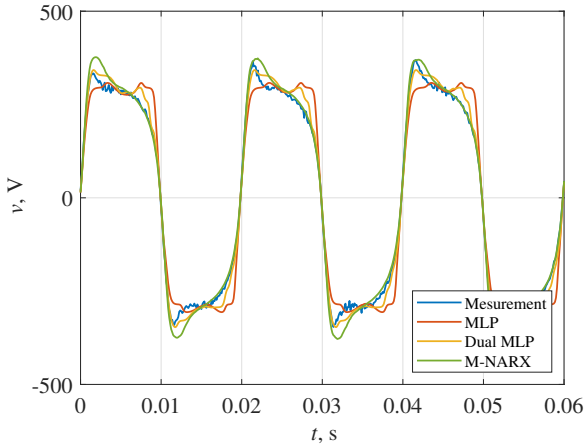

Fig. 5.15: Voltage waveforms – comparison between the outputs of the proposed shallow ANN models obtained for the same input current, for the large industrial EAF.

Deep ANNs

To directly include stochastic components in models based on ANN, deep learning EAF models have been proposed. The first one is oriented on reflection of the low frequency component - the general changes in the arc's V-I characteristic. The main idea behind this approach is to train LSTM networks to reflect stochastic processes, where realizations estimated from the measurement data have been calculated in Chapter 3. Three LSTM models have been trained with these data. Their ability to recall certain features of longer sequences allowed the independent generation of

Table 5.1: Errors of shallow ANN models of the large industrial EAF.

ANN	**Voltage RMS error,** ϵ_v
MLP	16.7%
Dual MLP	9.4%
M-NARX	13.2%

signals with similar statistical features. Various numbers of hidden units were tested and finally the networks were fitted with 300 hidden units in the LSTM layer. Their training was carried out using the Adam Optimizer with a variable learning rate starting from 0.005. The number of training epochs was also investigated in order to obtain the best results, and, in general, training stopped after 500 epochs, with the batch size equal to 128. The output realizations generated independently by each of the networks have been presented in Fig. 5.16. As shown, the signals indeed exhibit stochastic-like behavior.

Similarly to the RDE model, described in Chapter 3, this model provides a realization of discrete-time stochastic processes K_j, which allows calculation of the output voltage based on a given input current. Such a procedure has been conducted to calculate the voltage realization based on a chosen current waveform frame. The results in the form of the V-I characteristic have been compared with the measurement characteristic in Fig. 5.17. As presented, the characteristic changes shape from period to period in a manner similar to that observed in the measurement data.

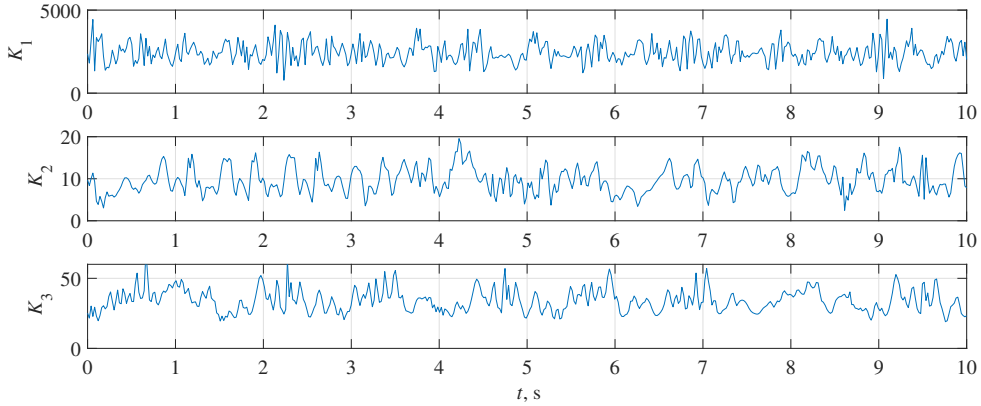

Fig. 5.16: Exemplary realization of K_j coefficients time series obtained from the LSTM model for the large industrial EAF.

Additionally, apart from the first LSTM model, its extension to the high frequency stochastic component has been developed. Similarly to the RDE model, the same high frequency signal filtered out from the voltage waveform was used. A separate fourth LSTM network was trained with this signal in order to replicate it independently in the later stage of development. The network has been trained and, as a result, was able to generate a signal with similar statistical properties. The output high frequency voltage component has been presented in Fig. 5.18. A simple addition to the previous voltage output results in the final LSTM model with a wide frequency spectrum. The overall output characteristic has been presented in

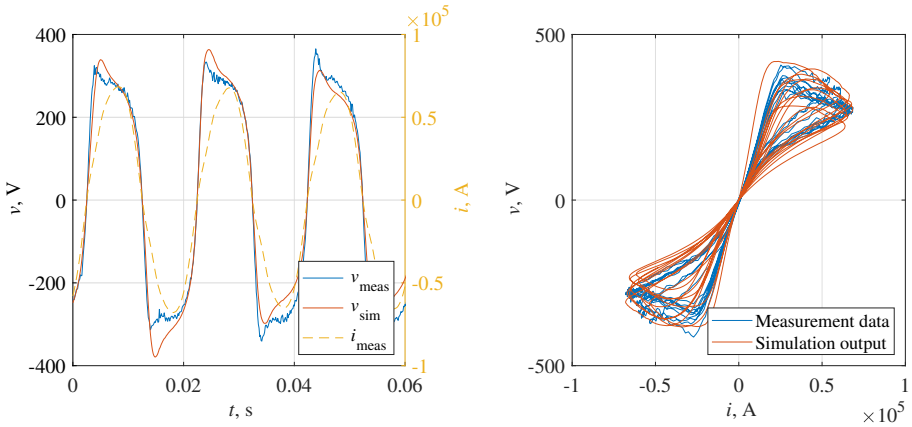

Fig. 5.17: Exemplary V-I characteristic of the large industrial EAF obtained from the LSTM model and measurements.

Fig. 5.19. To provide an additional perspective for the quality of the voltage representation, the figure also presents the voltage waveforms from the measurement data and the second LSTM models. As shown, addition of the high frequency signal allows reflection of stochastic changes related to the general shape of the waveform, as well as ripples in voltage observable in the measurement data.

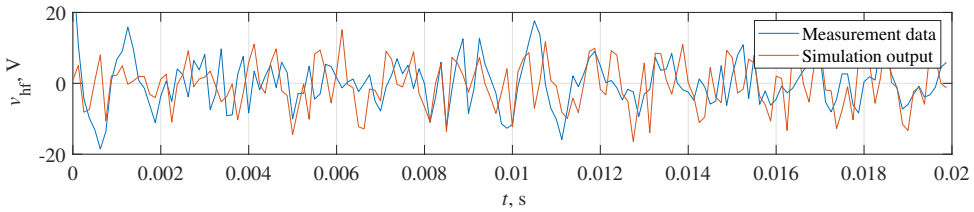

Fig. 5.18: Exemplary realization of high frequency voltage ripples generated by the LSTM network for the large industrial EAF.

5.2.2 Small industrial EAF

Shallow ANNs

Each of the proposed shallow ANN models has been applied separately to the small industrial furnace dataset. The combined results of the shallow model V-I output characteristics have been presented in Fig. 5.20, while exemplary clippings of the voltage waveforms have been compared in Fig. 5.21. As shown, the simplest models perform relatively well, however, the asymmetry present in this dataset results in poor accuracy of the M-NARX model. This problem could be solved by applying a dual M-NARX model, similar to the dual MLP model. However, this solution would require different data division, for which the first quadrant of the V-I characteristic would be modeled by one network and the third quadrant with the other. The performance of the original M-NARX structure has been worse, so to ensure better results for this more complex characteristic, delays of 2 samples have been added to the original input signals. This allows better reflection of the small industrial EAF characteristic. The quantitative assessment has confirmed the above conclusions. The results of the RMS error calculated for the voltage have been placed in Table 5.2.

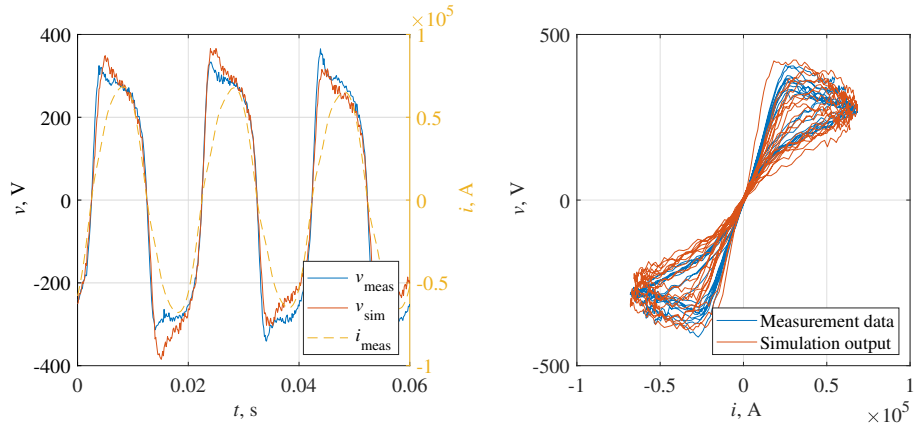

Fig. 5.19: Comparison of the V-I characteristic of the large industrial EAF obtained from the second LSTM model and measurements.

The numbers indicate that both MLP networks have very similar performance and, despite their limitations, outperform the M-NARX model developed based on this dataset.

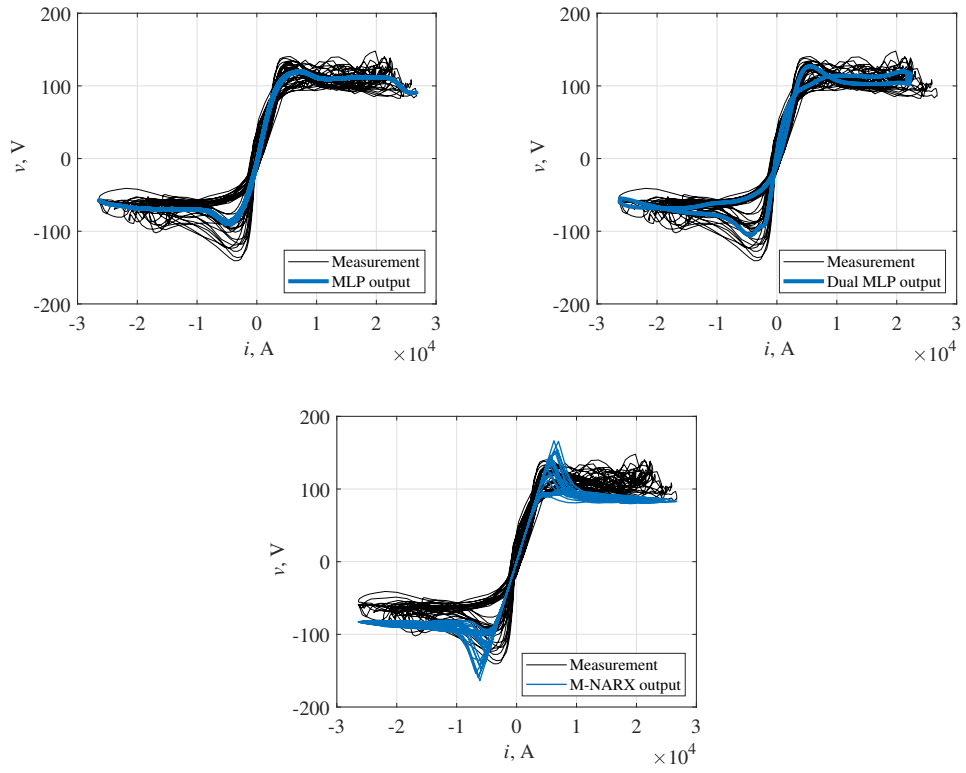

Fig. 5.20: Comparison of the V-I characteristic obtained from the shallow ANNs for small industrial EAF dataset.

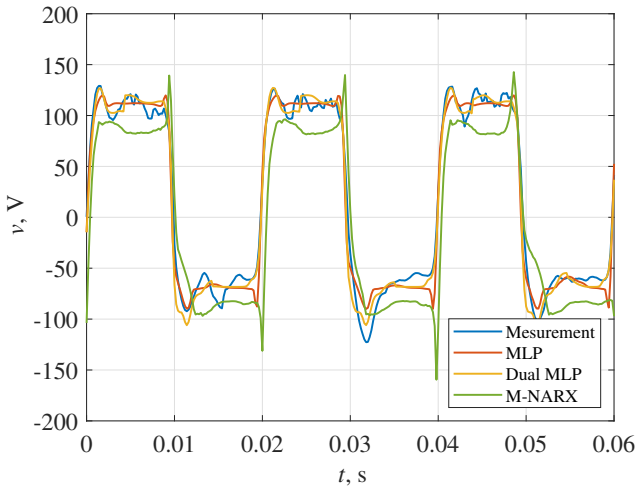

Fig. 5.21: Comparison of the voltage waveforms obtained from the shallow ANNs for small industrial EAF dataset.

Table 5.2: Errors of shallow ANN models of the small industrial EAF.

ANN	**Voltage RMS error,** ϵ_v
MLP	17.2%
Dual MLP	17.0%
M-NARX	29.9%

Deep ANNs

The realizations of stochastic processes K_j of the small industrial EAF have also been applied to the development of a deep learning model. In this case, the procedure remained the same as for the large industrial furnace. The only difference is that optimal results have been obtained for LSTM networks with 300 hidden units for K_1 and K_2, and 350 for K_3. The general structure remained the same. The output realizations generated independently by each of the networks have been presented in Fig. 5.22. In addition, an exemplary realization of the output voltage and a V-I characteristic is shown in Fig. 5.23. As presented, the model accurately reflects the measurement data.

The measurement data obtained from the small industrial EAF also contain the high frequency component, thus the next version of the LSTM model has been developed. This component and the simulation output of the separate LSTM network have been presented in Fig. 5.24. In this case, the network has been fitted with 500 hidden units. Exemplary results of the overall model with both the low and high frequency components have been shown in Fig. 5.25.

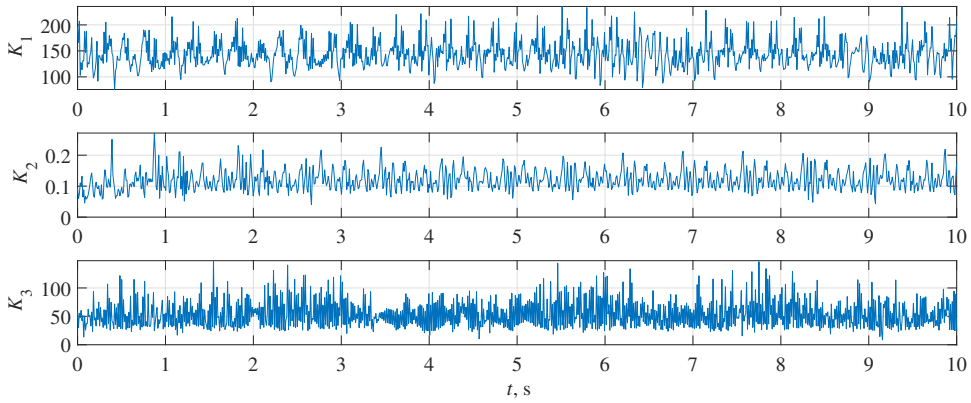

Fig. 5.22: Exemplary realization of K_j coefficients time series obtained from the LSTM model for the small industrial EAF.

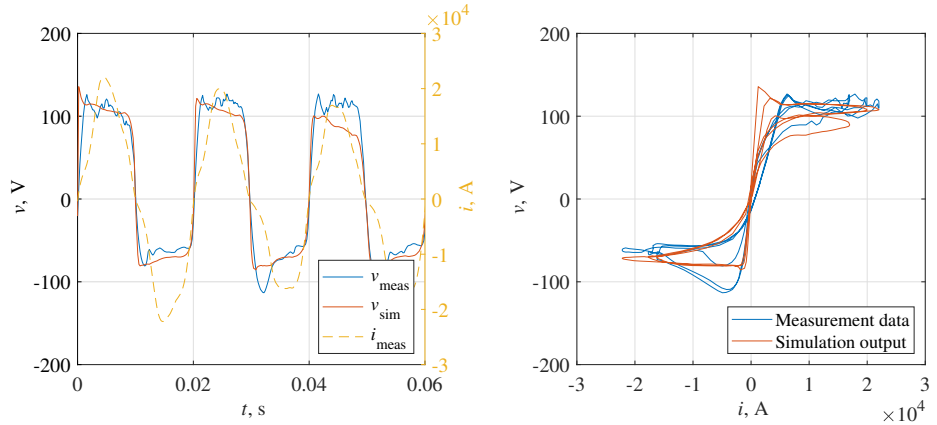

Fig. 5.23: Comparison of the V-I characteristic of small industrial EAF obtained from the LSTM model and measurements.

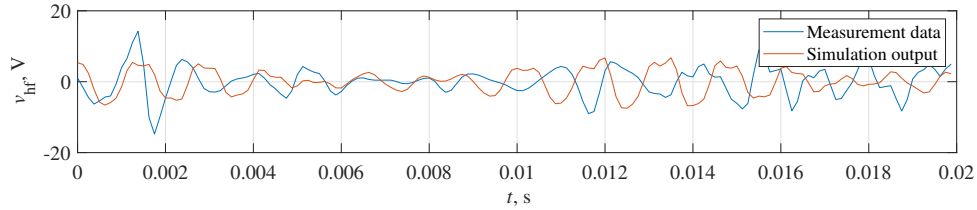

Fig. 5.24: Exemplary realization of high frequency voltage ripples generated by the LSTM network for the small industrial EAF.

5.2.3 Laboratory EAF

Shallow ANNs

Similarly to the previous section, each of the shallow ANN models has been applied again, but to the laboratory furnace dataset. The combined results of the V-I output characteristics of the shallow models have been presented in Fig. 5.26, while exemplary clippings of the voltage waveforms have been compared in Fig. 5.27. As shown, the simplest models perform relatively well, although, the asymmetry present in this dataset results in poor accuracy of the M-NARX model in the same

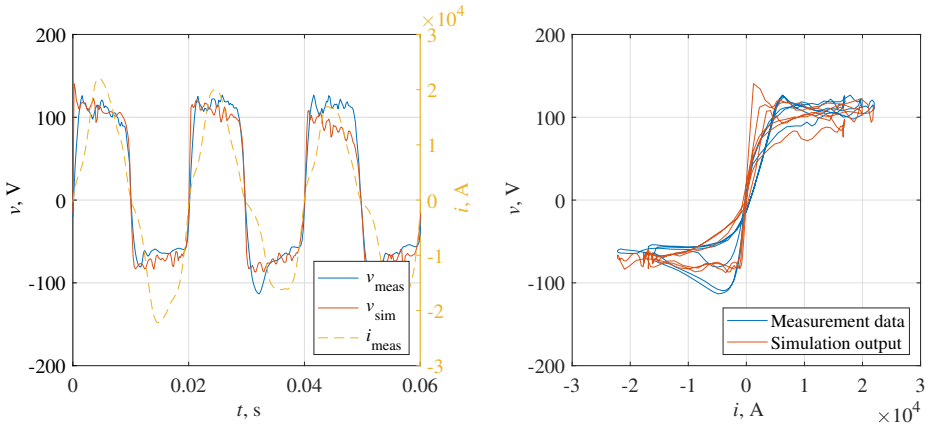

Fig. 5.25: Comparison of the V-I characteristic of the small industrial EAF obtained from the second LSTM model and measurements.

manner as in the case of the small industrial furnace. However, this time the results exhibit even more visible discrepancies with the measurement data. The delays of 2 samples have been added to the original input signals. Without that operation, the accuracy has been significantly worse. Quantitative assessment has confirmed the above conclusions. The results of the RMS error calculated for the voltage have been placed in Table 5.3. The numbers indicate that both MLP networks have very similar performance and, despite their limitations, outperform the M-NARX model developed based on this dataset.

Table 5.3: Errors of the shallow ANN models of the laboratory EAF.

ANN	**Voltage RMS error,** ϵ_v
MLP	21.3%
Dual MLP	24.1%
M-NARX	46.6%

Deep ANNs

The realizations of stochastic processes K_j in the laboratory EAF has been applied for the development of a deep learning model. In this case, the procedure remained the same as for the large industrial furnace. The only difference is that optimal results have been obtained for LSTM networks with 300 hidden units for K_1, 400 for K_2, and 350 for K_3. The general structure remained the same. Fig. 5.28. Additionally, an exemplary realization of the output voltage and the V-I characteristic has been shown in Fig. 5.29. As presented, the model accurately reflects the measurement data.

The measurement data obtained from the laboratory EAF also contains the high-frequency component, so the next version of the LSTM model has been developed. This component, as well as the simulation output of the separate LSTM network, has been presented in Fig. 5.30. In this case, the network has been fitted with 300 hidden units. As shown, the 600 Hz frequency threshold selected for the division between

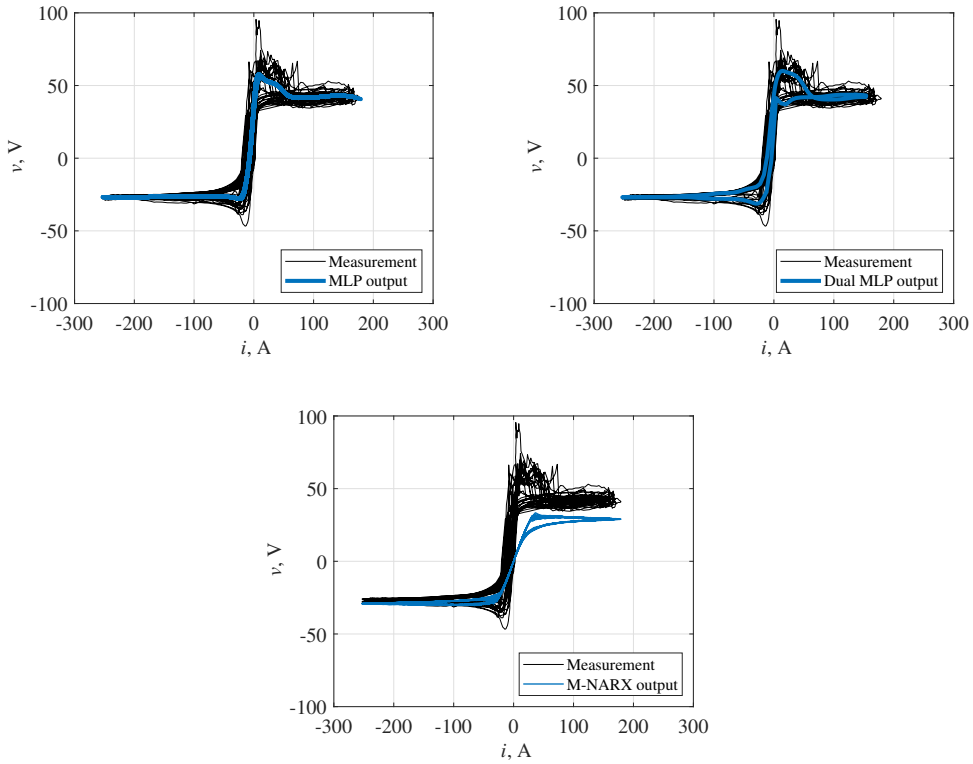

Fig. 5.26: Comparison of the V-I characteristic obtained from the shallow ANNs for laboratory EAF dataset.

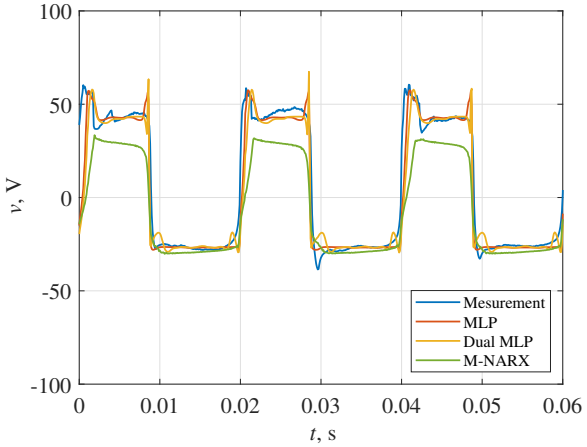

Fig. 5.27: Comparison of the voltage waveforms obtained from the shallow ANNs for laboratory EAF dataset.

the low and high frequency components resulted in exposure of some additional sinusoidal components, which do not fit directly with a simple stochastic process representation. The advantage of using the LSTM network is that those components can be easily included in the model. However, the realizations of individual periods can differ in the content of those components. Exemplary results of the overall model with both low and high frequency component has been shown in Fig. 5.31.

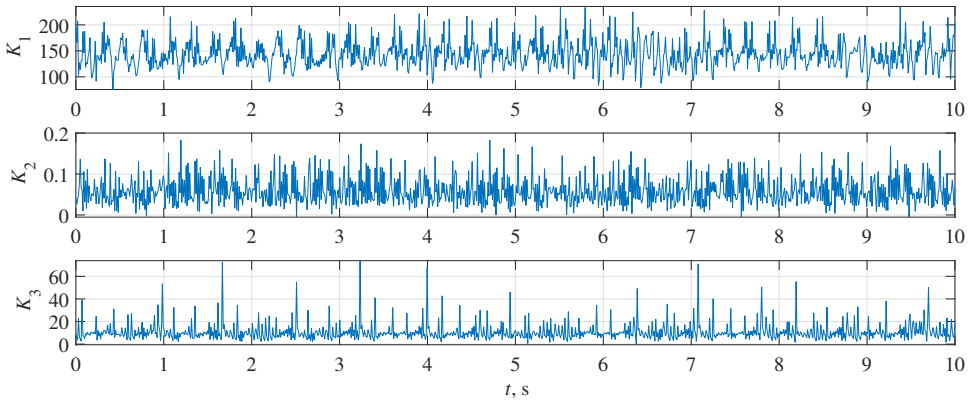

Fig. 5.28: Exemplary realization of K_j coefficients time series obtained from the LSTM model and measurements for the laboratory EAF.

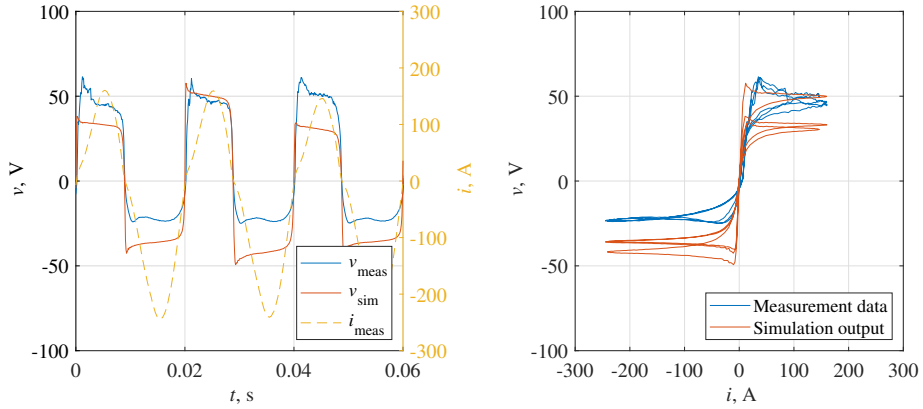

Fig. 5.29: Comparison of the V-I characteristic of the laboratory EAF obtained from the LSTM model and measurements.

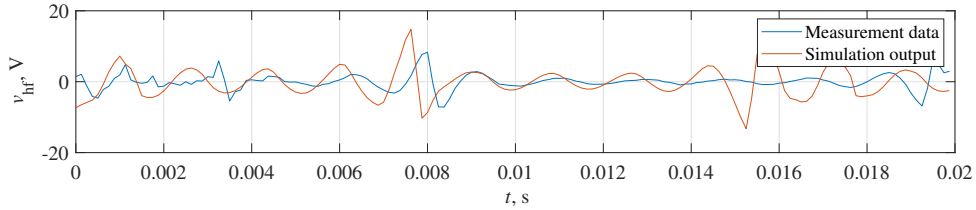

Fig. 5.30: Exemplary realization of high frequency voltage ripples generated by the LSTM network for the laboratory EAF.

Tabular data comparing models developed in this Section provide better insight into the performance of shallow neural network models. A comparison of deep learning models capable of reflecting more complex stochastic behavior (apart from graphical presentation of the output) is more difficult due to the need of applying statistical measures. The error calculated directly between two realizations of stochastic processes would not be correct. For this reason, a more detailed comparative analysis including measures of accuracy of deep leaning models in terms of their stochastic properties has been presented in Chapter 7.

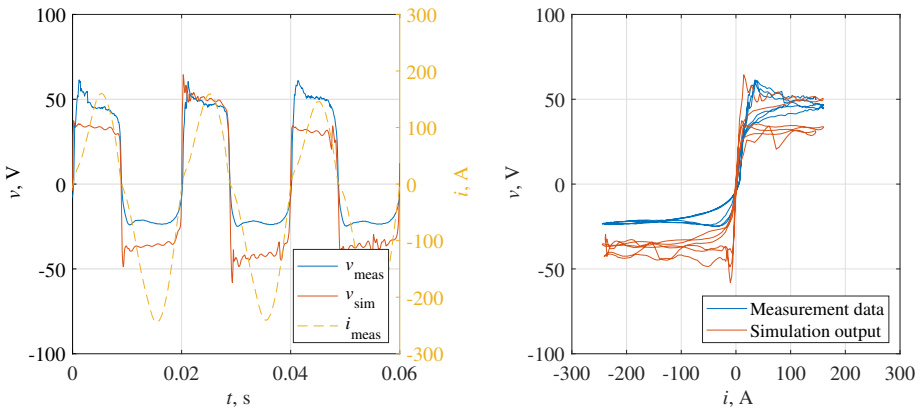

Fig. 5.31: Comparison of the V-I characteristic obtained from the second LSTM model and measurements for the laboratory EAF.

Chapter 6

Fractional order EAF model

The three previous chapters that present RDE, chaotic, and ANN models aim to improve the model of the deterministic power balance equation of the electric arc phenomenon by including stochastic or stochastic-like components. This procedure leads to better reflection of the real phenomena that occur in power systems with EAFs. This Chapter, in turn, is oriented toward improving the deterministic component itself. Namely, the following sections are related to the question if the electric arc can be modeled more accurately with power balance equation but generalized in order to include a fractional order integro-differential operator instead of classic differentiation of order 1.

6.1 Fractional order power balance equation

The power balance equation (1.1) can be simplified by adding an auxiliary variable y, as shown in [64]:

$$y = r^{m+4}, \tag{6.1}$$

then, for $n = 2$ and $m = 0, 1, 2$ it can be brought to a linear differential equation:

$$\frac{\mathrm{d}y(t)}{\mathrm{d}t} = -\beta y(t) + f(t), \tag{6.2}$$

where:

$$f(t) = \gamma\ i^2(t), \tag{6.3}$$

$$\beta = \frac{(m+4)k_1}{k_2}, \tag{6.4}$$

$$\gamma = \frac{(m+4)k_3}{k_2}. \tag{6.5}$$

Transformation of the original equation into a linear one (6.2) additionally results in the obtaining of a closed form solution, which simplifies the calculations and opens new ways to take into account the stochastic nature of the arc phenomena [65].

Similarly to the approach presented in the ANN M-NARX model, this equation can be presented in the form of a SISO block model. A graphic representation of the block model has been presented in Fig. 6.1. However, this time the output is not

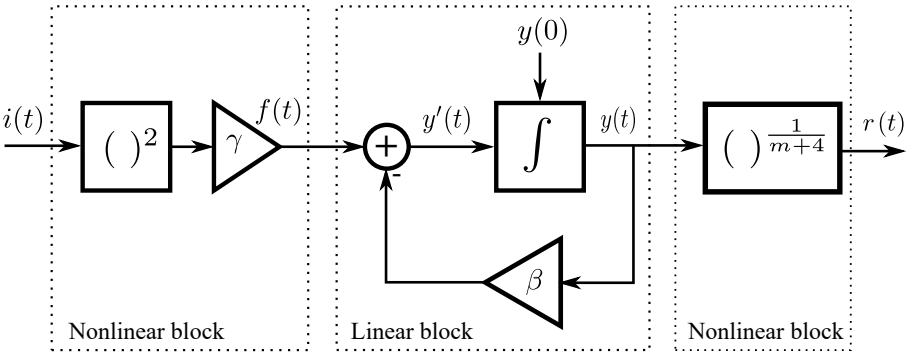

Fig. 6.1: Hammerstein-Wiener model of the EAF.

the arc conductance but the arc column radius. The linear dynamic model visible in the middle of nonlinear static blocks is a direct reflection of (6.2).

In practice, the HW model is implemented as a discrete system and thus its input and output signals consist of samples corresponding to the continuous signals. Identification algorithms provide information on the parameters of this discrete system. The linear block of the HW model corresponds to a difference equation [23]:

$$\frac{1}{T_\mathrm{s}}(y[k]-y[k-1])+\beta y[k]=f[k], \qquad y[k]=y(kT_\mathrm{s}), \quad f[k]=f(kT_\mathrm{s}), \tag{6.6}$$

where:

T_s – sampling period (time step of calculation),
$y[k]$ – discrete time signal, $k=1,2,3,...$,
$y[0]$ – initial condition.

After some transformation of the above equation, the numerical solution of the linear difference equation in the HW EAF model can be expressed as:

$$y\,[k]=\eta(f\,[k]+\frac{1}{T_\mathrm{s}}y\,[k-1]), \tag{6.7}$$

where:

$$\eta=\frac{T_\mathrm{s}}{1+\beta T_\mathrm{s}}. \tag{6.8}$$

The discrete version of EAF HW shown in Fig. 6.1 has been presented in Fig. 6.2, where the block z^{-1} denotes a delay of one sample.

The main idea behind the EAF model presented in this Chapter is to generalize the HW model by replacing a classical integral operator with a fractional order integro-differential operator. Such a continuous operator ${}_a\mathrm{D}_t^\alpha$ is defined as [66]:

$${}_a\mathrm{D}_t^\alpha=\begin{cases}\frac{\mathrm{d}^\alpha}{\mathrm{d}t^\alpha} & :\alpha>0,\\ 1 & :\alpha=0,\\ \int_a^t(\mathrm{d}\tau)^\alpha & :\alpha<0,\end{cases} \tag{6.9}$$

where a and t are the limits of the operation and α is the order of the fractional operator $\alpha\in R$.

Several definitions for the general fractional operator have been developed which are named after their inventors. The most popular definitions include, Riemann-Liouville (RL), Grünwald-Letnikov (GL), Hadamard, or Sonin-Letnikov. In the twentieth century, many new definitions were proposed by Riesz, Miller-Ross, Weyl, and Caputo, etc. New definitions, which are emerging to this day, are proof that theory and possible new applications of fractional calculus are still interesting to researchers. Although there are several definitions of fractional operators, their application in numerical analysis is limited. However, there are some methods that can approximate the solution of fractional order differentiation and integration. Here, the classical Grünwald-Letnikov (GL) definition has been chosen. It is often used for numerical calculations and simulations. It is given by:

$$ {}_a\mathrm{D}_t^{\alpha} y\left(t\right) = \lim_{T_\mathrm{s}\mapsto 0} \frac{1}{T_\mathrm{s}^{\alpha}} \sum_{j=0}^{\left\lfloor \frac{t-a}{T_\mathrm{s}} \right\rfloor} (-1)^j \binom{\alpha}{j} y\left(t - jT_\mathrm{s}\right), \tag{6.10} $$

where $\lfloor \cdot \rfloor$ denotes the integer part of the argument. For a wide class of functions, the GL definition, as well as RL and Caputo, is equivalent when $y(a) = 0$ [67].

The fractional order extension of the linear differential equation (6.2) with the integro-differential operator results in the following:

$$ \frac{\mathrm{d}^{\alpha} y\left(t\right)}{\mathrm{d}t^{\alpha}} = -\beta y\left(t\right) + f\left(t\right). \tag{6.11} $$

Moving to the discrete implementation by applying the GL definition (6.10) to (6.11), one obtains the following:

$$ \frac{1}{T_\mathrm{s}^{\alpha}} \sum_{j=0}^{k} c_j^{\alpha} y\left[k-j\right] + \beta y\left[k\right] = f\left[k\right], \quad k = 1, 2, 3, ..., \tag{6.12} $$

where c_j^{α} (j= 0, 1, ..., k) are binomial coefficients (see [68]). They can be calculated using a recursive formula:

$$ c_0^{\alpha} = 1, \; c_j^{\alpha} = \left(1 - \frac{1+\alpha}{j}\right) \cdot c_{j-1}^{\alpha}. \tag{6.13} $$

After rearranging the terms in (6.12), the numerical solution of the fractional order linear differential equation in the HW EAF model can be expressed as:

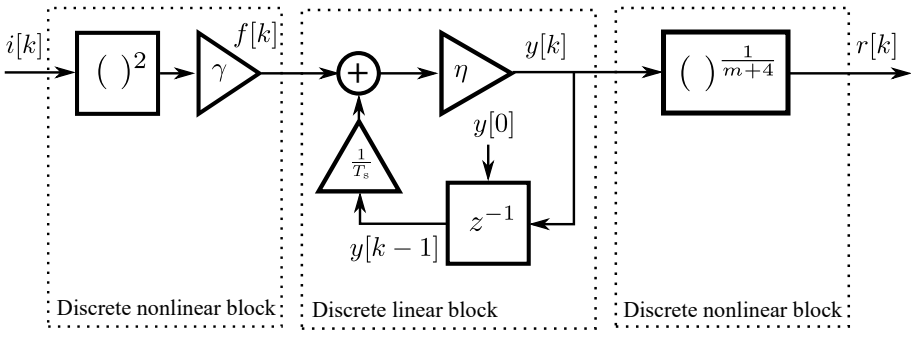

Fig. 6.2: Discrete HW model of an EAF [23].

$$y\left[k\right] = \eta_{\alpha}(f\left[k\right] - \frac{1}{T_{\mathrm{s}}^{\alpha}} \sum_{j=1}^{k} c_j^{\alpha} y\left[k-j\right]), \tag{6.14}$$

where:

$$\eta_{\alpha} = \frac{T_{\mathrm{s}}^{\alpha}}{1+\beta T_{\mathrm{s}}^{\alpha}}. \tag{6.15}$$

It is worth stressing that for $\alpha = 1$ the solution (6.14) simplifies to (6.7). The discrete fractional order HW model of an EAF that takes into account (6.14) has been presented in Fig. 6.4. The effects of varying α order have also been visualized by calculating the voltage waveform based on an exemplary period-long frame taken from the measurement data. The current waveform was repeatedly fed as input to the fractional model with constant noninteger order. Each time, the constant α was different. The k_j coefficients have been set to a constant and optimal value. This allowed calculation of the set of voltage waveforms, each related to a different fractional order. The results have been presented in Fig. 6.3. If the model is implemented in the system with limited resources, at the cost of reduced accuracy, the number of delay elements in the diagram can be reduced and limited to a given number, taking into account that the coefficients c_j^{α} decrease to 0 as j increases (see Table 6.1).

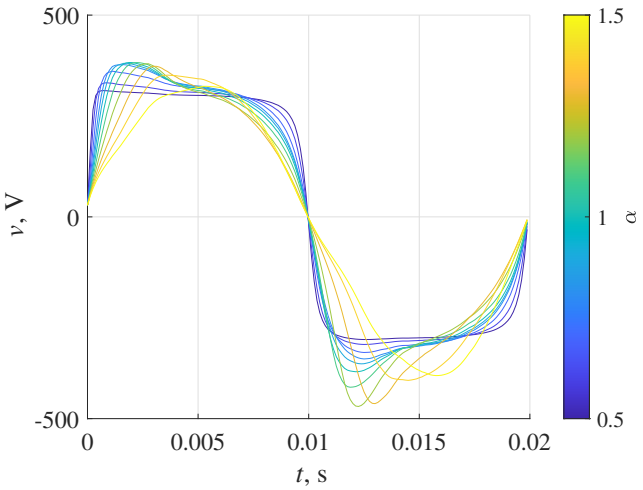

Fig. 6.3: Comparison of the shape of the output voltage depending on the value of α with the optimal coefficients k_j (j = 1, 2, 3).

Formula (6.14) describing the solution to a discrete fractional order differential equation has been used to evaluate the usefulness of the fractional order HW model of an EAF. The results of parameter identification and modeling have been presented and compared with the classical case of integer order in the next section. Calculations also have been validated using different methods proposed in [69]. Results obtained for both methods are consistent.

6.2 Simulation results and analysis

Similarly to the main concept of this thesis described in the RDE model in Chapter 3 for the fractional model, the results related to the estimation of order α of the

Table 6.1: Binomial coefficients c_j^{α}.

j	$\alpha = 0.8$	$\alpha = 0.9$	$\alpha = 1.0$	$\alpha = 1.1$	$\alpha = 1.2$
0	1.0000	1.0000	1.0000	1.0000	1.0000
1	-0.8000	-0.9000	-1.0000	-1.1000	-1.2000
2	-0.0800	-0.0450	0.0000	0.0550	0.1200
3	-0.0320	-0.0165	0.0000	0.0165	0.0320
4	-0.0176	-0.0087	0.0000	0.0078	0.0144
5	-0.0113	-0.0054	0.0000	0.0045	0.0081
6	-0.0079	-0.0037	0.0000	0.0030	0.0051
7	-0.0059	-0.0027	0.0000	0.0021	0.0035
8	-0.0045	-0.0020	0.0000	0.0015	0.0025
9	-0.0036	-0.0016	0.0000	0.0012	0.0019
10	-0.0030	-0.0013	0.0000	0.0009	0.0015

model equation have been presented together with the estimation of the coefficients k_j. The following subsections describe the results obtained for all datasets. In each subsection, two main concepts are tested, one with variable noninteger order and one with constant noninteger order of the integrodifferential operator.

6.2.1 Large industrial EAF

The optimization procedure described in the previous Section leads to the realizations of stochastic processes K_j, as well as the stochastic process representing changes of order α. The introduction of an additional parameter to optimize resulted in a change in the optimal values of the coefficients k_j for particular periods. The global optimum for optimization of the goal function with four decision variables leads to significantly different values of the estimated coefficients. It is worth stressing that the results obtained retained their stochastic characteristics. The most significant difference is the range of coefficient value changes and the shape of their distribution. Approximate representations of these distributions compared to the realizations of the classic version, that is, with $\alpha = 1$, have been presented in Fig. 6.5. As shown, the most significant difference occurred in the case of the K_2 process, namely its range of values increased, but the general shape of the distribution remained similar.

Regarding the order α of the equation itself, it has been estimated similarly to the remaining coefficients, separately for each signal period at the same time as the coefficients k_j. This led to the realization of another stochastic process, describing the random changes of α. The time sequence of this realization has been shown in Fig. 6.6, while its distribution is shown in Fig. 6.7. As presented, fractional order exhibits a behavior similar to that of a stochastic process realization, with a median around 0.6.

The introduction of the variable α leads to better fitting of the simulated voltage waveform to the measurement data. To visualize this effect, an exemplary period of both the simulated voltage with classic $\alpha = 1$, $\alpha = var$ and the measured voltage has been selected. The error between each case and the measured voltage has been calculated and plotted separately to highlight the differences. The plots have been

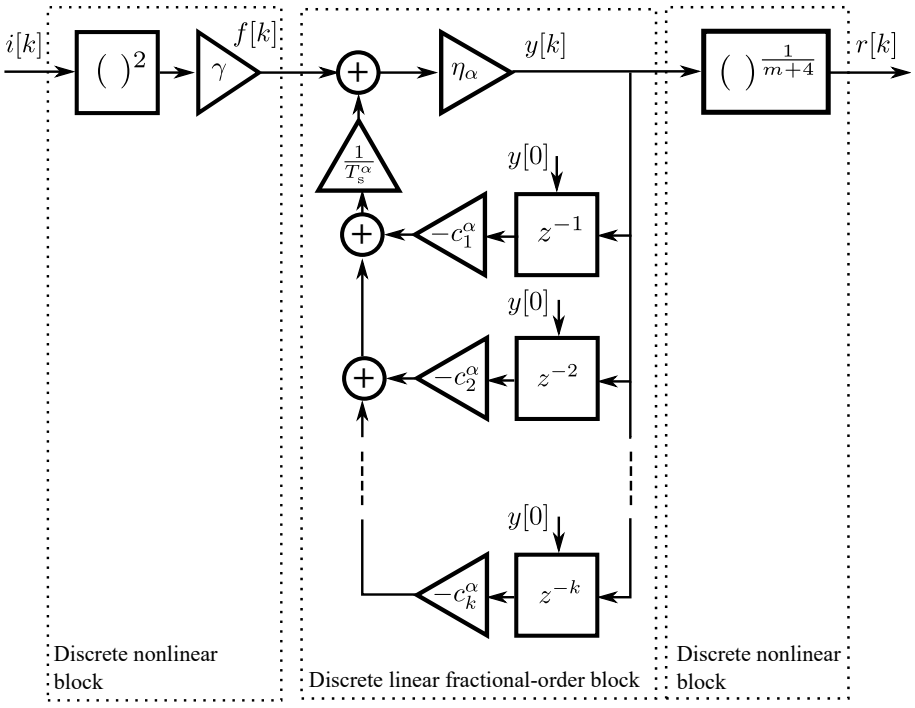

Fig. 6.4: The discrete Hammerstein-Wiener fractional order model of EAF.

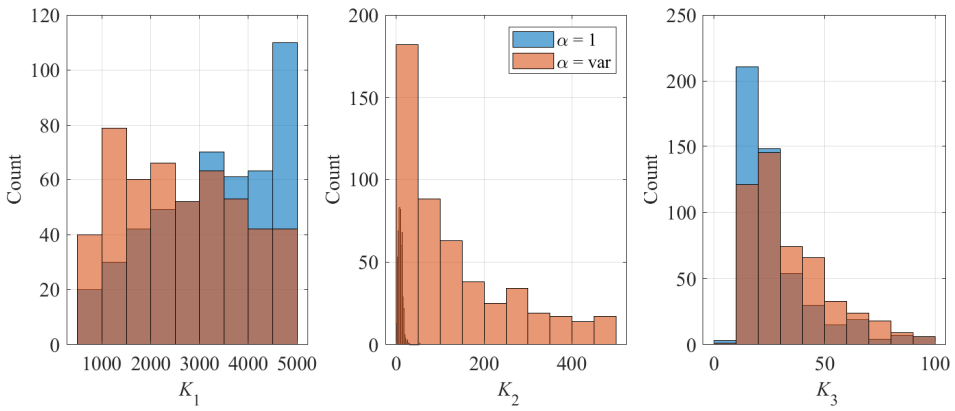

Fig. 6.5: Histograms of K_j $(j = 1, 2, 3)$ for the classical case with $\alpha = 1$ and for the variable α for the large industrial EAF.

presented in Fig. 6.8. As shown, along this exemplary period, the case $\alpha = var$ is characterized with a smaller error in the measured data than in the case of the ordinary approach.

To gain a more detailed understanding of the error characteristics, the errors related to each of the periods have been visualized using a box plot. The results have been shown in Fig. 6.9. The box edges indicate the 25th and 75th percentiles of the errors, while the line inside indicates the median of the dataset. The whiskers cover 99% confidence intervals calculated based on the standard deviation. The remaining points indicated with separate markers appear individually. As shown, the introduction of the variable order α resulted in a reduction of the error in the value of its median and overall distribution. Although the 25th percentile remained similar, the fractional order significantly lowered the remaining values.

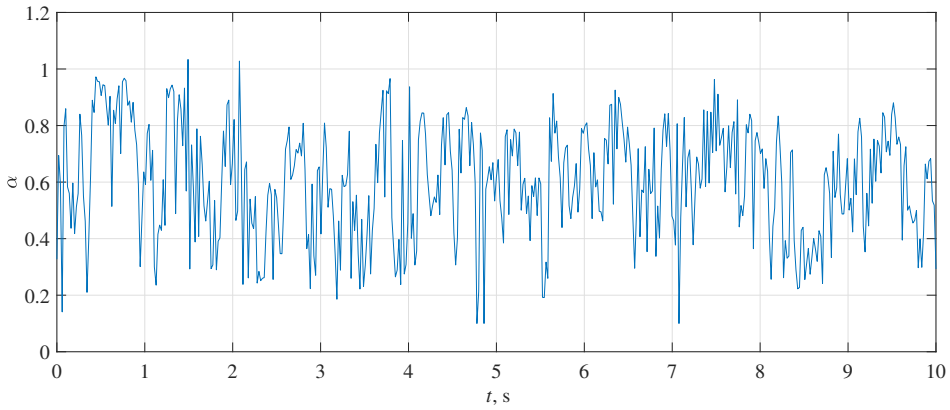

Fig. 6.6: Realization of discrete-time stochastic process of α value for the large industrial EAF.

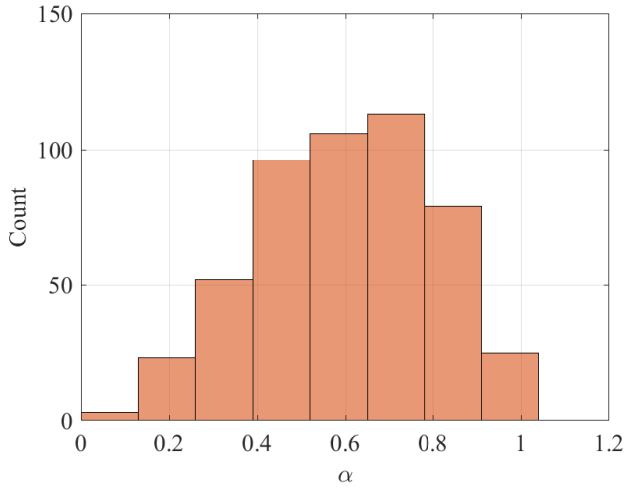

Fig. 6.7: Histogram of the estimated coefficient α for the large industrial EAF.

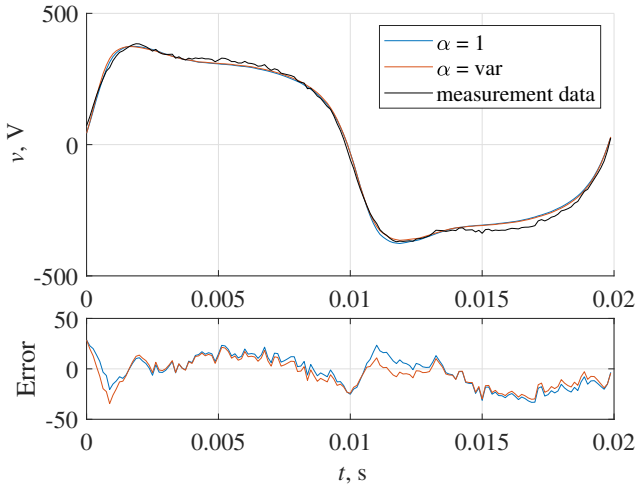

Fig. 6.8: Exemplary voltage waveform of the large industrial EAF fractional model fitted to the measurement data and its error.

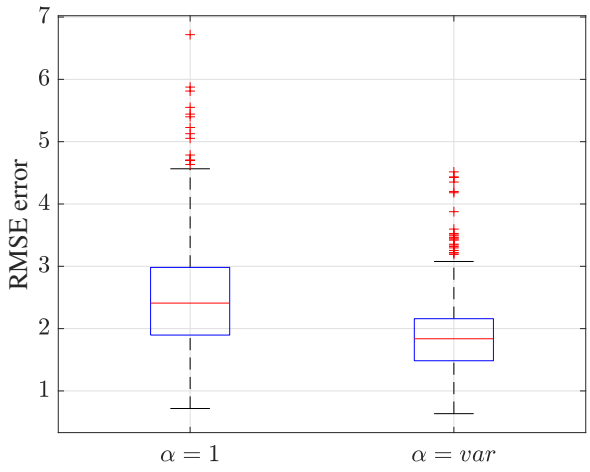

Fig. 6.9: Box plots of errors for all frames for both constant and variable α for the large industrial EAF

Despite the better accuracy of the model including the fractional order separately for each signal period, it is interesting to investigate if and how a constant noninteger value α could be chosen to still maintain improvement against the classic $\alpha = 1$ case. In this way, the model would be simpler because it would not require considering an additional stochastic process that represents the changes of α from period to period. To determine which value could be useful, two approaches have been applied. The first is to use the median value of the realization of α from Fig. 6.6, that is, $\alpha = 0.606$. The second was carried out using sweep analysis, in which the entire optimization procedure of coefficients k_j was carried out period-wise, but for the constant α that was iteratively repeated for the incremented value. The sweep has been carried out with the basic step of 0.05, which was reduced around the minimum error to 0.005. The results have been presented in Fig. 6.10. As shown, the minimal error was obtained for $\alpha = 0.755$, which further justifies the application of fractional order model to the electric arc phenomena.

To compare the results for each approach presented, the error medians have been calculated and compared. The results have been collected in Table 6.2. As noted, the case with variable fractional order is characterized by the highest improvement rate, close to 25%. The result with minimum error obtained from the sweep analysis with constant α is slightly worse, and the result for α median calculated from its stochastic realization is the worst, with an improvement of around 20%. The fact that every proposed fractional order application to EAF modeling resulted in a significant improvement in the accuracy of the model is worth stressing.

Table 6.2: RMSE median for large industrial EAF fractional model.

$\alpha = 1$	$\alpha = var$	$\alpha = 0.606$	$\alpha = 0.755$
2.41	1.81	1.91	1.82
RMSE change	-24.8%	-20.8%	-24.3%

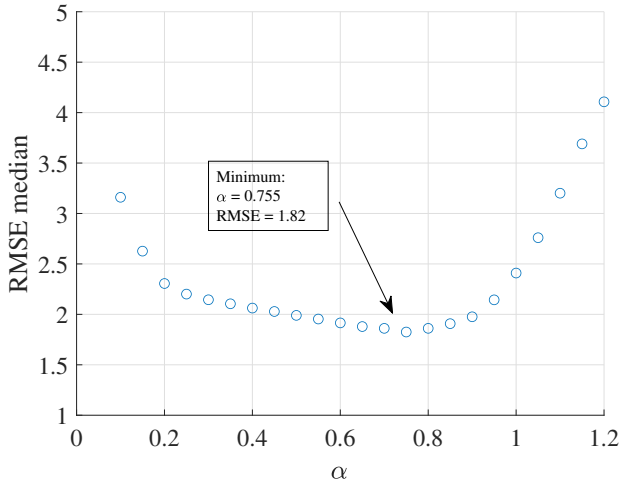

Fig. 6.10: Relationship of the error median depending on the value of the constant order α of the applied fractional differential equation for the large industrial EAF.

6.2.2 Small industrial EAF

The procedure presented in the previous section has been repeated for the dataset obtained from the small industrial EAF. The results of the analysis of the realizations of the K_j and α processes have been presented below. Fig. 6.11 shows the histograms of the calculated values compared to the classical case for $\alpha = 1$. The realization of the variable α has been presented in Fig. 6.12. As shown, for this dataset the range of values is different from that of a large industrial furnace. The most significant difference is related to the distribution of α. The median was equal to $\alpha_{med} = 1.178$ which exceeds the range of the large industrial furnace. To ensure that this value is correct, the other fragments of the measurement waveforms have been investigated. The analysis indicated that the distribution of α actually changes compared to the large furnace and that the median of α is greater than 1. Variations of order indicate that some short-term phenomena occurring in EAFs are better reflected with $\alpha > 1$, while others with $\alpha < 1$, as shown, for example, around the 7th second of realization in Fig. 6.12. The exact reason for this behavior may lie in the movement and properties of the metal charge inside the furnace hearth. In terms of the error related to this approach, the introduction of a fractional and variable order α again resulted in an improvement in accuracy. An example period of the voltage waveform and the error between simulation and measurement have been shown in Fig. 6.13. This figure additionally presents boxplots related to the results obtained. The graph indicates that the range and median error made have decreased compared to the classical approach with $\alpha = 1$. This fact has been supported by the calculations of the error change presented in Table 6.3.

Table 6.3: RMSE median for the small industrial EAF fractional model.

$\alpha = 1$	$\alpha = var$	$\alpha = 1.178$	$\alpha = 1.300$
14.02	12.53	13.54	12.87
RMSE change	-10.6%	-3.4%	-8.2%

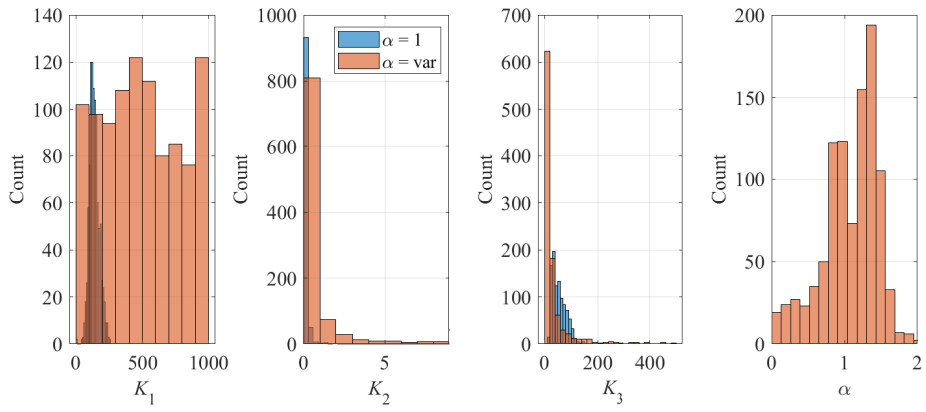

Fig. 6.11: Histograms of coefficients K_j $(j = 1, 2, 3)$ for the classical case with $\alpha = 1$ and for the variable α for the small industrial EAF.

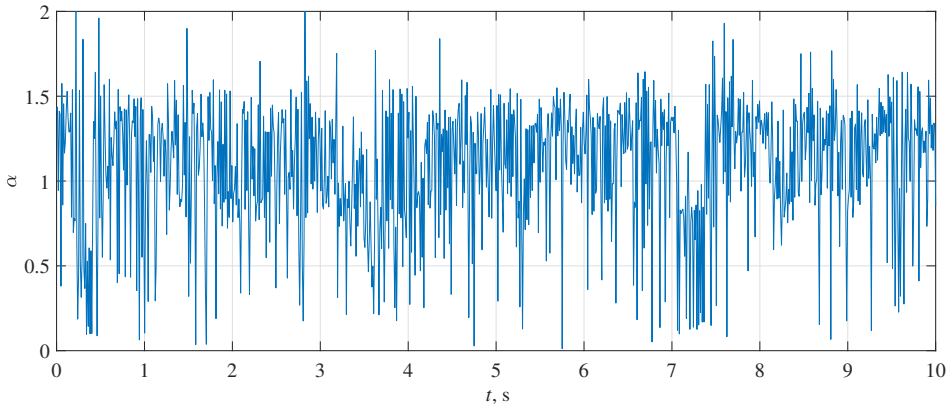

Fig. 6.12: Realization of discrete-time stochastic process of α value for the small industrial EAF.

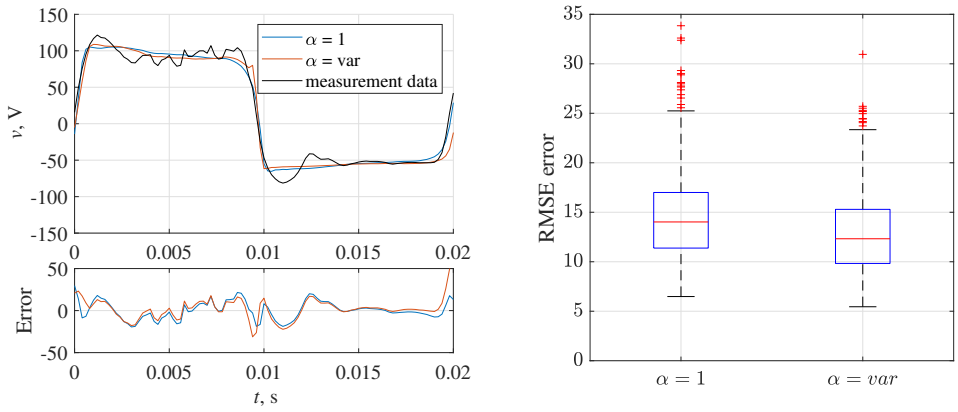

Fig. 6.13: Exemplary voltage waveform and box plot of RMSE errors of the small industrial EAF fitted to measurement data.

Apart from the classical case for $\alpha = 1$, the general $\alpha = var$, and $\alpha_{med} = 1.178$ Table 6.3 includes the RMSE error calculated for α chosen based on the lowest RMSE median among other cases investigated by sweep analysis with constant α, the results of which have been presented in Fig. 6.14. As shown, every approach

including the fractional order results in error reduction. The $\alpha = var$ case improves accuracy the most.

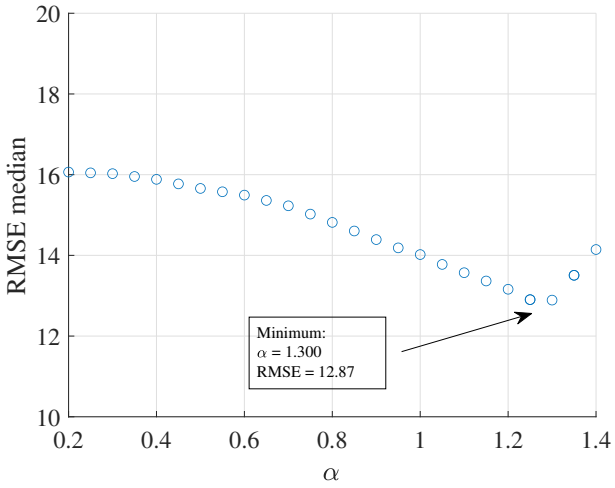

Fig. 6.14: Relationship of the median error according to the value of the order of the applied constant fractional differential equation α for the small industrial EAF.

6.2.3 Laboratory EAF

The fractional order model has been once again recalculated on the basis of the laboratory furnace measurement data. The comparison of the K_j and α distributions between classical $\alpha = 1$ and $\alpha = var$ has been presented in Fig. 6.15. The realization of α has been shown in Fig. 6.16. The results confirm that the phenomena that occur within the furnace influence the optimal value of α. The laboratory furnace is the smallest, where very little metal charge can be placed inside the crucible compared to industrial installations. Therefore, its thermodynamic constant is much lower than in the case of other furnaces. This, in turn, results in a shift of the local mean value of α visible in Fig. 6.16. At first α is generally closer to 1, but during progressive heating of the crucible by the arc, the value tends to decrease. The observed behavior differs from the results connected with other tested installations. However, the overall approach again has brought improvement in the model accuracy. An example period of the voltage waveform and the error between simulation and measurement have been shown in Fig. 6.17. This figure additionally presents boxplots related to the obtained results. The graph indicates that the range and median error made have been decreased compared to the classical approach with $\alpha = 1$. This fact has been supported by the calculation of the change in error presented in Table 6.4.

Table 6.4: RMSE median for the laboratory EAF fractional model.

$\alpha = 1$	$\alpha = var$	$\alpha = 0.777$	$\alpha = 0.715$
3.50	3.21	3.34	3.33
RMSE change	-8.4%	-4.8%	-5.0%

Apart from the classical case for $\alpha = 1$ and more general $\alpha = var$, Table 6.4 includes RMSE error calculated for the constant α chosen based on the procedure

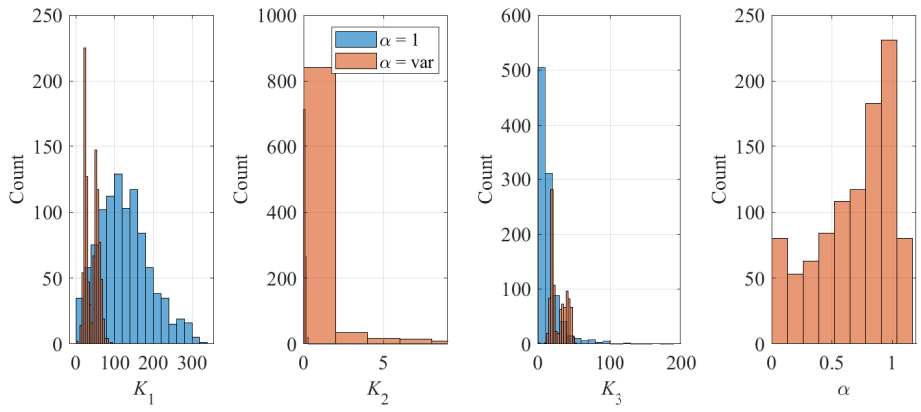

Fig. 6.15: Histograms of coefficients K_j $(j = 1, 2, 3)$ for the classical case with $\alpha = 1$ and for the variable α for the laboratory EAF.

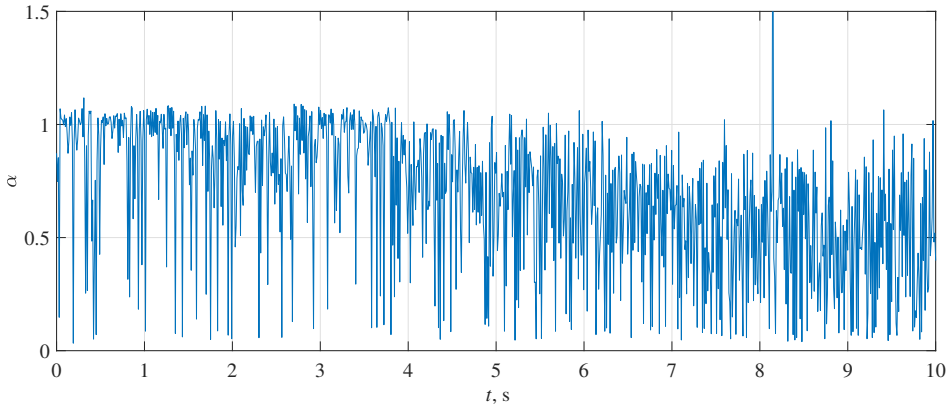

Fig. 6.16: Realization of discrete-time stochastic process of α value for the laboratory EAF.

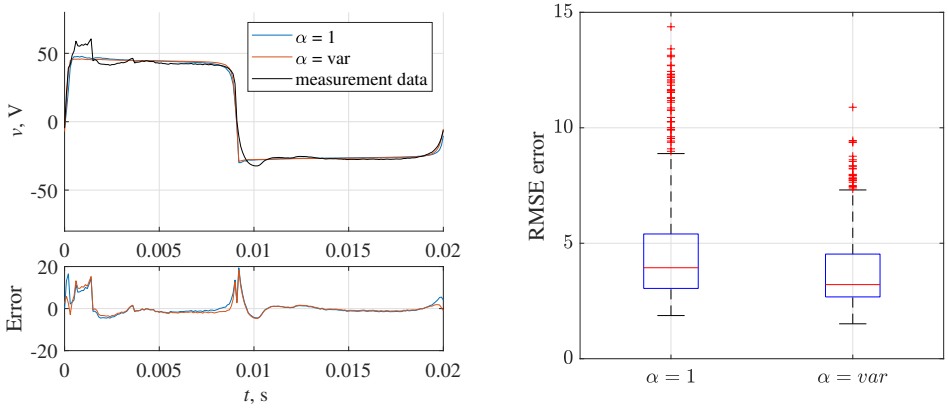

Fig. 6.17: Exemplary voltage waveform and box plot of RMSE errors of the laboratory EAF fitted to the measurement data.

described in Subsection related to the large industrial EAF. Namely, the first value $\alpha = 0.777$ is the median of α calculated from the results of the general case with variable α. The second $\alpha = 0.715$ is a value characterized by the lowest RMSE median among other cases investigated by sweep analysis, the results of which have

been presented in Fig. 6.18. As shown, every approach including the fractional order model results in error reduction. The general $\alpha = var$ improves accuracy the most.

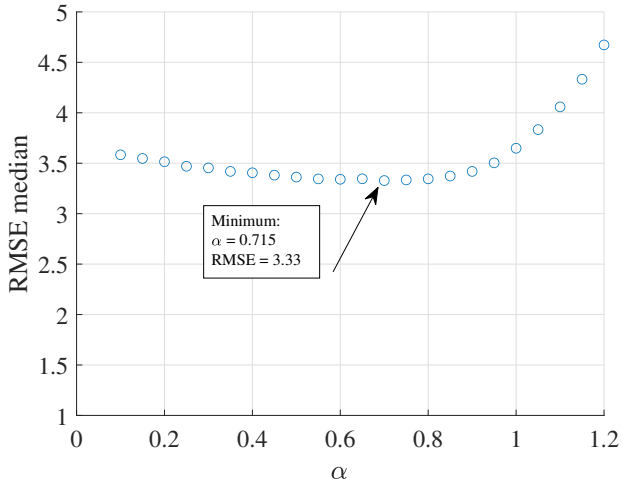

Fig. 6.18: Relationship of the error median depending on the constant value of the order α of the applied fractional differential equation for the laboratory EAF.

Chapter 7

Comparative analysis

The previous chapters have presented several different EAF models, developed based on three different measurement datasets. They are oriented toward reflecting the stochastic behavior of EAFs or improving the deterministic part of the model in the melting stage of the work cycle. The proposed approaches include the following:

- random differential equation model,
- chaotic model,
- artificial neural network models:
  - multilayer perceptron model,
  - dual multilayer perceptron model,
  - modified nonlinear autoregressive exogenous model,
  - long short-term memory model,
- fractional order model.

Every of the listed models is characterized with different properties with respect to the accuracy and range of the reflected features. Previous chapters include not only details of model development but also the exemplary results related to the model performance. This section is devoted to comparing these models in terms of their properties and accuracy measures.

In the application of the EAF modeling, it is especially difficult to objectively combine and compare models with a wide range of theoretical approaches and included features. Because of that, the first stage of the comparative analysis is the qualitative assessment of the proposed models. Information about their features has been collected in Table 7.1 below. As shown, only two of the proposed models (RDE and LSTM) are fully capable of reflecting the deterministic component and the low- and high-frequency stochastic changes in the EAF waveforms. Other approaches also have their own advantages related to, e.g. simplicity of the structure. However, the qualitative assessment is not enough to draw objective conclusions.

The next stage of the comparative analysis is related to the comparison of the exemplary realizations of the output voltage waveform performed by each of the models. The waveforms in some cases are only realizations obtained with random variables and stochastic processes. This means that they cannot be compared directly. Here, an objective measure of the waveform realizations has been proposed. Analysis is limited to the large industrial EAF installation, because due to its size

Table 7.1: Qualitative comparison of the EAF models presented in the thesis.

Model	**Det.**	**Low freq. stoch.**	**High freq. stoch.**	**Comment**
Power balance	×			Power balance equation is the base for other developed models. It only reflects the deterministic part of the EAF behavior.
RDE	×	×	×	The RDE model is the main framework for development of other models. It is based on the assumption that power balance equation k_j coefficients can be represented with stochastic processes K_j, which enables reflection of low frequency changes in the EAF model. Additionally another stochastic process can reflect high frequency stochastic variations.
Chaotic	×	×		The chaotic model applies optimized chaotic systems in order to reflect changes of the power balance equation k_j coefficients, therefore also models stochastic-like low frequency changes retaining deterministic background.
MLP	×			The MLP model is the most basic ANN model not capable of reflecting any dynamic changes or hysteresis in the EAF characteristic.
Dual MLP	×			The dual MLP model consists of a doubled MLP structure in order to allow reflection of the V-I characteristic hysteresis, although it still does not include any stochastic properties.
M-NARX	×	×		The M-NARX is a model capable of reflecting dynamic changes of the EAF characteristic and hysteresis with fairly simple structure, but does not include any more complex stochastic features.
LSTM	×	×	×	The LSTM model is the most complex among the presented ANN models. It is capable of standalone reflection of stochastic processes representing K_j and high frequency variations. Similarly to RDE it is based on the power balance equation.
Fractional order	×	×		The fractional model is oriented mainly on the improvement of the deterministic part by addition of the noninteger derivative order. The idea behind this model is similar to the RDE model with another degree of freedom available - the order of equation α. Based on that, it could reflect low frequency stochastic changes similarly to RDE.

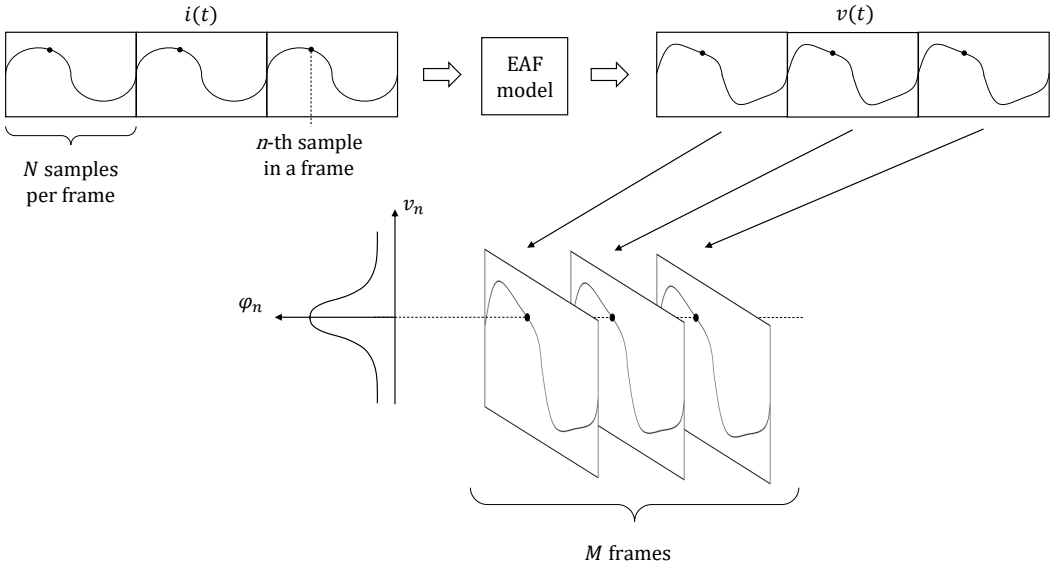

Fig. 7.1: Diagram presenting method of data preprocessing for the statistical comparative analysis.

and rated power, better modeling accuracy could have the most significant influence on the circuits considered. In order to avoid direct comparison of the voltage realizations, the 10 s long dataset has been divided into periods (related to the 50 Hz grid frequency). Then every period has been imposed onto one timeframe. A diagram presenting the way of preprocessing of calculated voltage waveforms has been shown in Fig. 7.1. For each of the n-th corresponding samples taken from every frame, a distribution ϕ_n is obtained. A set of N distributions characterizes every random variable contained in the voltage realization. The distributions ϕ_n have been calculated for measurement data as well as for every EAF model considered in this dissertation. In order to graphically present the effects of this statistical data characterization, Fig. 7.2 presents waveforms consisting of the mean value of every ϕ_n distribution obtained for the EAF models compared to that from measurement data. Additionally, plots include 95% confidence bounds of these distributions in order to show their dispersion. As shown, all shallow ANN models have a very limited ability to reflect proper variations in the shape of the voltage waveform between simulated periods. On the other hand, stochastic models, especially the RDE and fractional model, tend to overestimate those variations.

In order to provide an objective quantitative analysis of proposed solutions, for each pair of distribution ϕ_n taken from measurement data and a chosen model, a Cramér-von Mises statistic has been calculated [70]:

$$W^2(n) = CM(\phi_n^{meas}, \phi_n^{sim}), \tag{7.1}$$

where:

$W^2(n)$ – Cramér-von Mises statistic for distributions of n-th sample taken from the measurement data and selected model,
ϕ_n^{meas} – distribution of n-th sample taken from measurement data,
ϕ_n^{sim} – distribution of n-th sample taken from data simulated by the selected model.

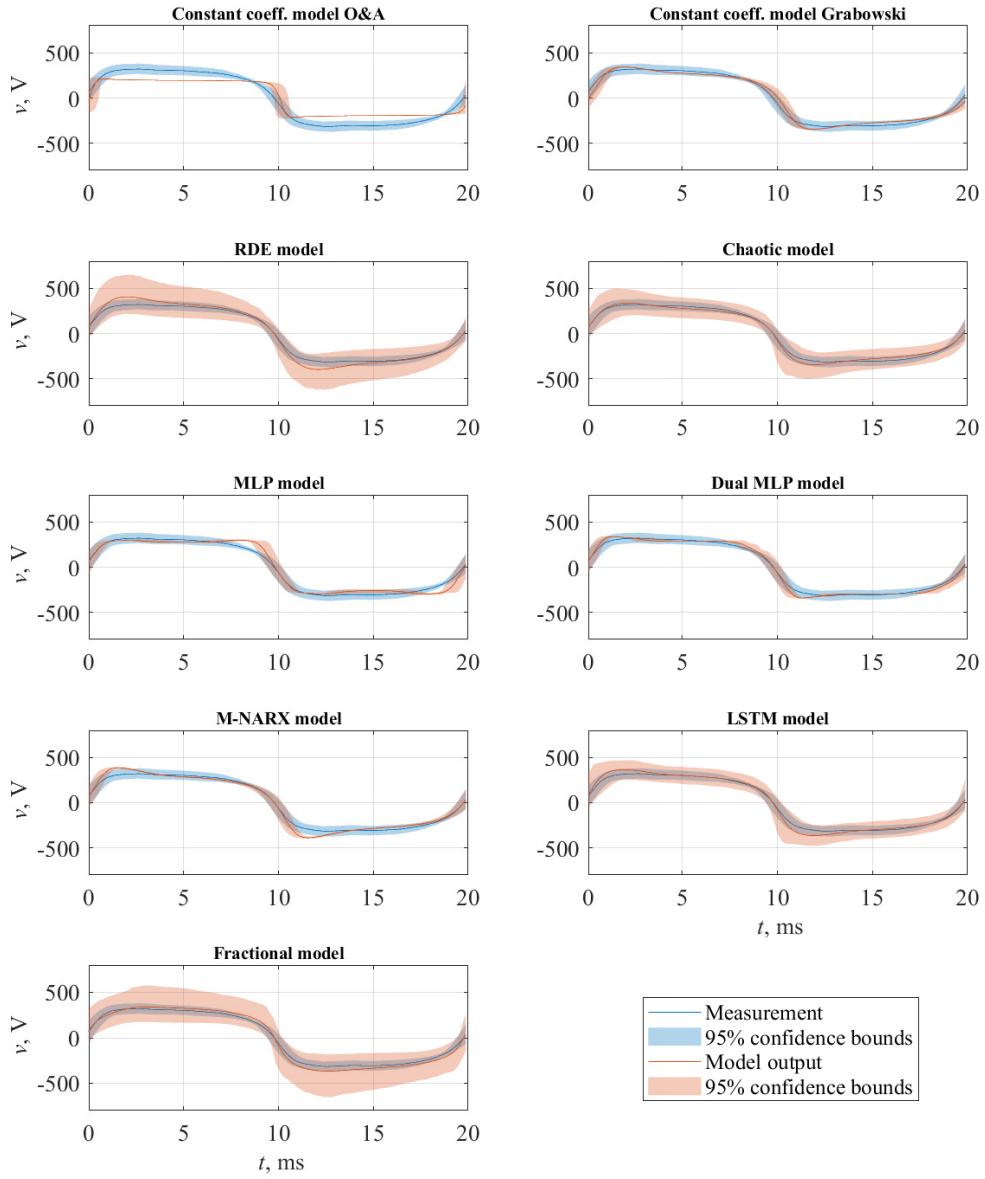

Fig. 7.2: Comparison between the averaged realizations of the output voltage of the developed models, the output of a model with constant coefficients k_j ([28] and [23]) and the measurement data.

Calculations of this measure have been repeated for each of the N samples in the frame. This way, a series of W^2 statistics has been obtained, representing quality of reflection of the modeled voltage variability with respect to the real measurement data. Those series calculated for all models developed in this dissertation have been presented in Fig. 7.3. Lower values of W^2 indicate better conformity between measurement and simulated distribution. As shown, around signal zero crossings (0, 10 and 20 ms), the conformity is the best, however this feature is reflected similarly by every model. More informative data is presented between zero crossings, indicating that the shallow ANN models and constant coefficient model proposed by Ozgun and Abur in [28] are characterized by the largest discrepancies with respect to the measurement data. A second constant coefficient model proposed by Grabowski in [23] has lower discrepancies, but is visibly worse than the remaining models proposed in this dissertation, which include stochastic properties.

In order to further analyse the previous results, a single-valued measure has been proposed as a median of W^2 statistic time sequence, calculated for every model. A bar plot with obtained values has been presented in Fig. 7.4. The results confirm previously stated dependencies. The constant coefficient model proposed by Ozgun and Abur in [28] is characterized by the worst accuracy. Next, the group of shallow ANN models and the constant coefficient model by Grabowski from [23] have better, similar accuracy. The best performing models belong to the stochastic models developed in earlier Chapters of this dissertation, i.e. RDE, chaotic, fractional, and LSTM models.

Another very important factor relevant in comparative analysis is the computational power required for the development and usage of the models. It is especially important from the point of view of target simulation software, which can have limited resources or available libraries. Furthermore, industrial applications, especially embedded solutions, are even more dependent on these parameters. Due to this, the models proposed in this thesis have been subjected to an analysis of the computational resources required. The first parameter investigated was the size of the model in software memory, which is proportional to the complexity of the model structure and the size of the auxiliary variables or functions required for its functionality. What is important is the fact that the calculated memory usage included all the additional variables related to the development of the models, including, target datasets for ANN models or auxiliary variables obtained through the data pre-processing stages. The second important parameter is related to the computation time. Because, for some models, their parameters change between consecutive periods, some calculations are performed only with an interval of those periods, while the others are needed at each timestep. The time estimated here is the CPU time elapsed during generation of a 10 s long output voltage waveform, divided by the number of obtained samples. In this way, the final value is the average time spent on the computation of a single output voltage sample, regardless of the simulation stage. All models have been designed and evaluated in Matlab software, and the computing infrastructure included a portable computer with an Intel Core i7 processor (4 cores, 1.8 GHz), 16 GB RAM, and the Windows 10 operating system. Some of the calculations related to the development stage, especially for the purpose of optimization of the model structure, have been computed by the high-performance computing infrastructure PLGrid (HPC Centers: ACK Cyfronet AGH), however, the comparison of computation time has been done using only data

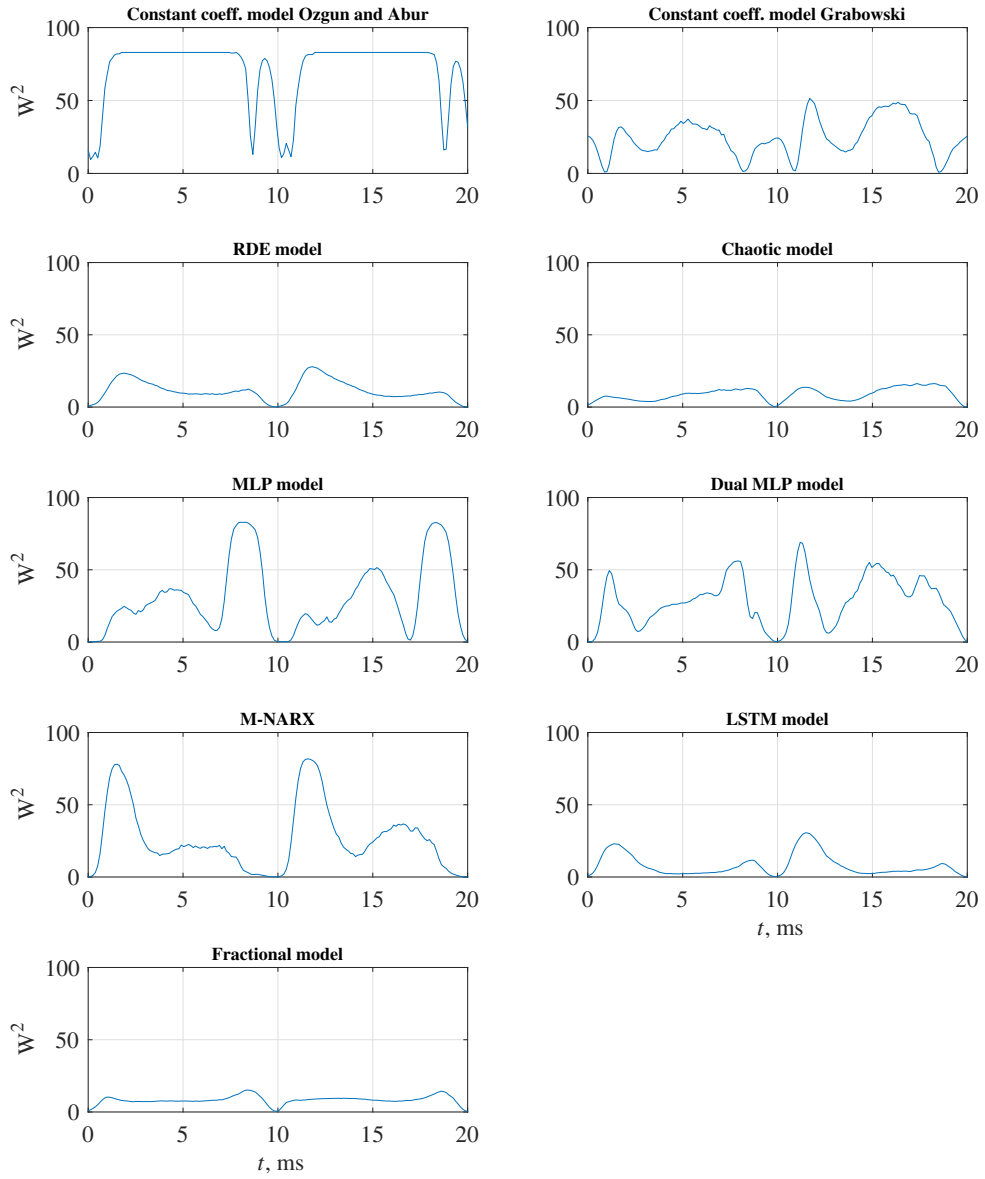

Fig. 7.3: Time series of Cramér-von Mises statistic illustrating divergence between distributions of samples taken from measurement data and a given model.

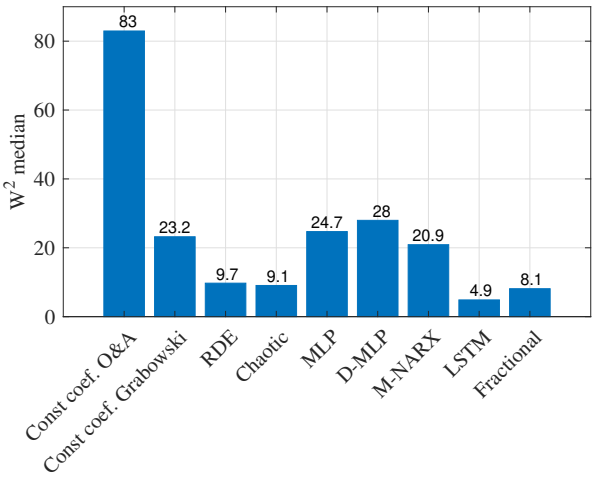

Fig. 7.4: Bar plot comparing median of W^2 statistics obtained for all considered EAF models.

from the aforementioned portable computer. The results have been presented in Fig. 7.5. As shown, the fractional, RDE and MLP models significantly outperform the others in terms of both computation time and used memory. The highest memory usage characterizes the M-NARX model because of additional preprocessing stages, recalculation of the arc's conductance, and filtering of the outliers. The longest computational time of the dual MLP model seems counterintuitive, but is related to the need to check the criterion of the current derivative, whether to use the first or the second MLP model. The best overall model is the RDE model.

On the basis of all the results provided in this Chapter, a selection of the suitable model for further implementation has been made. The goal of this research is to equip electrical engineers around the world with a tool to simulate EAFs, with the ability to reflect the stochastic phenomena that occur in power systems with such loads. The simulation tool that has been chosen for this purpose is the EMTP-ATP program, which is a very popular software for circuit simulation. It is often used for research purposes, as well as for direct industrial applications. However, the software has limitations. The main idea of this research was not only to develop the EAF model, but also to implement it directly into the target software so potential users would not have to install additional libraries, components, and establish new dynamic links or connections with other external software. Taking this into account, the three main aspects of the comparative analysis have been considered:

- capability of reflecting the stochastic phenomena,
- model accuracy,
- required computational power and required resources.

In case of the first aspect (see Table 7.1), the whole spectrum of both low frequency and high frequency stochastic changes is reflected only by the LSTM and RDE models. For model accuracy, the RDE, LSTM, fractional and chaotic models are leading. Furthermore, the simple incorporation of the variable coefficients k_j leads to an improvement in the representation of the voltage waveform by almost 30% (see Table 3.1). Lastly, in terms of computational resources, the best models are

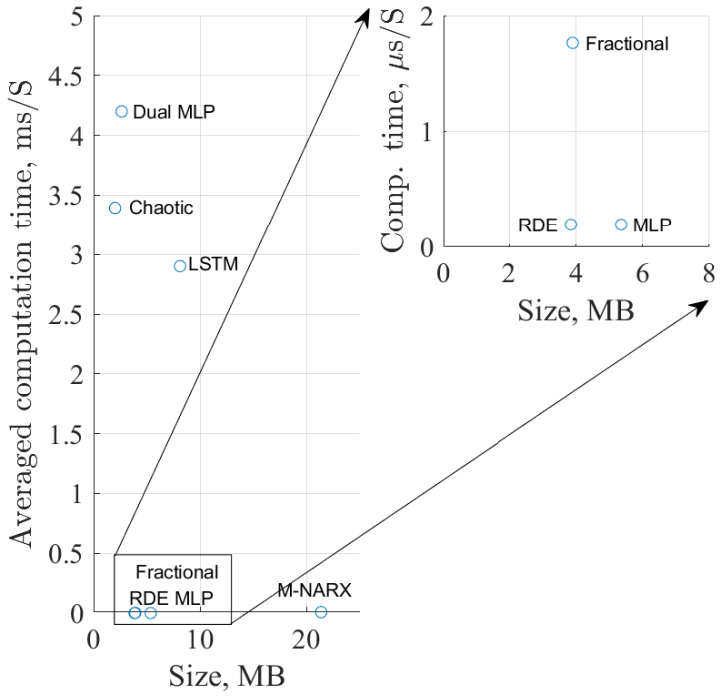

Fig. 7.5: Comparison between the average computation time and memory used for the development and use of the proposed models.

fractional RDE and MLP. Based on the information above, the factor by which the RDE model outperforms others in terms of computational power, including stochastic features and relatively good accuracy, as well as structural simplicity, results in the conclusion that it is the one which should be implemented in the EMTP-ATP simulation software. The details of the implementation procedure and its results are presented in the next Chapter.

Chapter 8

ETMP-ATP EAF model

This Chapter is devoted to the implementation of the RDE model of the EAF selected based on the analysis presented in Chapter 7. The target software was selected to be ETMP-ATP, which is a world-known and very popular program for the simulation of electrical circuits. Among the advantages related to the application of this software is its flexibility to model circuits, starting from small topologies all the way up to large power systems. Additionally, this program's version is free-licensed, which makes it available to anyone interested. Although not commercial, several groups of users exist which contribute to the further development of software, share knowledge, and provide support (e.g. the European EMTP-ATP Users Group). This program is used by various companies and institutions and is often applied not only for industrial purposes but also for scientific research. On the other hand, the software also has limitations, especially related to the components available in the libraries and capabilities of add-ons extending the properties of existing elements. Fortunately, the program has been equipped with a component where the user can add a code that performs all the previously assumed features. The language applied in this software is called MODELS language and provides functionalities similar to other popular high-level programming languages [71], [72]. In this way, the model introduced in this thesis, initially developed as a Matlab code, can be translated and implemented in the EMTP-ATP software. The approach presented in this Chapter has been the subject of a conference publication that was presented during the European EMTP-ATP Users Group meeting [45]. Details of the implementation have been provided in the following sections.

8.1 Implementation of the RDE model

The selected EAF model has been implemented in the EMTP-ATP software following a definition provided in Chapter 3. Similarly, the model implemented consists of three main structural blocks, the deterministic part, low frequency stochastic changes and a high frequency addition. Arc resistance was represented with a non-linear resistor, whose value would change at each solver step. It follows the governing equations coded in the MODELS language. These assumptions impose the need to implement the equations of Chapter 3 in such a way that the resistance to the arc would be their output variable.

For the purpose of RDE model implementation, the same auxiliary variable y as introduced in Chapter 6 has been used. In this way, the deterministic part would

be reflected directly in the EMTP-ATP software by solving the following differential equation:

$$\frac{\mathrm{d}y(t)}{\mathrm{d}t} = -\beta y(t) + f(t). \tag{8.1}$$

However, the overall model output should be the arc resistance, which in this case is only the deterministic component of the arc resistance, denoted as R_p, since it originates from the power balance equation:

$$R_p(t) = \frac{k_3}{\sqrt{y(t)}}, \quad y(t) \geq 0. \tag{8.2}$$

The above deterministic part is supplied with k_j coefficients that change from period to period, which consist of the low frequency stochastic part. The exact changes are calculated on the basis of the discrete-time stochastic processes representing the auxiliary $\hat{k}_j$ coefficients, as identified in the previous chapters.

To independently generate those values in a model, the identified stochastic processes had to be implemented in the MODELS language. The language is flexible and convenient for the user, but the entire implementation had to rely only on the built-in random number generator, which generates a random number from the uniform distribution $U(0,1)$. The rest of the stochastic properties had to be implemented by the user manually.

8.1.1 Representation of $\hat{K}_1$

The stochastic process representing changes in coefficient $\hat{k}_1$ has been identified as the ARIMA(1,1,2) process with residuals following a hyperbolic secant distribution and a shift - see Chapter 3. Moreover, the distribution was reshaped with a Box-Cox transformation [53]. Here, the ARIMA process was implemented as follows [51]:

$$Y_t = Y_{t-1} + AR_1(Y_{t-1} - Y_{t-2}) + \epsilon_t + \epsilon_{t-1}MA_1 + \epsilon_{t-2}MA_2, \tag{8.3}$$

where:

Y_t – ARIMA sample in discrete timestep t,
AR_1 – autoregressive component coefficient,
MA_1, MA_2 – moving average component coefficients,
ϵ_t – innovations following a hyperbolic secant distribution in timestep t.

Innovations ϵ following hyperbolic secant distributions have been generated using an inversion method. In this way, a random number p from the universe distribution $U(0,1)$ is applied as an argument for the inverse CDF of the hyperbolic secant distribution. The output variable then follows this exact distribution [52]. That is,

$$\epsilon_t = \mu_\epsilon + \frac{2\sigma_\epsilon}{\pi} \ln\left(\tan\left(\frac{\pi}{2}p_t\right)\right), \tag{8.4}$$

where:

μ_ϵ – mean of the hyperbolic secant distribution,
σ_ϵ – standard deviation of the hyperbolic secant distribution,
p_t – random value of the uniform distribution $U(0,1)$ at time t.

Eventually, the value of $\hat{k}_1$ can be calculated using the reverse Box-Cox transformation:

$$\hat{k}_{1,t} = (\lambda Y_t + 1)^{\frac{1}{\lambda}}, \tag{8.5}$$

where:

λ – Box-Cox transformation parameter.

8.1.2 Representation of $\hat{K}_2$

The second stochastic process that has been identified in the EAF model in Chapter 3 was the one that represents the changes of $\hat{k}_2$. It was a white noise process with a mixed shifted Weibull distribution with two components. The effect of the combination of two different components was achieved with the auxiliary random variable p_s of uniform distribution $U(0,1)$, which was used as a decision variable. Drawing a value below a certain threshold leads to generation of a random value from one Weibull component, while a value above the threshold leads to generation of a random value from the second Weibull component. The threshold value reflected the probability of choosing the first component. The Weibull distribution itself was again implemented using the inverse CDF method, namely:

$$\hat{k}_{2,t} = \begin{cases} \mu_W + a_1(\ln(1-p))^{\frac{1}{b_1}} & \text{for } p_s \leq p_{thr}, \\ \mu_W + a_2(\ln(1-p))^{\frac{1}{b_2}} & \text{for } p_s > p_{thr}, \end{cases} \tag{8.6}$$

where:

μ_W – Weibull distribution shift,
a_1, b_1 – shape coefficients of the first Weibull component,
a_2, b_2 – shape coefficients of the second Weibull component,
p – random variable from uniform distribution $U(0,1)$,
p_s – random variable from uniform distribution $U(0,1)$ used for selection of the Weibull distribution component,
p_{thr} – threshold value representing probability of selecting the first Weibull component, then probability of selecting the second is equal to $1-p$.

The last step before solving the actual differential equation is to supply it with the original three coefficients k_j. It is done by applying the constant mean value of k_3 calculated from the measurement data and coming back to the original coefficients of the coefficients $\hat{k}_j$, using:

$$k_1 = \frac{k_3}{\hat{k}_1},\ k_2 = \frac{k_3 \hat{k}_1}{\hat{k}_2}. \tag{8.7}$$

8.1.3 Representation of the high frequency component

As stated previously in Chapter 3, the high frequency component can be represented with a moving average stochastic process with four components. The process itself can be described with the following equation:

$$V_{r,t} = \epsilon_{r,t} + \epsilon_{r,t-1} MA_{r1} + \epsilon_{r,t-2} MA_{r2} + \epsilon_{r,t-3} MA_{r3} + \epsilon_{r,t-4} MA_{r4}, \tag{8.8}$$

where:

$V_{r,t}$ – high frequency component voltage sample in a discrete timestep t,
MA – moving average coefficients,
$\epsilon_{r,t}$ – innovation in timestep t.

The innovations in this particular process follow a normal distribution and have been generated using the Box-Muller method, which applies two independent random variables from a uniform distribution $U(0,1)$ [52]. The equation takes the following form:

$$\epsilon_{r,t} = MA_{var}\sqrt{-2\ln(u_1)}\cos(2\pi u_2), \tag{8.9}$$

where:

$\epsilon_{r,t}$ – innovation with normal distribution in discrete timestep t,
MA_{var} – scale coefficient for generated innovations,
u_1, u_2 – uniformly distributed random values from $U(0,1)$.

These equations allow for calculation of the high frequency component voltage. However, the model implemented in EMTP-ATP requires information about the arc resistance value. This results in the necessity of transformation of the high frequency voltage component into a component with resistive character. An EAF is a nonlinear object, however this component is implemented assuming a linearization at the operating point at given t. Thus, the resistance calculated from the differential equation and the high frequency resistive component are simply summed. The resistance related to the high frequency component can then be calculated as:

$$R_{r,t} = \frac{V_{r,t}}{i_{arc,t}}, \tag{8.10}$$

where:

$R_{r,t}$ – high frequency resistance component at timestep t,
$i_{arc,t}$ – arc current at timestep t.

The global EMTP-ATP solver timestep can often be too small for the high frequency component to be generated each time. This could cause inaccuracies in the final results. As shown in previous research related to the high frequency component [39], a suitable sampling time is equal to $\Delta t_r = 1.25 \cdot 10^{-4}$ s. To ensure that, for different ATP solver timesteps, the correct results are obtained, an additional procedure has been introduced. The main idea is to provide the appropriate intermediate steps of $R_{r,t}$ between the larger ATP timesteps. Fig. 8.1 presents the relationship between consecutive time steps of the ATP solver with regard to Δt_r. The graph also presents how voltage samples are calculated between two consecutive Δt_r steps, based on the linear approximation. Firstly, a simplified derivative of high frequency component voltage is calculated using:

$$dV_{r,t} = \frac{V_{r,t} - V_{r,t-1}}{\Delta t_r}, \tag{8.11}$$

where:

Δt_r – fixed timestep of the high frequency component,

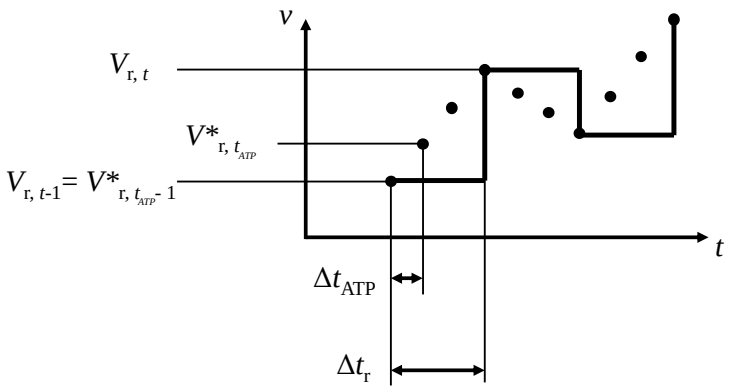

Fig. 8.1: Graphical explanation of the intermediate calculation of the high frequency voltage component in EMTP-ATP.

Next, for each ATP timestep the currently used value of $V_{r,t}$ is corrected by adding a component equal to the product of derivative $dV_{r,t}$ and the current ATP timestep:

$$V^*_{r,t_{ATP}} = V^*_{r,t_{ATP}-1} + dV_{r,t}\Delta t_{ATP}. \tag{8.12}$$

The value computed from the above equation is then used to calculate the corrected high frequency resistance component. The last step is to sum both components, which results in the following relationship.

$$R_{arc}(t) = R_p(t) + R_r(t) = R_p(t) + \frac{V^*_r(t)}{i_{arc}(t)}, \tag{8.13}$$

where:

$R_{arc}(t)$ – overall resistance of the arc at time t,
$R_p(t)$ – component of the resistance of the arc originating from the power balance equation (both deterministic and low frequency stochastic components at time t),
$R_r(t)$ – resistance of high frequency stochastic components at time t.

For a complete model including the stochastic components mentioned above, the resistance $R_{arc}(t)$ is a realization of a stochastic process describing the resistance of the arc.

The numerical stability of such a model could be disrupted by changes of high frequency components in the area near the origin of V-I characteristic coordinate system. To ensure its stability, an additional weighting factor has been applied. It consists of a multiplicative variable that reduces the value of the R_r component around the current zero crossing. The level of such a reduction can be adapted by adjusting the value of the current threshold I_{thr}. The whole expression for the arc resistance with the weighting factor is as follows:

$$R_{arc}(t) = R_p(t) + R_r(t)\tanh(I_{thr}|i_{arc}(t)|). \tag{8.14}$$

8.2 Simulation results and analysis

All of the equations presented in the previous section have been implemented directly in the MODELS language in the code governing the appropriate nonlinear resistor. In EMTP-ATP it is a nonlinear resistor with resistance controlled externally, e.g. by code calculated at each timestep. The results provided in the following subsections arise from the calculation of the expected resistance computed by the MODELS language solver. For the purpose of performance analysis, the output arc voltage has been presented instead of the resistance itself, based on the following equation:

$$\tilde{v}_{arc}(t) = R_{arc}(t) i_{arc}(t), \tag{8.15}$$

where:

$\tilde{v}_{arc}(t)$ – estimated arc voltage,
$R_{arc}(t)$ – arc resistance calculated using MODELS code,
$t_{arc}(t)$ – arc branch current measured by the built-in EMTP-ATP component.

8.2.1 Single-phase model

The single-phase model directly reflects the equations describing the arc model because the power balance approach itself is designed to reflect the behavior of a single arc. In the EMTP-ATP software, a simple test circuit has been designed. It consists of a voltage source, resistance, and inductance that simulate the influence of busbars, flexible cables, and the arc model. The arc model itself consists of three crucial elements: a current-measuring component, a general MODELS block, which takes the current measurement as an input and computes desired arc resistance as output, and finally the nonlinear resistor controlled by the MODELS block output. The single-phase model topology has been presented in Fig. 8.2. As can be noticed, there is an additional resistor between the nonlinear resistor node and the ground. It is related to the simplifying assumptions that the single phase arc can exist independently from the remaining EAF phases [1], which would contribute to the overall resistance through which the current would flow.

It was assumed that R and L in the source branch had values: 0.33 mΩ and 7.18μH as in the primary dataset for the large industrial EAF. The parameters of the voltage source are 718 V RMS and 50 Hz. Figs. 8.3-8.5 present a set of exemplary results generated by the model with only a deterministic part, deterministic and global stochastic, and deterministic and both stochastic parts, respectively.

8.2.2 Three-phase model

The single-phase model presented in the previous subsection can be directly used for the development of a three-phase version. In that case, the model structure has to be tripled for each branch to model each of the three arc columns. The branches, of course, have a common coupling point in the node that represents the melting load. The parameters of the flexible cables have also been duplicated. The whole

[1] This assumption has been made in order to allow analysis of a single phase of the EAF circuit. However, in a real three phase device, where transformer secondary windings are connected in delta configuration, a single phase arc cannot exist.

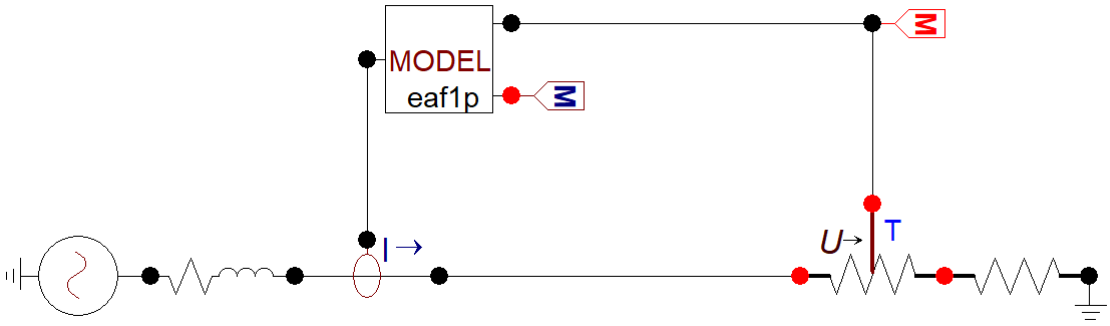

Fig. 8.2: Single phase EAF circuit constructed in EMTP-ATP.

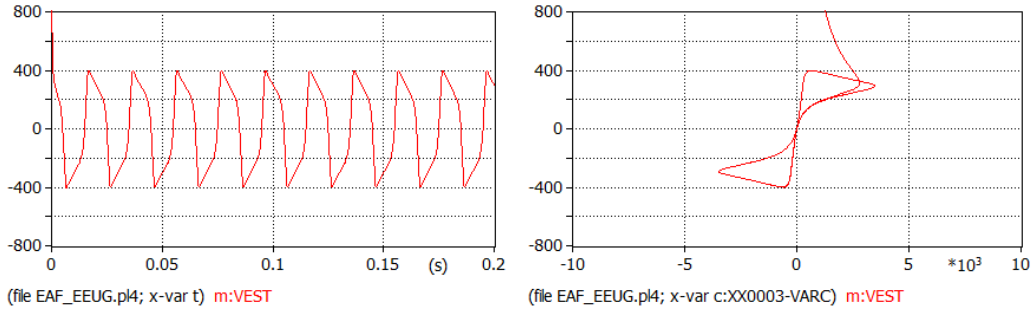

Fig. 8.3: Voltage and V-I characteristic of the deterministic part of the model implemented in EMTP-ATP.

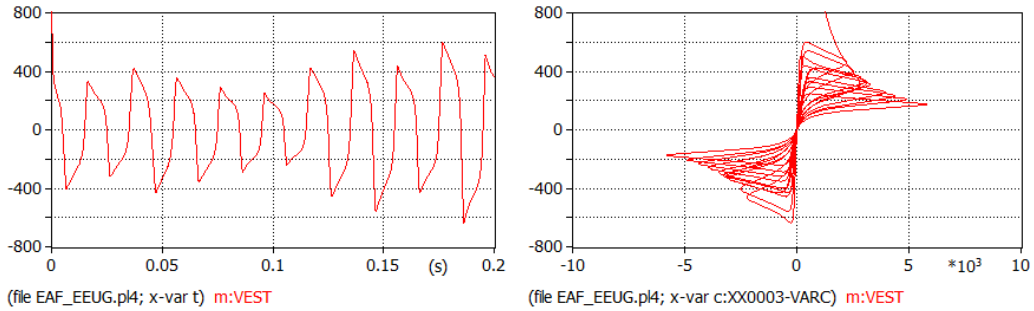

Fig. 8.4: Voltage and V-I characteristic of the deterministic and low frequency stochastic component of the model implemented in EMTP-ATP.

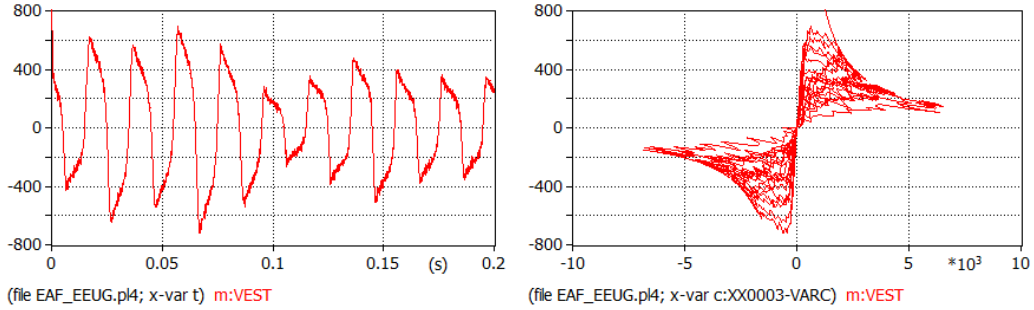

Fig. 8.5: Voltage and V-I characteristics of the deterministic stochastic components, both low- and high-frequency, of the model implemented in EMTP-ATP.

test circuit has been shown in Fig. 8.6. The results containing the estimated arc voltage, as well as the measured current and V-I characteristic in each phase, have been presented in Figs. 8.7 and 8.8.

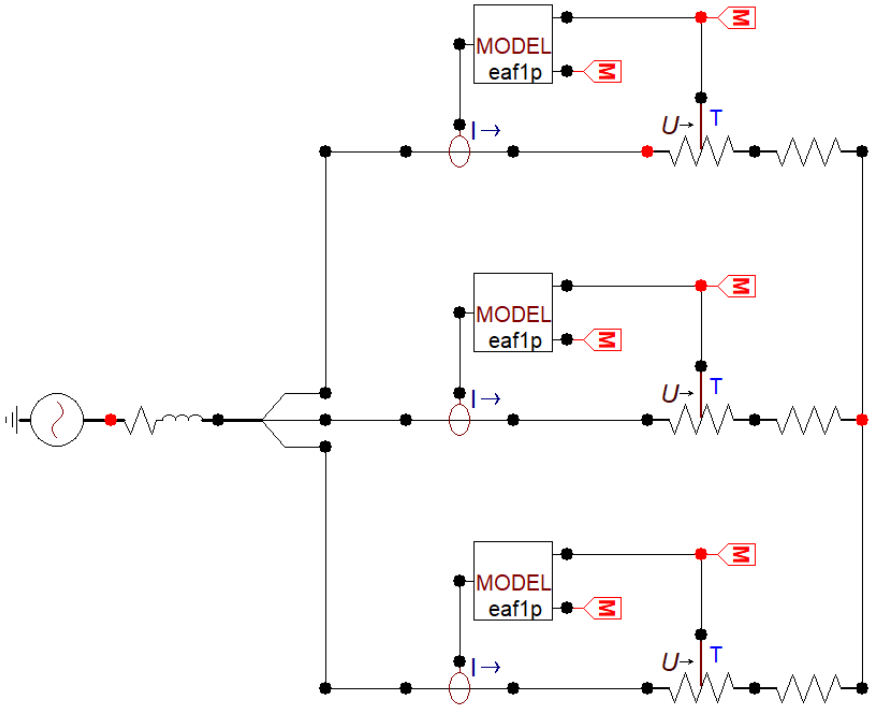

Fig. 8.6: Three-phase EAF model constructed in EMTP-ATP.

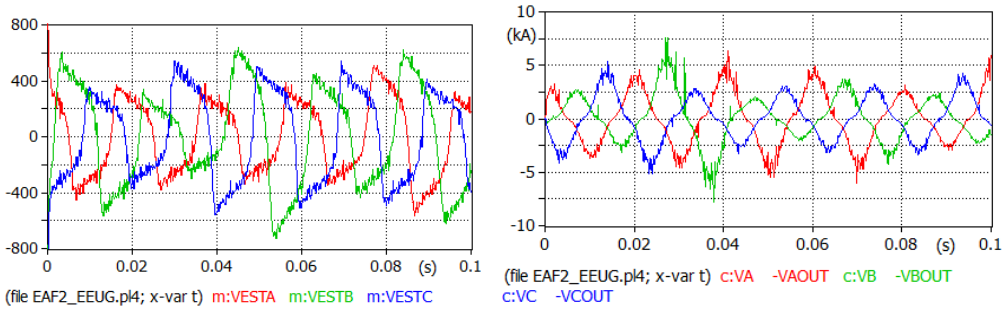

Fig. 8.7: Output voltage (left graph) and measured current (right graph) of the three-phase EAF model implemented in EMTP-ATP.

8.2.3 Model validation

The performance of the arc model implemented in EMTP-ATP software has been validated using a single phase model. Comparison of the resistance calculated by the MODELS code with the resistance of the nonlinear resistor presented in Fig. 8.2 calculated based on the ATP measurement variables indicated its consistency. The graphical representation of this comparison has been shown in Fig. 8.9. For the sake of clarity, the high frequency component has been disabled leaving only the

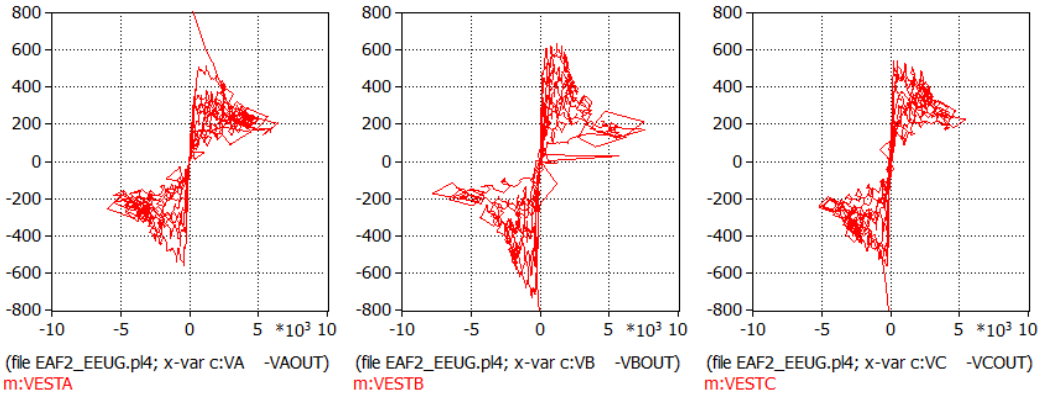

Fig. 8.8: V-I characteristics for each of the phases of the three-phase EAF model implemented in EMTP-ATP.

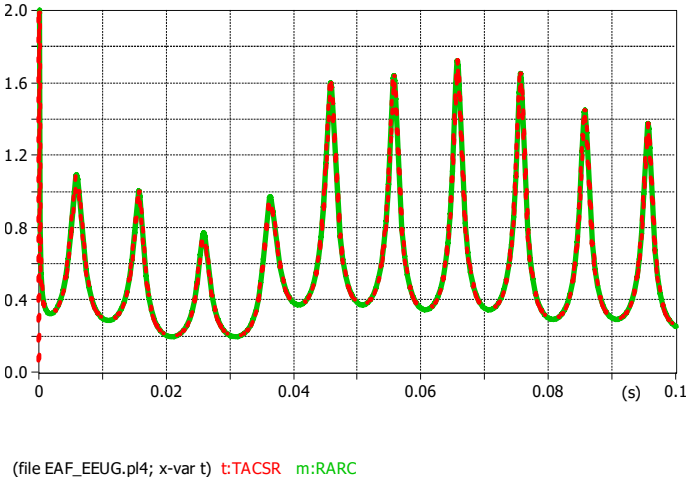

Fig. 8.9: Arc resistance calculated by MODELS block (green line) compared to arc resistance calculated on the basis of the EMTP-ATP results (red line).

low frequency component active. The plot presents stochastic realization of arc resistance in a single phase model.

The entire ATP code of the single phase model has been placed in the Appendix in order to provide the details leading to the implementation of the proposed EAF model in the EMTP-ATP software.

Chapter 9

Conclusions

EAFs are often listed as one of the most disturbing loads in electrical engineering. Their random and unpredictable behavior, along with the strongly nonlinear characteristic of the arc phenomenon, results in their significant influence on power systems and power quality. Moreover, a large proportion of the worldwide steel production use EAFs, so the consequences of their use are far from negligible. As previously stated in the Introduction, many industrial applications, from the design stage of facilities, through operation, to the design or control of power quality improvement systems, require an accurate model of the phenomena occurring in the EAFs. Simplified, deterministic-only models are not capable of reflecting some stochastic phenomena that are observable in real installations. This thesis has presented the development of several new EAF models, especially oriented toward the possibilities of the incorporation of stochastic behavior into those models. Various theoretical approaches have been investigated. The research included the development of the models based on three different, real EAF measurement datasets, investigation of the numerical results, and multi-aspect comparison. A single model selected by means of the comparative analysis has been implemented directly in the time domain simulation software: EMTP-ATP. The code of the EAF model implemented using dedicated MODELS language has been presented in the thesis Appendix, making it available to all the interested parties.

The research presented in this thesis is fully supported by real measurement data. All of the proposed approaches have been tested by applying them to calculations based on three different measurement datasets. These datasets consisted of single phase current and voltage measured in differently sized EAFs. The first was a large industrial furnace, the second a smaller industrial furnace, while the last was the smallest, laboratory scale furnace. For every dataset, the point of interest was the melting stage of the EAF work cycle. This was related to the fact that while the furnace's load is still not liquid, the arc can behave the most randomly and its characteristic is highly nonlinear. This results in the worst impact on the power quality of the power system among all the remaining stages. The small industrial EAF and laboratory version measurements have been personally carried out by the author for the purpose of this analysis. In addition, a laboratory station has been constructed, especially for comparative analysis with industrial furnaces during doctoral research.

All of the proposed methodologies are based on a well-known model of electric arc power balance. The model is suitable for the simulation of behavior of a single

arc. Instantaneous power balance with definitions based on the arc current and arc column radius are combined into this differential equation. Each of the equation expressions has its own proportionality coefficient. In this thesis, the first proposed model assumes a representation of those coefficients (which often are considered constant) with stochastic processes instead of their constant values. Due to this, the error RMSE between the voltage calculated from the RDE model and the measurement data has decreased compared to the error based on the voltage calculated with constant coefficients. The error was reduced by approximately 30%, 40% and 70% for a large industrial furnace, a small industrial furnace, and a laboratory furnace, respectively. The RDE model introduced in Chapter 3 includes a detailed identification of the stochastic processes based on the realizations estimated from the measurement data.

The next covered model relies similarly on the coefficients of the power balance equation variable in time. In this case, however, their changes have been appropriately represented with optimized chaotic signals. As chaotic systems are relatively popular in various scientific branches, in this Chapter, four different systems have been compared: Chua, Lorenz, Rössler and four-wing attractor systems. The best results of the EAF modeling have been obtained for the combination of the Lorenz and four-wing attractor system.

Another way to model EAFs is by applying ANNs. This thesis includes the development of several different ANN models based on shallow and deep learning networks. Among shallow models, very simple MLP and dual MLP have been introduced, but they are not capable of reflecting any stochastic changes of the EAF characteristic. The only shallow model that included dynamic changes was the M-NARX model. The application of deep learning methods with LSTM networks has been required to accurately model stochastic changes in the wide frequency spectrum.

The last proposed model has been focused on improving the deterministic part of the power balance equation by introducing a novel fractional order operator into it. The addition of another degree of freedom allowed a better reflection of the EAF characteristic. What is interesting is that the best results have been obtained on the order of approximately 0.6, 1.2 and 0.8 for large industrial, small industrial, and laboratory furnaces, respectively. These results suggest that the size of the EAF influences the value of α.

All of the proposed approaches have been compared using the data averaged throughout 10 s long waveforms in order to avoid errors of direct comparison of realizations of stochastic processes. The computational resources needed for the development and operation of each model have also been analyzed. Additionally, the qualitative assessment has been done, emphasizing the range of features which a given model can reflect in comparison to real observable phenomena. The level of accuracy of the models is strongly related to the fact that, although large, the datasets are still limited. The amount of information is enough for the development and accurate application of the models, however it does not cover every possible scenario. The proposed models are limited to the representation of the melting stage only. On the basis of the possible power quality issues, this stage is of the main interest for the simulation, but it is necessary to note that other stages are not covered. Furthermore, the proposed models assume that the coefficients k_j are not correlated with each other. In reality, such a correlation exists. Therefore, future

research following this thesis should first focus on investigating this effect. The application of all of the proposed methodologies to measurement data originating from differently sized furnaces proves their versatility. Although the range of results obtained differs, the same features occur in all sets of results. As a consequence, the same methods can be applied to accurately model installations of different sizes.

The proposed solutions consist of data driven models, which have been developed on the basis of three selected real installations. It is important to mention that although all of the presented approaches resulted in an accurate reflection of the modeled object, these models are not universally parameterized in the sense of scalability to other, not investigated furnaces. The analysis indicated that different furnaces exhibit similar stochastic features, but further research should focus on the analysis of possible universal scalability rules applicable to developed solutions. Determining such rules would allow modeling of any given EAF based on the proposed approaches. However, such an extended investigation would require many more measurement datasets and access to different EAFs. The most informative set of measurement waveforms would have to include not only datasets from differently sized furnaces, but also multiple datasets from installations with comparable rated power. Moreover, even in one particular EAF, different smelting processes can be characterized by slightly different features due to the influence of melted metal.

Based on the comparative analysis conducted, drawing conclusions from various aspects of the performance of the models, the RDE model has been selected as the most suitable for implementation in the EMTP-ATP software. Appropriate numerical methods developed in the dedicated MODELS language allowed direct implementation of the stochastic processes and differential equation governing this model. The exact nature of the model was a nonlinear controlled resistor, the resistance of which is provided by the computation of implemented code, based on the measured branch current. The calculations are carried out repeatedly for each timestep, updating the resistance value each time. The calculations themselves accurately reflect not only the deterministic component, but also low- and high-frequency stochastic variations of the EAF characteristic. The code has been presented in the Appendix, in order to make it freely available to anyone interested in modeling the circuits with EAFs.

Among the most significant original achievements of this thesis are:

- introduction of the variable coefficients k_j reflecting the stochastic changes of the EAF characteristic, resulting in significant accuracy improvement, instead of implementing a new random variable without a physical interpretation,
- application of an optimization of chaotic systems in terms of their parameters and sampling frequency to the measurement data to reflect the stochastic changes of the power balance equation,
- development of a novel M-NARX and LSTM models of EAF, which allow reflection of dynamic changes or whole stochastic features, respectively,
- improvement of the deterministic component of the arc model by novel introduction of the fractional order differentiation into the ordinary differential power balance equation,
- multi-aspect comparative analysis of all of the proposed approaches resulting in selection and implementation of the RDE model into the circuit simulation software used worldwide - EMTP-ATP,

- design and construction of the laboratory stand for measurements and analysis of electric arc phenomenon.

Taking into account all the above points, it can be concluded that the aims of this thesis presented in the Introduction have been reached and the stated hypotheses can be considered as positively verified.

Chapter 10

Appendix - EMTP-ATP code

```
BEGIN NEW DATA CASE
C ------------------------------------------------------------
C Generated by ATPDRAW styczen, poniedzialek 30, 2023
C A Bonneville Power Administration program
C by H. K. Hoidalen at SEfAS/NTNU - NORWAY 1994-2016
C ------------------------------------------------------------
C dT >< Tmax >< Xopt >< Copt ><Epsiln>
   1.E-6 .1 60. 60. 1.E-12
     500 1 1 1 1 0 0 1 0

C Proposed single-phase EAF model based on random differential equation

/MODELS
MODEL EAF1p

-- Default variables implemented in the EAF model

DATA global {dflt:0}
     local {dflt:0}
     k3 {dflt:31.6300}
     lambda {dflt:-0.1113}
     AR1 {dflt:0.7627}
     MA1 {dflt:-0.8135}
     MA2 {dflt:-0.1556}
     mu_ARIMA {dflt:-7.8668}
     mu_eps {dflt:-0.0002}
     sigma_eps {dflt:0.2918}
     p_thr {dflt:0.7651}
     a1 {dflt:0.0079}
     b1 {dflt:1.2780}
     a2 {dflt:0.0301}
     b2 {dflt:3.2092}
     mu_W {dflt:0.0033}
     MAr1 {dflt:-0.4170}
     MAr2 {dflt:-0.5210}
     MAr3 {dflt:-0.1400}
     MAr4 {dflt:0.0860}
     MA_var {dflt:14.2370}
     dt_r {dflt:1.25e-4}
     I_thr {dflt:0.01}

INPUT Iarc
```

```
OUTPUT Rall, Varc_est

VAR Rall
    y
    Iarc2
    k1_hat, k2_hat
    k1, k2
    Yt[1..3], eps[1..3], Yt_s
    p
    Varc_est
    v_r[1..2], epsr[1..5], t_r, u1, u2, dv_r, v_r_star

HISTORY
  y {dflt:1}
  Iarc2 {dflt:0}
  Rall {dflt:1e8}

INIT
  Rall:=1e8
  Yt[1..2]:=0
  eps[1..2]:=0
  k1:=2523.8
  k2:=9.22
  k1_hat:=0.0037
  k2_hat:=0.0125
  epsr[1..5]:=0
  t_r:=0
  v_r[1..2]:=0
  dv_r:=0
  v_r_star:=0
ENDINIT

EXEC

-- Part of code responsible for calculation of arc resistance including the
    ↪ stochastic components

IF global=1 THEN
  IF prevval(Iarc)*Iarc<=0 AND prevval(Iarc)<0 THEN

    eps[3]:=mu_eps+(sigma_eps*2/pi)*ln(tan((pi/2)*random()))

    Yt[3]:=Yt[2]+AR1*(Yt[2]-Yt[1])+MA1*eps[2]+MA2*eps[1]+eps[3]
    Yt_s:=Yt[3]+mu_ARIMA
    k1_hat:=(lambda*Yt_s+1)**(1/lambda)

    eps[1]:=eps[2]
    eps[2]:=eps[3]
    Yt[1]:=Yt[2]
    Yt[2]:=Yt[3]


    p:=random()
    IF p<=p_thr THEN
      k2_hat:=a1*(-ln(1-random()))**(1/b1)
    ELSE
      k2_hat:=a2*(-ln(1-random()))**(1/b2)
```

```
    ENDIF
    k2_hat:=k2_hat+mu_W

    k1:=k3/k2_hat
    k2:=k3*k1_hat/k2_hat
  ENDIF
ENDIF

  t_r:=t_r+timestep
  IF t_r>=dt_r THEN
    t_r:=0

    u1:=random()
    u2:=random()
    epsr[5]:=MA_var*sqrt(-2*ln(u1))*cos(2*pi*u2)

    v_r[2]:=epsr[5]+epsr[4]*MAr1+epsr[3]*MAr2+epsr[2]*MAr3+epsr[1]*MAr4
    dv_r:=(v_r[2]-v_r[1])/dt_r
    v_r_star:=v_r[1]

    v_r[1]:=v_r[2]

    epsr[1]:=epsr[2]
    epsr[2]:=epsr[3]
    epsr[3]:=epsr[4]
    epsr[4]:=epsr[5]
  ENDIF
  v_r_star:=v_r_star+dv_r*timestep

  Iarc2:=Iarc*Iarc
  LAPLACE(y/Iarc2):=((4*k3/k2)|)/((4*k1/k2)| + 1.0|s)

IF local=1 THEN
  Rall:=k3*recip(sqrt(y))+((v_r_star)/Iarc)*tanh(I_thr*abs(Iarc))
ELSE
  Rall:=k3*recip(sqrt(y))
ENDIF

  Varc_est:=Rall*Iarc

ENDEXEC
ENDMODEL

-- Usage of the EAF model in ATP circuit

USE EAF1p AS DEFAULT
INPUT
  Iarc:= MM0001
DATA
  global:= 1.
  local:= 0.0
  k3:= 31.63
  lambda:= -0.11134
  AR1:= 0.7627
  MA1:= -0.8135
  MA2:= -0.1556
  C:= -7.86682
  mu:= -1.81E-4
```

```
  sigma:= 0.291776
  pW:= 0.765095
  aW1:= 0.00789
  bW1:= 1.278046
  aW2:= 0.030121
  bW2:= 3.209155
  Wshift:= 0.00335
  MAr1:= -0.417
  MAr2:= -0.521
  MAr3:= -0.14
  MAr4:= 0.086
  MAvar:= 14.237
  v_rip_dt:= 1.25E-4
  I_threshold:= 0.1
OUTPUT
  RARC:=Rarc
  Vest:=Varc_est
ENDUSE
RECORD
  RARC AS RARC
  VEST AS VEST
ENDMODELS

C Beginning of ATP circuit definition

/BRANCH
C < n1 >< n2 ><ref1><ref2>< R >< L >< C >
C < n1 >< n2 ><ref1><ref2>< R >< A >< B ><Leng><><>0
91VARC VRARC TACS RARC 2
  VARC VRARC NAME PHASOR 10.
  XX0001XX0002 .000337.2E-6 0
  VRARC 1.E-8 0
C Additional resistor defined above between the arc resistance and the ground
    ↪ influences the final results. Its value should be considered during the
    ↪ design of a final model with respect to the real contact resistance that
    ↪ may exist in the modeled object
/SWITCH
C < n 1>< n 2>< Tclose ><Top/Tde >< Ie ><Vf/CLOP >< type >
  XX0002XX0003 MEASURING
  XX0003VARC MEASURING 1
/SOURCE
C < n 1><>< Ampl. >< Freq. ><Phase/T0>< A1 >< T1 >< TSTART >< TSTOP >
14XX0001 1015.4 50. -1. 100.
/OUTPUT
  VARC
BLANK MODELS
BLANK BRANCH
BLANK SWITCH
BLANK SOURCE
BLANK OUTPUT
BLANK PLOT
BEGIN NEW DATA CASE
BLANK
```

Bibliography

[1] S. Lupi, "Arc furnaces," in *Fundamentals of Electroheat: Electrical Technologies for Process Heating*, pp. 83–205, Cham: Springer International Publishing, 2017.

[2] V. Manojlović, Željko Kamberović, M. Korać, and M. Dotlić, "Machine learning analysis of electric arc furnace process for the evaluation of energy efficiency parameters," *Applied Energy*, vol. 307, p. 118209, 2022.

[3] T. A. C. Maia and V. C. Onofri, "Survey on the electric arc furnace and ladle furnace electric system," *Ironmaking & Steelmaking*, vol. 49, no. 10, pp. 976–994, 2022.

[4] A. Bracale, P. Caramia, P. D. Falco, G. Carpinelli, and A. Russo, "DC electric arc furnace modelling for power quality indices assessment," in *2020 19th International Conference on Harmonics and Quality of Power (ICHQP)*, pp. 1–6, 2020.

[5] M. Čerňan, Z. Müller, J. Tlustý, and V. Valouch, "An improved SVC control for electric arc furnace voltage flicker mitigation," *International Journal of Electrical Power & Energy Systems*, vol. 129, p. 106831, 2021.

[6] B. S. Jebaraj, J. Bennet, R. Kannadasan, M. H. Alsharif, M.-K. Kim, A. A. Aly, and M. H. Ahmed, "Power quality enhancement in electric arc furnace using matrix converter and Static VAR Compensator," *Electronics*, vol. 10, no. 9, 2021.

[7] A. Dheepanchakkravarthy, M. P. Selvan, and S. Moorthi, "Alleviation of power quality issues caused by electric arc furnace load in power distribution system using 3-phase four-leg DSTATCOM," *Journal of The Institution of Engineers (India): Series B*, vol. 100, pp. 9–22, Feb 2019.

[8] K. U. Vinayaka and P. S. Puttaswamy, "Improvement of power quality in an electric arc furnace using shunt active filter," in *Emerging Research in Electronics, Computer Science and Technology* (V. Sridhar, M. Padma, and K. R. Rao, eds.), (Singapore), pp. 1255–1269, Springer Singapore, 2019.

[9] D. C. Bhonsle and R. B. Kelkar, "Design and analysis of composite filter for power quality improvement of electric arc furnace," in *2013 3rd International Conference on Electric Power and Energy Conversion Systems*, pp. 1–10, 2013.

[10] J. Mayordomo, L. Beites, R. Asensi, M. Izzeddine, L. Zabala, and J. Amantegui, "A new frequency domain arc furnace model for iterative harmonic analysis," *IEEE Transactions on Power Delivery*, vol. 12, no. 4, pp. 1771–1778, 1997.

[11] D. C. Bhonsle and R. B. Kelkar, "Simulation of electric arc furnace characteristics for voltage flicker study using MATLAB," in *2011 INTERNATIONAL CONFERENCE ON RECENT ADVANCEMENTS IN ELECTRICAL, ELECTRONICS AND CONTROL ENGINEERING*, pp. 174–181, 2011.

[12] M. Panoiu, C. Panoiu, and L. Ghiormez, "Modeling of the electric arc behavior of the electric arc furnace," in *Soft Computing Applications* (V. E. Balas, J. Fodor, A. R. Várkonyi-Kóczy, J. Dombi, and L. C. Jain, eds.), (Berlin, Heidelberg), pp. 261–271, Springer Berlin Heidelberg, 2013.

[13] Y.-J. Liu, G. W. Chang, and R.-C. Hong, "Curve-fitting-based method for modeling voltage–current characteristic of an ac electric arc furnace," *Electric Power Systems Research*, vol. 80, no. 5, pp. 572–581, 2010.

[14] S. Golestani and H. Samet, "Generalised Cassie–Mayr electric arc furnace models," *IET Generation, Transmission & Distribution*, vol. 10, no. 13, pp. 3364–3373, 2016.

[15] A. J. Ustariz-Farfan, L. F. Diaz-Cadavid, and E. A. Cano-Plata, "Modeling and simulation of the electric arc furnace: The issues," in *2021 IEEE Industry Applications Society Annual Meeting (IAS)*, pp. 1–8, 2021.

[16] R. Xu, S. Ma, and M. Zhang, "Modeling of electric arc furnace for power quality analysis," in *2022 IEEE 3rd China International Youth Conference on Electrical Engineering (CIYCEE)*, pp. 1–5, 2022.

[17] D. Solati Alkaran, M. Vatani, M. Sanjari, and G. Gharehpetian, "Parameters estimation of electric arc furnace based on an analytical solution of power balance equation," *International Transactions on Electrical Energy Systems*, vol. 27, no. 4, p. e2295, 2017. e2295 ETEP-16-0221.R1.

[18] J. Marulanda-Durango, A. Escobar-Mejía, A. Alzate-Gómez, and M. Álvarez-López, "A support vector machine-based method for parameter estimation of an electric arc furnace model," *Electric Power Systems Research*, vol. 196, p. 107228, 2021.

[19] H. Samet, E. Farjah, and Z. Sharifi, "A dynamic, nonlinear and time-varying model for electric arc furnace," *International Transactions on Electrical Energy Systems*, vol. 25, no. 10, pp. 2165–2180, 2015.

[20] J. Marulanda-Durango and C. Zuluaga-Ríos, "A meta-heuristic optimization-based method for parameter estimation of an electric arc furnace model," *Results in Engineering*, vol. 17, p. 100850, 2023.

[21] A. Sawicki, "Mathematical model of an electric arc in differential and integral forms with the plasma column radius as a state variable," *Acta Energetica*, no. 2, pp. 57–64, 2020.

[22] M. Torabian Esfahani and B. Vahidi, "A new stochastic model of electric arc furnace based on hidden markov model: A study of its effects on the power system," *IEEE Transactions on Power Delivery*, vol. 27, no. 4, pp. 1893–1901, 2012.

[23] D. Grabowski, *Selected applications of stochastic approach in circuit theory*. Publishing House of the Silesian University of Technology, 2015.

[24] A. Á. Gomez, J. J. M. Durango, and A. E. Mejia, "Electric arc furnace modeling for power quality analysis," in *2010 IEEE ANDESCON*, pp. 1–6, 2010.

[25] F. Illahi, I. El-Amin, and M. U. Mukhtiar, "The application of multiobjective optimization technique to the estimation of electric arc furnace parameters," *IEEE Transactions on Power Delivery*, vol. 33, no. 4, pp. 1727–1734, 2018.

[26] R. Collantes-Bellido and T. Gomez, "Identification and modelling of a three phase arc furnace for voltage disturbance simulation," *IEEE Transactions on Power Delivery*, vol. 12, no. 4, pp. 1812–1817, 1997.

[27] H. Samet, A. Mojallal, T. Ghanbari, and M. R. Farhadi, "Enhancement of SVC performance in electric arc furnace for flicker suppression using a gray-ann based prediction method," *International Transactions on Electrical Energy Systems*, vol. 29, no. 4, p. e2811, 2019. e2811 ITEES-18-0219.R2.

[28] O. Ozgun and A. Abur, "Development of an arc furnace model for power quality studies," in *1999 IEEE Power Engineering Society Summer Meeting. Conference Proceedings (Cat. No.99CH36364)*, vol. 1, pp. 507–511 vol.1, 1999.

[29] G. Carpinelli, F. Iacovone, A. Russo, and P. Varilone, "Chaos-based modeling of dc arc furnaces for power quality issues," *IEEE Transactions on Power Delivery*, vol. 19, no. 4, pp. 1869–1876, 2004.

[30] G. Jang, W. Wang, G. T. Heydt, S. S. Venkata, and B. Lee, "Development of enhanced electric arc furnace models for transient analysis," *Electric Power Components and Systems*, vol. 29, no. 11, pp. 1060–1073, 2001.

[31] R. Garcia-Segura, J. Vázquez Castillo, F. Martell-Chavez, O. Longoria-Gandara, and J. Ortegón Aguilar, "Electric arc furnace modeling with artificial neural networks and arc length with variable voltage gradient," *Energies*, vol. 10, no. 9, 2017.

[32] G. W. Chang, C.-I. Chen, and Y.-J. Liu, "A neural-network-based method of modeling electric arc furnace load for power engineering study," *IEEE Transactions on Power Systems*, vol. 25, no. 1, pp. 138–146, 2010.

[33] G. W. Chang, M.-F. Shih, Y.-Y. Chen, and Y.-J. Liang, "A hybrid wavelet transform and neural-network-based approach for modelling dynamic voltage-current characteristics of electric arc furnace," *IEEE Transactions on Power Delivery*, vol. 29, no. 2, pp. 815–824, 2014.

[34] E. Balouji, Ö. Salor, and T. McKelvey, "Deep learning based predictive compensation of flicker, voltage dips, harmonics and interharmonics in electric arc furnaces," *IEEE Transactions on Industry Applications*, vol. 58, no. 3, pp. 4214–4224, 2022.

[35] V. Feliu-Batlle and R. Rivas-Perez, "Robust fractional-order controller for an EAF electrode position system," *Control Engineering Practice*, vol. 56, pp. 159–173, 2016.

[36] S. M. Mousavi Agah, S. H. Hosseinian, H. A. Abyaneh, and N. Moaddabi, "Parameter identification of arc furnace based on stochastic nature of arc length using two-step optimization technique," *IEEE Transactions on Power Delivery*, vol. 25, no. 4, pp. 2859–2867, 2010.

[37] E. A. Cano-Plata, A. J. Ustariz-Farfan, and O. J. Soto-Marin, "Electric arc furnace model in distribution systems," *IEEE Transactions on Industry Applications*, vol. 51, no. 5, pp. 4313–4320, 2015.

[38] M. Dietz, D. Grabowski, M. Klimas, and H.-J. Starkloff, "Estimation and analysis of the electric arc furnace model coefficients," *IEEE Transactions on Power Delivery*, vol. 37, no. 6, pp. 4956–4967, 2022.

[39] M. Klimas and D. Grabowski, "Application of shallow neural networks in electric arc furnace modeling," *IEEE Transactions on Industry Applications*, vol. 58, no. 5, pp. 6814–6823, 2022.

[40] M. Klimas and D. Grabowski, "Application of the deterministic chaos in ac electric arc furnace modeling," in *2022 IEEE International Conference on Environment and Electrical Engineering and 2022 IEEE Industrial and Commercial Power Systems Europe (EEEIC / I&CPS Europe)*, pp. 1–6, 2022.

[41] M. Klimas and D. Grabowski, "Application of shallow neural networks in electric arc furnace modelling," in *2021 IEEE International Conference on Environment and Electrical Engineering and 2021 IEEE Industrial and Commercial Power Systems Europe (EEEIC / I&CPS Europe)*, pp. 1–6, 2021.

[42] M. Klimas and D. Grabowski, "Application of long short-term memory neural networks for electric arc furnace modelling," in *Intelligent Data Engineering and Automated Learning – IDEAL 2021* (H. Yin, D. Camacho, P. Tino, R. Allmendinger, A. J. Tallón-Ballesteros, K. Tang, S.-B. Cho, P. Novais, and S. Nascimento, eds.), (Cham), pp. 166–175, Springer International Publishing, 2021.

[43] M. Klimas and D. Grabowski, "Identification of nonstationary parameters of electric arc furnace model using monte carlo approach," in *2020 Progress in Applied Electrical Engineering (PAEE)*, pp. 1–6, 2020.

[44] D. Grabowski, J. Walczak, and M. Klimas, "Electric arc furnace power quality analysis based on a stochastic arc model," in *2018 IEEE International Conference on Environment and Electrical Engineering and 2018 IEEE Industrial and Commercial Power Systems Europe (EEEIC / I&CPS Europe)*, pp. 1–6, 2018.

[45] M. Klimas and D. Grabowski, "Implementation of a stochastic electric arc furnace model in emtp-atp.," in *Proceedings of the EEUG Meeting 2022, European EMTP-ATP Users Group e.V.* (E. E.-A. Conference, ed.), pp. 1–12, 2022.

[46] M. Klimas and D. Grabowski, "New directions in electric arc furnace modeling," in *Konferencja z podstaw elektrotechniki i teorii obwodów. XLIII SPETO, Gliwice - Ustroń 25-27. 05. 2022.*, p. 12, 2022.

[47] E. Acha, A. Semlyen, and N. Rajakovic, "A harmonic domain computational package for nonlinear problems and its application to electric arcs," *IEEE Transactions on Power Delivery*, vol. 5, no. 3, pp. 1390–1397, 1990.

[48] G. Chang, C. Hatziadoniu, W. Xu, P. Ribeiro, R. Burch, W. Grady, M. Halpin, Y. Liu, S. Ranade, D. Ruthman, N. Watson, T. Ortmeyer, J. Wikston, A. Medina, A. Testa, R. Gardinier, V. Dinavahi, F. Acram, and P. Lehn, "Modeling devices with nonlinear voltage-current characteristics for harmonic studies," *IEEE Transactions on Power Delivery*, vol. 19, no. 4, pp. 1802–1811, 2004.

[49] B. Stoughton, *The metallurgy of iron and steel.* McGraw-Hill, 1923.

[50] D. C. Prince, "Mercury arc rectifier phenomena," *Journal of the A.I.E.E.*, vol. 46, no. 7, pp. 667–674, 1927.

[51] R. H. Shumway, D. S. Stoffer, and D. S. Stoffer, *Time series analysis and its applications*, vol. 3. Springer, 2000.

[52] L. Devroye, "Nonuniform random variate generation," *Handbooks in operations research and management science*, vol. 13, pp. 83–121, 2006.

[53] J. I. Vélez, J. C. Correa, and F. Marmolejo-Ramos, "A new approach to the Box–Cox transformation," *Frontiers in Applied Mathematics and Statistics*, vol. 1, 2015.

[54] P. E. King, T. L. Ochs, and A. D. Hartman, "Chaotic responses in electric arc furnaces," *Journal of Applied Physics*, vol. 76, no. 4, pp. 2059–2065, 1994.

[55] E. N. Lorenz, "Deterministic nonperiodic flow," *Journal of Atmospheric Sciences*, vol. 20, no. 2, pp. 130 – 141, 1963.

[56] G. Qi, G. Chen, M. A. van Wyk, B. J. van Wyk, and Y. Zhang, "A four-wing chaotic attractor generated from a new 3-d quadratic autonomous system," *Chaos, Solitons & Fractals*, vol. 38, no. 3, pp. 705–721, 2008.

[57] A. Barbiero and A. Hitaj, "Discrete approximations of continuous probability distributions obtained by minimizing cramér-von mises-type distances," *Statistical Papers*, Sep 2022.

[58] S. Petchrompo, D. W. Coit, A. Brintrup, A. Wannakrairot, and A. K. Parlikad, "A review of Pareto pruning methods for multi-objective optimization," *Computers & Industrial Engineering*, vol. 167, p. 108022, 2022.

[59] T. Matsumoto, "A chaotic attractor from chua's circuit," *IEEE Transactions on Circuits and Systems*, vol. 31, no. 12, pp. 1055–1058, 1984.

[60] O. Rössler, "An equation for continuous chaos," *Physics Letters A*, vol. 57, no. 5, pp. 397–398, 1976.

[61] R. K. Pearson, Y. Neuvo, J. Astola, and M. Gabbouj, "Generalized Hampel filters," *EURASIP Journal on Advances in Signal Processing*, vol. 2016, p. 87, Aug 2016.

[62] C. C. Aggarwal *et al.*, "Neural networks and deep learning," *Springer*, vol. 10, no. 978, p. 3, 2018.

[63] MATLAB, *version 9.7.0 (R2019b)*. Natick, Massachusetts: The MathWorks Inc., 2019.

[64] D. Grabowski and J. Walczak, "Deterministic model of electric arc furnace – a closed form solution," *COMPEL - The international journal for computation and mathematics in electrical and electronic engineering*, vol. 32, pp. 1428–1436, Jan 2013.

[65] H.-J. Starkloff, M. Dietz, and G. Chekhanova, "On a stochastic arc furnace model.," *Studia Universitatis Babes-Bolyai, Mathematica*, vol. 64, no. 2, 2019.

[66] S. Das, *Introduction to Fractional Calculus*, pp. 1–50. Berlin, Heidelberg: Springer Berlin Heidelberg, 2011.

[67] J. Gulgowski, T. P. Stefański, and D. Trofimowicz, "On applications of elements modelled by fractional derivatives in circuit theory," *Energies*, vol. 13, no. 21, 2020.

[68] I. Petrás, "Fractional derivatives, fractional integrals, and fractional differential equations in matlab," in *Engineering Education and Research Using MATLAB* (A. H. Assi, ed.), ch. 10, Rijeka: IntechOpen, 2011.

[69] M. Sowa, "Application of subival in solving initial value problems with fractional derivatives," *Applied Mathematics and Computation*, vol. 319, pp. 86–103, 2018. Recent Advances in Computing.

[70] H. Cramér, "On the composition of elementary errors," *Scandinavian Actuarial Journal*, vol. 1928, no. 1, pp. 13–74, 1928.

[71] L. Prikler and H. K. Høidalen, "Atpdraw version 3.5 for windows 9x," tech. rep., NT/2000/XP Users' Manual, 2002.

[72] L. Dube and I. Bonfanti, "Models: A new simulation tool in the emtp," *European Transactions on Electrical Power*, vol. 2, no. 1, pp. 45–50, 1992.

Acronyms

ACF autocorrelation function

ANN artificial neural network

ARIMA autoregressive integrated moving average

CDF cumulative distribution function

EAF electric arc furnace

EMTP-ATP Electromagnetic Transients Program - Alternative Transients Program

GA genetic algorithm

HW Hammerstein-Wiener

LSTM long short-term memory

MLP multilayer perceptron

NARX nonlinear autoregressive exogenous

PACF partial autocorrelation function

RDE random differential equation

RMSE root mean square error

SISO single input single output

V-I voltage-current

List of Figures

1.1 Diagram presenting the most common strategies of EAF modeling. . 16
1.2 Exemplary V-I characteristics of the arc calculated for sinusoidal current and two different sets of k_j coefficients [28], [23]. 18

2.1 Schematic of the EAF construction [49]. 20
2.2 Electrical circuit of EAF. 21
2.3 Phase voltage and current waveforms measured in the large industrial EAF. 23
2.4 Active, reactive and apparent power of each phase of the melting process of the large industrial EAF. 24
2.5 Measured voltage waveform compared with cables and electrodes voltage drop and arc voltage itself for the large industrial EAF. 24
2.6 Photos of the small industrial electric arc furnace. 25
2.7 Measurement phase voltage and current waveforms in the small industrial EAF. 25
2.8 Active, reactive and apparent power during the melting process of the small industrial EAF. 26
2.9 Measured voltage waveform compared with cables and electrodes voltage drop and arc voltage itself for the small industrial EAF. 26
2.10 Photos of the laboratory scale electric arc furnace. 27
2.11 Measurement phase voltage and current waveforms in the laboratory EAF. 27
2.12 Active, reactive and apparent power of each phase of the melting process of the laboratory EAF. 28
2.13 Measured voltage waveform compared with cables and electrodes voltage drop and arc voltage itself for the laboratory EAF. 28

3.1 Diagram of possible RDE model structures. 30
3.2 Graphical presentation of investigated K_j coefficients frames and starting points. 31
3.3 Flowchart of the GA optimization process. 33
3.4 Realizations of K_j stochastic processes estimated from large industrial EAF measurement data. 35
3.5 Autocorrelation and partial autocorrelation function of realizations of K_j stochastic processes obtained from large industrial EAF measurement data. 35
3.6 Three dimensional histogram of raw values and their increments of realizations of K_j stochastic processes obtained from large industrial EAF measurement data. 36

3.7 Short-term current and voltage waveforms and characteristic of the EAF single phase arc measured during the melting stage compared to the simulation output for the large industrial EAF. 36
3.8 High frequency component of large industrial EAF voltage waveform. 37
3.9 Autocorrelation and partial autocorrelation function of the high frequency voltage component for the large industrial EAF. 37
3.10 Short-term current and voltage waveforms and characteristic of EAF single phase arc measured during the melting stage compared to the overall simulation output (with both low and high frequency components) for the large industrial EAF. 38
3.11 Realizations of K_j stochastic processes estimated from the small industrial EAF measurement data. 38
3.12 Autocorrelation and partial autocorrelation function of realizations of K_j stochastic processes obtained from the small industrial EAF measurement data. 38
3.13 Three dimensional histogram of raw values and their increments of realizations of K_j stochastic processes obtained from the small industrial EAF measurement data. 39
3.14 Short-term current and voltage waveforms and characteristic of EAF single phase arc measured during the melting stage compared to the simulation output for the small industrial EAF. 40
3.15 High frequency component of small industrial EAF voltage waveform. 40
3.16 Autocorrelation and partial autocorrelation function of the high frequency voltage component for small industrial EAF. 40
3.17 Short-term current and voltage waveforms and characteristic of EAF single phase arc measured during the melting stage compared to the overall simulation output (with both low and high frequency components) for the small industrial EAF. 41
3.18 Realizations of K_j stochastic processes estimated from laboratory EAF measurement data. 42
3.19 Autocorrelation and partial autocorrelation function of realizations of K_j stochastic processes obtained from laboratory EAF measurement data. 42
3.20 Three dimensional histogram of raw values and their increments of realizations of K_j stochastic processes obtained from laboratory EAF measurement data. 42
3.21 Short-term current and voltage waveforms and characteristic of EAF single phase arc measured during the melting stage compared to the simulation output for the laboratory EAF. 43
3.22 High frequency component of the laboratory EAF voltage waveform. . 43
3.23 Autocorrelation and partial autocorrelation function of the high frequency voltage component for the laboratory EAF. 44
3.24 Short-term current and voltage waveforms and characteristic of the EAF single phase arc measured during the melting stage compared to the overall simulation output (with both low and high frequency component) for the laboratory EAF. 44
3.25 Realizations of $\hat{K}_1$ and $\hat{K}_2$ stochastic processes estimated from large industrial EAF measurement data. 45

3.26 Distribution of the values of $\hat{K}_1(l)$ for the large industrial EAF. . . . 46
3.27 Autocorrelation and partial autocorrelation function of $\hat{K}_1(l)$ and $\Delta\hat{K}_1(l)$ for the large industrial EAF. 46
3.28 Autocorrelation and partial autocorrelation function of $\hat{K}_2(l)$ for the large industrial EAF. 47
3.29 Histogram of $\hat{K}_2(l)$ for the large industrial EAF. 47
3.30 Short-term current and voltage waveforms and characteristic of the EAF single-phase arc measured during the melting stage compared to the extended model output for large industrial EAF. 49

4.1 Example of a Chua circuit chaotic attractor for the following parameters: $C_1 = 15.6$, $C_2 = 27$ $C_{d1} = -\frac{8}{7}$, $C_{d2} = -\frac{5}{7}$. 53
4.2 Example of a Lorenz chaotic attractor for the following parameters: $L_1 = 10$, $L_2 = 28$, $L_3 = \frac{8}{3}$. 53
4.3 Example of a Rössler chaotic attractor for the following parameters: $R_1 = R_2 = 0.2$ and $R_3 = 5.7$. 54
4.4 Example of a four-wing chaotic attractor for the following parameters: $F_1 = 14$, $F_2 = 43$, $F_3 = -1$, $F_4 = 16$, $F_5 = 4$. 55
4.5 Time sequences of the realizations of K_j obtained with an optimized chaotic systems for the large industrial EAF. 56
4.6 Histograms and autocorrelation functions of the realizations of K_j calculated based on measurement data (MD) and fitted using the Lorenz system (LS) or the four-wing attractor system (FWS) for the large industrial EAF. 57
4.7 Comparison of the measurement voltage waveform and the V-I characteristic with a realization generated by a chaotic EAF model for the large industrial EAF. 57
4.8 Time sequences of the realizations of K_j obtained with the optimized chaotic systems for the small industrial EAF. 59
4.9 Histograms and autocorrelation functions of realizations K_j calculated on the basis of measurement data (MD) and fitted using the Rössler system (RS) or the four-wing attractor system (FWS) for the small industrial EAF. 59
4.10 Comparison of the measurement voltage waveform and V-I characteristic with a realization generated by a chaotic EAF model for the small industrial EAF. 59
4.11 Time sequences of the realizations of K_j obtained with the optimized chaotic systems for the laboratory EAF. 60
4.12 Histograms and autocorrelation functions of the realizations of K_j calculated on the basis of the measurement data (MD) and fitted using the four-wing attractor system (FWS) for the laboratory EAF. 61
4.13 Comparison of the measurement voltage waveform and V-I characteristic with a realization generated by a chaotic EAF model for the laboratory EAF. 61

5.1 Diagram presenting ANN based solutions for EAF modeling proposed in the dissertation. 63
5.2 Structure of a single neuron in an ANN model. 63
5.3 Structure of the MLP model. 64

5.4 An example of training data division for the Dual-MLP model. 64
5.5 Structure of the Hammerstein-Wiener model of the EAF [23]. 65
5.6 Structure of NARX ANN. 66
5.7 Structure of M-NARX ANN. 66
5.8 Example of an outlier in EAF's arc conductance waveform. 67
5.9 Structure of a single LSTM cell [63]. 67
5.10 Block diagram of a complete LSTM network. 68
5.11 V-I characteristic of the EAF – comparison between the MLP output and measurement data from the large industrial EAF. 69
5.12 V-I characteristic of the EAF – comparison between the dual MLP output and measurement data from the large industrial EAF. 70
5.13 Comparison between conductance waveforms based on data measured and simulated by the M-NARX for the large industrial EAF. 70
5.14 V-I characteristic of the large industrial EAF – comparison between the M-NARX output and measurement data. 71
5.15 Voltage waveforms – comparison between the outputs of the proposed shallow ANN models obtained for the same input current, for the large industrial EAF. 71
5.16 Exemplary realization of K_j coefficients time series obtained from the LSTM model for the large industrial EAF. 72
5.17 Exemplary V-I characteristic of the large industrial EAF obtained from the LSTM model and measurements. 73
5.18 Exemplary realization of high frequency voltage ripples generated by the LSTM network for the large industrial EAF. 73
5.19 Comparison of the V-I characteristic of the large industrial EAF obtained from the second LSTM model and measurements. 74
5.20 Comparison of the V-I characteristic obtained from the shallow ANNs for small industrial EAF dataset. 74
5.21 Comparison of the voltage waveforms obtained from the shallow ANNs for small industrial EAF dataset. 75
5.22 Exemplary realization of K_j coefficients time series obtained from the LSTM model for the small industrial EAF. 76
5.23 Comparison of the V-I characteristic of small industrial EAF obtained from the LSTM model and measurements. 76
5.24 Exemplary realization of high frequency voltage ripples generated by the LSTM network for the small industrial EAF. 76
5.25 Comparison of the V-I characteristic of the small industrial EAF obtained from the second LSTM model and measurements. 77
5.26 Comparison of the V-I characteristic obtained from the shallow ANNs for laboratory EAF dataset. 78
5.27 Comparison of the voltage waveforms obtained from the shallow ANNs for laboratory EAF dataset. 78
5.28 Exemplary realization of K_j coefficients time series obtained from the LSTM model and measurements for the laboratory EAF. 79
5.29 Comparison of the V-I characteristic of the laboratory EAF obtained from the LSTM model and measurements. 79
5.30 Exemplary realization of high frequency voltage ripples generated by the LSTM network for the laboratory EAF. 79

5.31 Comparison of the V-I characteristic obtained from the second LSTM model and measurements for the laboratory EAF. 80

6.1 Hammerstein-Wiener model of the EAF. 82
6.2 Discrete HW model of an EAF [23]. 83
6.3 Comparison of the shape of the output voltage depending on the value of α with the optimal coefficients k_j (j = 1, 2, 3). 84
6.4 The discrete Hammerstein-Wiener fractional order model of EAF. . . 86
6.5 Histograms of K_j $(j = 1, 2, 3)$ for the classical case with $\alpha = 1$ and for the variable α for the large industrial EAF. 86
6.6 Realization of discrete-time stochastic process of α value for the large industrial EAF. 87
6.7 Histogram of the estimated coefficient α for the large industrial EAF. 87
6.8 Exemplary voltage waveform of the large industrial EAF fractional model fitted to the measurement data and its error. 87
6.9 Box plots of errors for all frames for both constant and variable α for the large industrial EAF 88
6.10 Relationship of the error median depending on the value of the constant order α of the applied fractional differential equation for the large industrial EAF. 89
6.11 Histograms of coefficients K_j $(j = 1, 2, 3)$ for the classical case with $\alpha = 1$ and for the variable α for the small industrial EAF. 90
6.12 Realization of discrete-time stochastic process of α value for the small industrial EAF. 90
6.13 Exemplary voltage waveform and box plot of RMSE errors of the small industrial EAF fitted to measurement data. 90
6.14 Relationship of the median error according to the value of the order of the applied constant fractional differential equation α for the small industrial EAF. 91
6.15 Histograms of coefficients K_j $(j = 1, 2, 3)$ for the classical case with $\alpha = 1$ and for the variable α for the laboratory EAF. 92
6.16 Realization of discrete-time stochastic process of α value for the laboratory EAF. 92
6.17 Exemplary voltage waveform and box plot of RMSE errors of the laboratory EAF fitted to the measurement data. 92
6.18 Relationship of the error median depending on the constant value of the order α of the applied fractional differential equation for the laboratory EAF. 93

7.1 Diagram presenting method of data preprocessing for the statistical comparative analysis. 96
7.2 Comparison between the averaged realizations of the output voltage of the developed models, the output of a model with constant coefficients k_j ([28] and [23]) and the measurement data. 97
7.3 Time series of Cramér-von Mises statistic illustrating divergence between distributions of samples taken from measurement data and a given model. 99
7.4 Bar plot comparing median of W^2 statistics obtained for all considered EAF models. 100

7.5 Comparison between the average computation time and memory used for the development and use of the proposed models. 101

8.1 Graphical explanation of the intermediate calculation of the high frequency voltage component in EMTP-ATP. 106
8.2 Single phase EAF circuit constructed in EMTP-ATP. 108
8.3 Voltage and V-I characteristic of the deterministic part of the model implemented in EMTP-ATP. 108
8.4 Voltage and V-I characteristic of the deterministic and low frequency stochastic component of the model implemented in EMTP-ATP. . . . 108
8.5 Voltage and V-I characteristics of the deterministic stochastic components, both low- and high-frequency, of the model implemented in EMTP-ATP. 108
8.6 Three-phase EAF model constructed in EMTP-ATP. 109
8.7 Output voltage (left graph) and measured current (right graph) of the three-phase EAF model implemented in EMTP-ATP. 109
8.8 V-I characteristics for each of the phases of the three-phase EAF model implemented in EMTP-ATP. 110
8.9 Arc resistance calculated by MODELS block (green line) compared to arc resistance calculated on the basis of the EMTP-ATP results (red line). 110